Verónica María Rodríguez Betancourtt

Raman Spectroscopic Study of
High Temperature Rare Earth
Metal - Rare Earth Halide Solutions:

$Ln\text{-}LnX_3\text{-}$ and $LnX_2\text{-}LnX_3\text{-}(LiX\text{-}KX)_{eu}$
Systems (Ln: Nd, Ce; X: Cl, I)

Raman Spectroscopic Study of High Temperature Rare Earth Metal - Rare Earth Halide Solutions: Ln-LnX$_3$- and LnX$_2$-LnX$_3$-(LiX-KX)$_{eu}$ Systems (Ln: Nd, Ce; X: Cl, I)

Zur Erlangung des akademischen Grades eines
DOKTORS DER NATURWISSENSCHAFTEN
(Dr. rer. nat.)
von der Fakultät für Chemie und Biowissenschaften
der
Universität Karlsruhe (TH)
angenommene

DISSERTATION

von
M. Sc. Verónica María Rodríguez Betancourtt
aus Guadalajara, Jal., Mexiko

Dekan: Prof. Dr. M. Metzler
1. Gutachter: Priv. Doz. Dr. D. Nattland
2. Gutachter: Prof. Dr. M. Kappes
Tag der mündlichen Prüfung: 17.07.03

para Verito, Victor y mis padres

Index

Abstract

In this work new Raman spectroscopic experiments on rare earth metal-rare earth trihalide melts (Ln-LnX$_3$ and LnX$_2$-LnX$_3$: Ln=Ce, Nd; X=Cl, I) and their mixtures in alkali halide eutectic solvents ((LiX-KX)$_{eu}$; X=Cl, I) are presented. The neodymium and cerium systems have been selected because their metal-metal trihalide melts exhibit very different behavior of the specific electric conductivity as function of the metal concentration. On the one hand, in the Ce-systems it increases strongly which may be due to the formation of mobile electronic defect states. On the other hand, in the Nd-systems it shows only a shallow maximum at the composition of NdX$_{2.5}$. For this behavior an intervalence charge transfer mechanisms was suggested. In this context an important objective is to study a possible influence of the specific types of electronic defect states in these systems on the microscopic structure. The main experimental challenge was the strong corrodibility of these melts. To overcome this difficulty a new windowless Raman cell had to be developed. In such a set up the exciting laser beam was focused through a protecting optical window onto the sample contained in a corrosion resistant crucible (e. g. glassy carbon). The Raman spectrum was measured in the back scattering geometry. The optical window had no direct contact with the high temperature melt. The limitations are given by a possible contamination of the window by sublimated traces of the sample.

The main results can be summarized as follows:

- The Raman spectra of following trihalide systems have been measured for the first time: CeCl$_3$, CeI$_3$, NdI$_3$ and their mixtures in the respective alkali halide eutectic solvent. The structure of the LnX$_3$ in the solvent can be characterized by octahedral complexes. The force constants decrease from the chlorides to the iodides.

- The Raman spectra of the following dihalides have been observed in this work: NdCl$_2$, CeI$_2$ and their mixtures in the alkali halide solvent. Interestingly, CeCl$_2$ might form as

intermediate species on doping $CeCl_3$ with Ce. It is not a stable compound in the Ce-$CeCl_3$ phase diagram.

- With respect to the above mentioned main objective the following conclusions can be drawn:

(i) On mixing of $NdCl_2$ with $NdCl_3$ in $(LiCl\text{-}KCl)_{eu}$ the undisturbed spectra of both components can be observed simultaneously. This is in agreement with the suggested intervalence charge transfer hopping mechanism if one assumes a hopping rate below 10^{12}.

(ii) Even though $CeCl_2$ might form as intermediate, in the equilibrium spectra of liquid Ce-$CeCl_3$-$(LiCl\text{-}KCl)_{eu}$ only the typical $CeCl_6^{3-}$-octahedra can be identified. This supports the assumption that in these systems the electronic defect states are probably mobile Drude-like electrons which do not lead to new Raman detectable species. A qualitatively similar observation was made for CeI_2-CeI_3-$(LiI\text{-}KI)_{eu}$ melts.

Zusammenfassung

In der vorliegenden Arbeit werden neue spektroskopische Ramanexperimente an Seltenerdmetall- Seltenerdmetalltrihalogenid Schmelzen (Ln-LnX$_3$ und LnX$_2$-LnX$_3$: Ln=Ce, Nd; X=Cl, I) und deren Mischungen mit flüssigen eutektischen Alkali-Halogeniden [(LiX-KX)$_{eu}$; X=Cl, I)] dargestellt. Die Neodym- und Cer-Systeme wurden ausgewählt weil ihre Metall-Metalltrihalogenid-Schmelzen sehr unterschiedliches Verhalten der spezifischen elektrischen Leitfähigkeit mit der Metallkonzentration zeigen. Einerseits steigt sie in den Cer-Systemen sehr stark an, was mit der Bildung von beweglichen elektronischen Defektzuständen erklärt werden kann. Andererseits, verläuft sie bei den Nd-Systemen nur durch ein flaches Maximum bei einer Zusammensetzung von NdX$_{2.5}$. Für dieses Verhalten wurde ein *Intervalence Charge Transfer* Mechanismus vorgeschlagen. Eine wichtige Zielsetzung ist in diesem Zusammenhang, einen möglichen Einfluss der spezifischen Art des elektronischen Defektzustandes in diesen Systemen auf die mikroskopische Struktur zu untersuchen. Die wesentliche experimentelle Herausforderung war die starke Korrosivität dieser Schmelzen. Um diese Schwierigkeiten zu überwinden, musste eine neue fensterlose Ramanzelle entwickelt werden. In diesem Aufbau wurde der anregende Laserstrahl durch das die Probe schützende optische Fenster auf die Probe fokussiert, die sich in einem korrosionsresistenten Tiegel befand (z. B. aus glasartigen Kohlenstoff). Das Ramanspektrum wurde in Rückstrengeometrie gemessen. Das optische Fenster hatte keinen direkten Kontakt mit der Hochtemperaturschmelze. Diese experimentelle Vorgehensweise hat ihre Grenzen in der möglichen Kontamination des Fensters durch sublimierten Rest der Probe.

Die wesentlichen Ergebnisse können wie folgt zusammengefasst werden:

- Die Raman Spektren der folgenden Trihalogenid Systeme wurden zum ersten Mal gemessen: CeCl$_3$, CeI$_3$, NdI$_3$ und ihre Mischungen im jeweiligen eutektischen Alkalihalogenidlösungsmittel. Die Struktur des LnX$_3$ im Lösungsmittel kann durch

oktaedrische Komplexe gekennzeichnet werden. Die Kraft konstante nimmt von den Chlorverbindungen zu den Jodiden ab.

- Die Raman Spektren der folgenden Dihalogenide wurden in dieser Arbeit beobachtet: $NdCl_2$, CeI_2 und ihre Mischungen im eutektischen Alkalihalogenidlösungsmittel. Interessanterweise bildet sich $CeCl_2$ möglicherweise als intermediäre Spezies, wenn $CeCl_3$ mit Cer-Metall dotiert wird. Im Ce-CeCl$_3$ Phasendiagramm ist es nicht als stabile Verbindung erkannt.

- In Bezug auf die oben erwähnt Hauptzielsetzung können folgende Schlussfolgerungen gezogen werden:

  (i)   Beim Mischen von $NdCl_2$ mit $NdCl_3$ in (LiCl-KCl)$_{eu}$ können die ungestörten Spektren der beiden Bestandteile nebeneinander beobachtet werden. Dies ist in Übereinstimmung mit dem vorgeschlagenen *Intervalence Charge Transfer* Mechanismus, wenn man eine Platzwechselfrequenz des Elektrons von weniger als 10^{12} Hz zugrunde legt.

  (ii)   Obwohl sich $CeCl_2$ als Intermediär bildet, können in den Gleichgewichtsspektren von flüssigem Ce-CeCl$_3$-(LiCl-KCl)$_{eu}$ lediglich die typischen $CeCl_6^{3-}$-Oktaeder identifiziert werden. Dieses stützt die Annahme, dass in diesen Systemen die elektronischen Defektzustände vermutlich bewegliche Drude Elektronen sind, die nicht zu neuen Spezies führen, die im Ramanspektrum nachweisbar sind. Eine qualitativ ähnliche Beobachtung wurde für CeI_2-CeI$_3$-(LiI-KI)$_{eu}$ Schmelzen gemacht.

1. Introduction

The aim of this investigation is the study of the microscopic structure of rare earth halide systems in the molten state applying Raman spectroscopy. More specifically, we are interested in a possible influence on the microscopic structure as molten rare earth trihalide systems are doped with the respective rare earth metal or with its subhalide.

In general, metal molten salt solutions may be subdivided in two main prototypical groups with respect to different mechanisms for electron localization. First, the alkali metal-alkali halide systems show over a miscibility gap a homogeneous phase range where the system undergoes a continuous transition from a liquid ionic conductor (the pure liquid salt) to a metallic system (the pure liquid metal). No stable subhalide can be found. Instead, in the salt rich range the electronic defect states are localized F-center like states and spin paired (bipolaronic) states in equilibrium with mobile nearly-free Drude electrons. The first can be identified by their characteristic absorption band whereas the latter lead to a strong increase of the specific electronic conductivity with increasing metal concentration. The alkali metal-alkali halide systems exhibit a non metal-to-metal transition in the concentration range of the metal of $x_{NMM} \approx 0.2$. The systems have been studied quite extensively and are described in some reviews (Bredig 1964, Warren 1985, Nattland 1996, Freyland 1994, Freyland 1995).

The second group of metal-molten salt systems is represented by mixed valence transition metal-transition metal halide systems like tantalum or niobium halides. Doping of pentavalent metal halide containing melts with the respective transition metal lead to subhalide species like Ta(IV)-chloride. Here, electron transport takes place by hopping from

one Ta-site to another. This intervalence charge transfer leads to a maximum of electronic conductivity at a concentration ratio of Ta(V)/Ta(IV) $\approx$ 1. The value of the electronic conductivity does exceed considerably that of the ions (Stöhr 1999, Stöhr 1999a).

In this respect the rare earth metals and their trihalides are of particular interest. As can be seen for the Ln-LnCl$_3$ system in Fig 1.1 and for Ln-LnI$_3$ system in Fig 1.2 they display both limiting cases described above. As the lighter rare earth metal (La and Ce) are dissolved in their molten trihalides the conductivity rises almost as steep as in the alkali metal-alkali halide systems. Thus, the mobile electronic species must exist in these systems. On the other hand, the neodymium systems show a shallow maximum of the conductivity. In these systems stable subhalides exist. This resembles the intervalence charge transfer transport mechanism. For Nd-NdCl$_3$ (Terakado 2002a) and for Nd-NdI$_3$ (Zein El Abedin 2002) this was suggested recently on account of optical absorption and conductivity measurements.
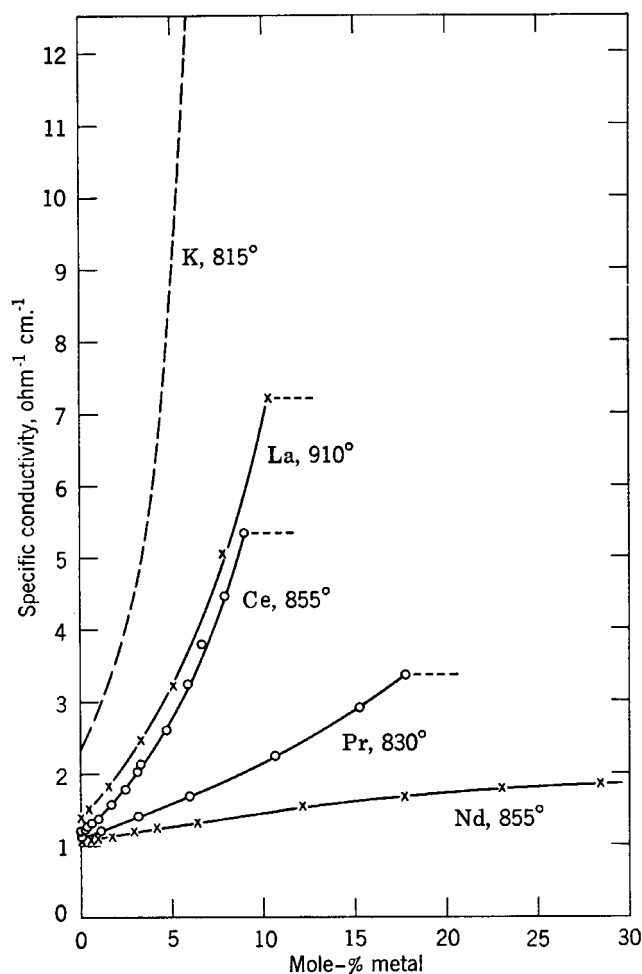
Figure 1.1: Specific conductivity in rare earth metal-rare earth metal chloride systems (Bredig 1964).
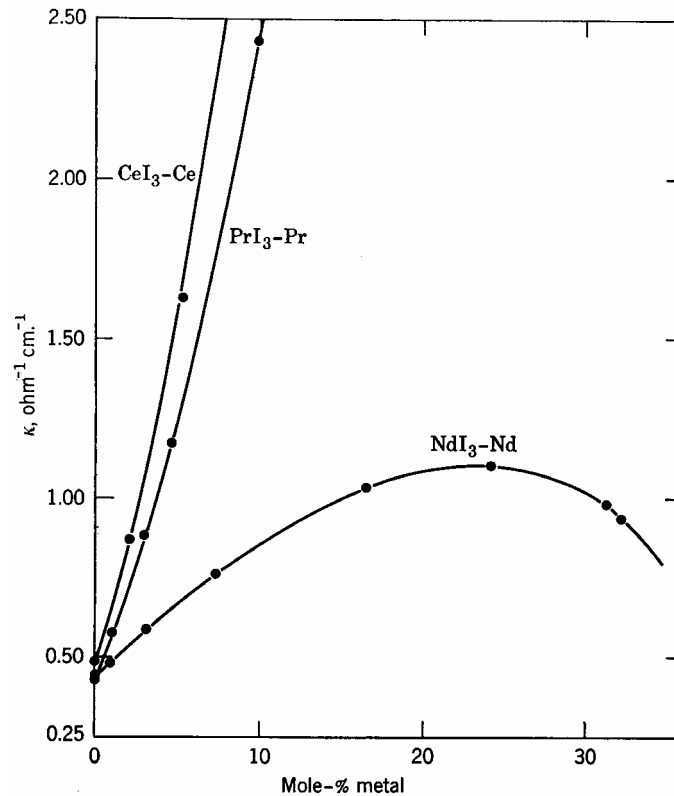
Figure 1.2: Specific conductivity in rare earth metal-rare earth metal iodide systems (Bredig 1964).

Besides the electronic properties, the modifications of the microscopic structure of liquid LnX_3 systems as they are doped with Ln metal are of special interest. In this respect, Raman spectroscopy can provide valuable new information on a possible interplay between electronic and microscopic structure: does the structure of the Raman active species in the melt change on doping? Do new species appear as the liquid trihalide is mixed with the respective metal or with the dihalide?

The microscopic structures of rare earth trihalides and their molten mixtures with alkali halides (AX) have been extensively studied by G. M. Papatheodorou's research group at the University of Patras by means of vibrational Raman spectroscopy (Papatheodorou 1975, Papatheodorou 2002, Photiadis 1994, Photiadis 1998, Børresen 1996, Dracopoulos 1998). They found that in the solid state the microscopic structure of pure $LnCl_3$ change along the lanthanide series, depending on the size of the metal atom. Thus, for large Ln^{3+} cations the trihalides are hexagonal, with a nine-fold coordination of Ln. For small Ln^{3+} cations the structures are monoclinic or rhombohedral, being the Ln six-fold coordinated. For certain

intermediate cations the trihalides are orthorhombic with an eight-fold coordination. In the liquid state on the other hand, the Raman patterns indicate a nearly common structure consisting of a loose network of edge bridged distorted octahedral (Ln with six-fold coordination). Furthermore, in rich alkali halide molten mixtures ($x_{NdCl_3} \leq 0.25$) the normal octahedral species LnX_6^{3-} dominate (Pavlatou 1997, Photiadis 1993, Photiadis1998).

Contrary to the LnX_3, the Ln-LnX$_3$ systems and their mixtures with alkali halide mixtures had not been investigated up to now by Raman spectroscopy. Probably this is mainly due to their chemical corrosive properties and in the case of LnX$_2$ to the problems of disproportionation at high temperatures, i.e. 3LnX$_2 \rightarrow$ 2LnX$_3$ + Ln (Gmelin 1982, Lavtep 1986).

To overcome at least parts of these difficulties a new approach is presented in this work. On the one hand, we use a Raman spectrometer with a CCD camera for fast experiments. A microscope objective with a short working distance allows a highly focused laser beam and small sample sizes. On the other hand we employ windowless cells to avoid cell corrosion by the melt. These cells including furnace have to be specially designed for the optical set up.

2. Basic Concepts of Raman Spectroscopy

2.1. Classical Description of Raman Spectroscopy

In Raman spectroscopy, a monochromatic incident beam ($\tilde{\nu}_0$) is passed through the sample and the scattered light is monitored. This light consists of two contributions: the elastic *Rayleigh scattering*, which is relatively strong and the inelastic *Raman scattering*, which is comparably weak ($<10^{-5}$ of the incident beam) with frequencies of $\tilde{\nu}_0 \pm \tilde{\nu}_m$, where $\tilde{\nu}_m$ is a vibrational frequency of a molecule. The $\tilde{\nu}_0$ - $\tilde{\nu}_m$ lines are called *Stokes lines* and the $\tilde{\nu}_0 +$ $\tilde{\nu}_m$ lines *anti-Stokes lines*. Thus, in Raman spectroscopy, we measure the vibrational frequency ($\tilde{\nu}_m$) as a shift from the incident beam frequency ($\tilde{\nu}_0$)[1] (Bulkin 1991, Ferraro 1994, Long 1977, Herzberg 1954).

The simplest way of thinking about the mechanism of Raman spectroscopy is via an energy level diagram such as that shown in Fig 2.1. In normal Raman spectroscopy the exciting line ($\tilde{\nu}_0$) is chosen so that its energy is far below the first electronic excited state. The dotted line indicates a virtual state to distinguish it from the real excited state.

As determined by the Boltzmann distribution the population of molecules at v = 0 is much larger than at v = 1. Thus, the Stokes lines (S) are stronger than the anti-Stokes lines (A) under normal conditions. Since both give the same information, it is customary to measure

---

[1] Although Raman spectra are normally observed for vibrational and rotational transitions, it is possible to observe Raman spectra of electronic transitions between ground states and low-energy excited states (Ferraro 1994, Long 1977).

only the Stokes side of the spectrum. However, both lines can be beneficially used to calibrate the monochromator employed in the experiment.

Resonance Raman (RR) scattering occurs when the exciting line is chosen so that its energy intercepts the manifold of an electronic excited state. In this case also fluorescence spectra are observed when the excited state molecule decays to the lowest vibrational level via radiationless transitions and then emits radiation. This can strongly distort the Raman spectrum.
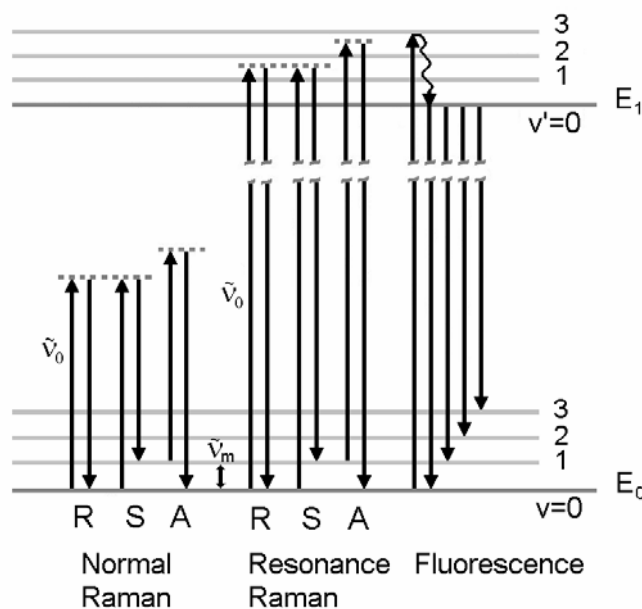
Figure 2.1: Energy level diagram showing the basic transitions involved in Raman scattering: Rayleigh (R), Stokes (S) and anti-Stokes (A) scattering. In conventional Raman spectroscopy, the incident radiation does not match an absorption frequency of the molecule, and there is only a transition to a virtual state. However, in the resonance Raman Effect the incident radiation has a frequency that coincides with a molecular transition. In Fluorescence, an radiationless decay to low lying vibrational states of an electronically excited state is followed by the emission of photons as the molecule decays to the electronic ground state.

2.2. Origin of the Raman Spectrum

As mentioned above Raman spectroscopy has its origin in the general phenomenon of light scattering, in which the electromagnetic radiation interacts with a pulsating, deformable (i.e. polarizable) electron cloud. For an overwiew see e.g. Long 1977, Bulkin 1991 and Ferraro 1994. In the specific case of vibrational Raman scattering, this interaction is

modulated by the molecular vibrations. According to the classical theory, Raman scattering can be explained as follows: the electric field strength (E) of an electromagnetic wave (laser beam with frequency $\tilde{v}_0$) fluctuates harmonically with time (t)

$$E = E_0 \cos 2\pi \tilde{v}_0 t \, , \tag{2.1}$$

where E_0 is the maximum amplitude. If a diatomic molecule is irradiated by this light, it induces an electric dipole moment μ, such that

$$\mu = \alpha E = \alpha E_0 \cos 2\pi \tilde{v}_0 t \, , \tag{2.2}$$

where the proportionality constant α is called the *polarizability tensor*, a 3×3 matrix. If the molecule is vibrating with a frequency $\tilde{v}_m$, the nuclear displacement Q is written

$$Q = Q_0 \cos 2\pi \tilde{v}_m t \, , \tag{2.3}$$

where Q_0 is the vibrational amplitude. For small amplitudes, α is a linear function of Q. Thus we can write

$$\alpha = \alpha_0 + \left(\frac{\partial \alpha}{\partial Q} \right)_0 Q + \textit{higher order terms.} \tag{2.4}$$

Here, α_0 is the polarizability at the equilibrium position, and $(\partial\alpha/\partial Q)_0$ is the rate of change of α with respect to the change in Q, evaluated at the equilibrium position.

Combining (2.2) with (2.4, truncated up to 1st order term), we obtain

$$\mu = \alpha_0 E_0 \cos 2\pi \tilde{v}_0 t + \frac{1}{2}\left(\frac{\partial \alpha}{\partial Q} \right)_0 \left[\cos\{2\pi(\tilde{v}_0 + \tilde{v}_m)t\} + \cos\{2\pi(\tilde{v}_0 - \tilde{v}_m)t\} \right]. \tag{2.5}$$

The three terms on the right hand side of this equation represent the three major phenomena observed in a simple Raman spectroscopy experiment: the first term is elastic scattering (known as Rayleigh scattering), the second term with frequency $\tilde{v}_0 + \tilde{v}_m$ corresponds to the anti-Stokes Raman scattering and the third term is the Stokes Raman scattering. If $(\partial\alpha/\partial Q)_0$ is zero, the vibration is not Raman active. In other words, to be Raman active, the polarizability must be changed with the vibration of the molecule.

The classical description of Raman spectroscopy gives only a very limited insight into the relative intensities of each of these phenomena. One does expect that $(\partial\alpha/\partial Q)_0$ will be much smaller than α_0, so that the Raman scattering should be less intense than the Rayleigh scattering. This is in fact the case. The relative intensities of the Stokes and anti-Stokes scattering are only predicted to differ by the ratio of $[(\tilde{v}_0 - \tilde{v}_m)/(\tilde{v}_0 + \tilde{v}_m)]^4$, which is not

according with observation. As earlier indicated, the population of any excited level is always less than that of the ground state, being the Boltzmann distribution the major factor in determining the relative intensities of these two phenomena. This make Stokes Raman scattering always more intense than anti-Stokes.

A quantum mechanical treatment of Raman scattering made by Placzek (Long 1977, Sushchinskii 1972), gives the expressions of the Raman intensities in different geometries. In these expressions, the polarizability tensor α is divided into two parts

$$\alpha = \alpha_s + \alpha_a , \tag{2.6}$$

where α_s is the symmetric or isotropic part and α_a the asymmetric or anisotropic part. These are defined as

$$3\alpha_s = \left(\alpha_{xx} + \alpha_{yy} + \alpha_{zz} \right)$$

$$2(\alpha_a)^2 = \left[\left(\alpha_{xx} - \alpha_{yy} \right)^2 + \left(\alpha_{yy} - \alpha_{zz} \right)^2 + \left(\alpha_{zz} - \alpha_{xx} \right)^2 + 6\left(\alpha_{xy}^2 + \alpha_{yz}^2 + \alpha_{zx}^2 \right) \right]. \tag{2.7}$$

The result for Raman scattering at right angles in terms of these components of the polarizability is derived for a molecule initially in state m and finally in state n as

$$I = \frac{\left(\tilde{\nu}_0 + \tilde{\nu}_{mn} \right)^4}{\tilde{\nu}_{mn}} \cdot \frac{NI_0}{1 - \exp\left(-h\tilde{\nu}_{mn} \big/ kT \right)} \left[45\left(\alpha_s' \right)^2 + 13\left(\alpha_a' \right)^2 \right], \tag{2.8}$$

where N is the number of molecules in state m, I_0 is the incident intensity and α' is $(\partial\alpha/\partial Q)$. The coefficients 45 and 13 arise from the orientational averaging process and are a consequence of the geometry. This yields the ratio of Stokes to anti-Stokes intensity,

$$\frac{I_{Stokes}}{I_{anti-Stokes}} = \frac{\left(\tilde{\nu}_0 - \tilde{\nu}_m \right)^4}{\left(\tilde{\nu}_0 + \tilde{\nu}_m \right)^4} \exp\left(h\tilde{\nu}_m \big/ kT \right) \tag{2.9}$$

which is verified experimentally at thermal equilibrium. These expressions assume that $\tilde{\nu}_o$ is far from any electronic levels of the molecule.

2.3. Depolarization Ratios of Raman Bands

Depolarization ratios of Raman bands provide valuable information about the symmetry of a vibration, which is indispensable in making band assignments. Fig 2.2 shows a coordinate system which is used for measurements of depolarization ratios. A molecule

situated at the origin is irradiated from the *y*-direction with plane polarized light whose electric vector oscillates on the *yz*-plane (E_z). If one observes scattered radiation in the *x*-direction, and measures the intensities in the *xy*(I_y)- and *xz*(I_z)-planes, the depolarization ratio ρ is defined by

$$\rho = \frac{I_{\parallel}}{I_{\perp}} \quad . \tag{2.10}$$

When the molecule is performing a symmetric vibration, the vibration is called *polarized* (abbreviated as *p*) and $0 \leq \rho < \frac{3}{4}$. If the molecule is performing an asymmetric vibration, $\rho = \frac{3}{4}$ and the vibration is called *depolarized* (abbreviated as *dp*).
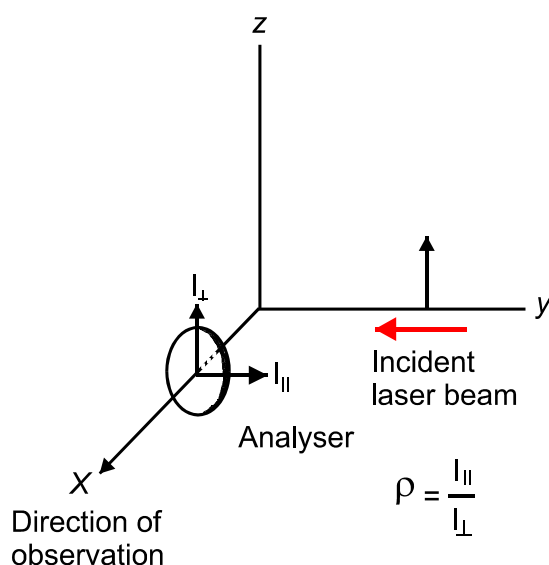
Fig 2.2: Polarization of the light. The sample is irradiated with a laser beam from the *y*-direction with plane polarized light, with the electronic vector in *z*-direction.

2.4. Normal modes of vibration of the molecules

To interpret a Raman spectrum it is necessary to know the internal motions of a vibrating molecule. That is apparently complex but it can be resolved into a number of relatively simple vibratory motions known as *the normal modes of vibration*. Each of these modes has a characteristic frequency, dependent on the mass of the atoms and the forces between them. The number of modes is *3N-6* for a nonlinear molecule and *3N-5* for a linear molecule containing *N* atoms. There are several types of motion that contribute to the normal

modes like stretching motion between two bonded atoms, bending motion between three atoms connected by two bonds, and out-of-plane deformation modes that change an otherwise planar structure into a non-planar.

The activity of the normal modes in Raman spectroscopy is dependent on the geometry of the molecule. The shape of a molecule is specified by the symmetry elements (planes of symmetry, axes of rotation, center of symmetry, see Fig 2.4), which leads to a designation in terms of the molecular point group. A standard method of classifying molecules is the *Group Theory*, in which a set of mathematical methods allow one to correlate the symmetry properties of the normal modes of vibration to the symmetry of the molecule. For an isolated molecule, the analysis reveals the number of normal modes and their symmetry type, the numbers of Raman active modes, the number of polarized Raman lines, and the activity of overtones and combination bands. These Raman selection rules apply rigorously to molecules in isolation, i.e., molecules unperturbed by their environment. In consequence, there will be no strict selection rules operating on the liquid phase. The relaxation of selection rules is associated with the development of intermolecular forces (Halford 1946, Harfold 1946a).
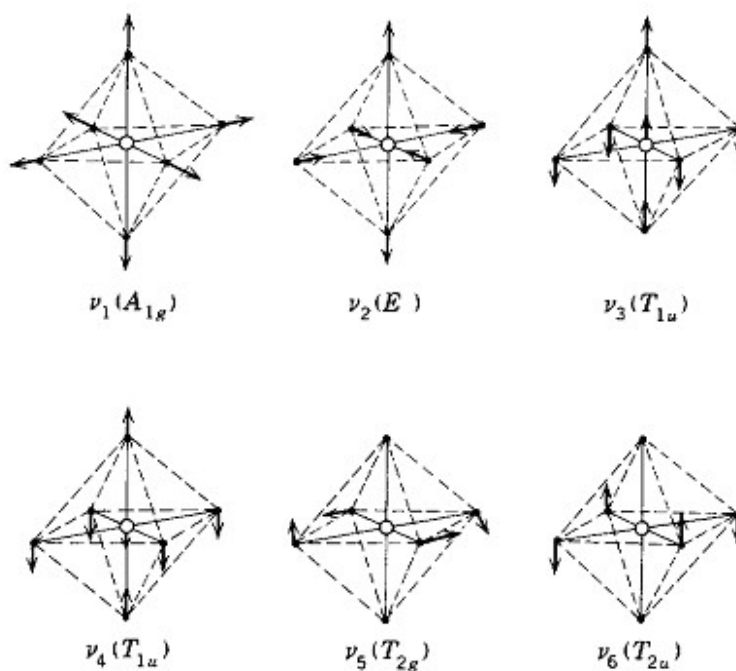
Figure 2.3: Normal modes of vibrations of octahedral AB_6 molecule —point group O_h. The vibrations A_{1g} and E_g are bond stretch, T_{2g} is due to an angle deformation. The $\nu_1(A_{g1})$, $\nu_2(E_g)$ and $\nu_5(T_{g2})$ are Raman active (Ferraro 1969).
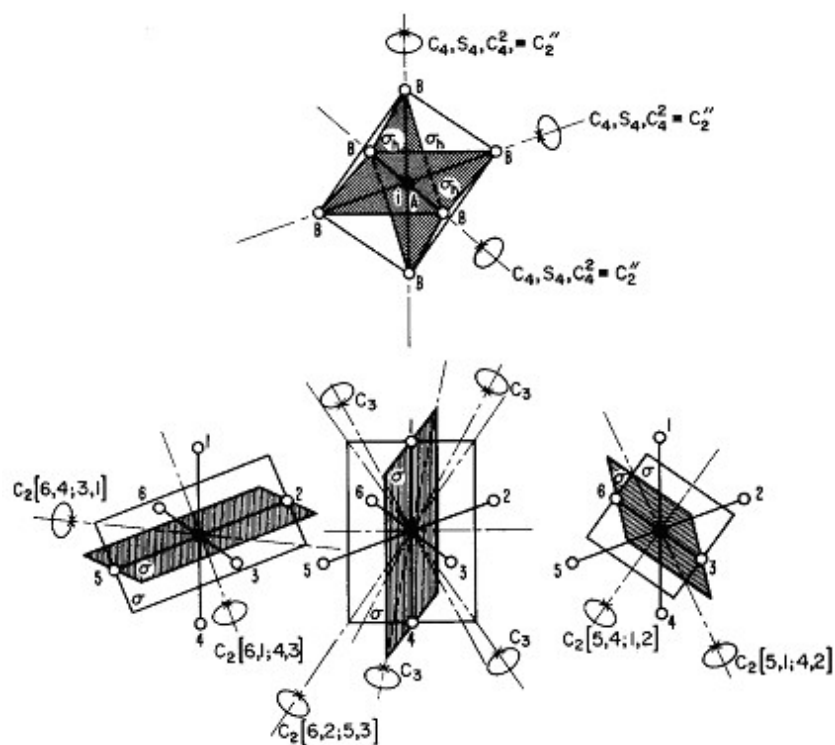
Fig. 2.4: Symmetry elements for the O_h point group ($6C_2$, $4C_3$, $3C_4$, $3S_4$, $9\sigma_v$, i). The numbers in brackets indicate the atoms between which each axis passes. For example, the axis followed by the bracket with the asterisk passes between atoms 5 and 1 and 4 and 2. C_n are the rotation axes, with a rotation angle of 360°/n; σ are the planes of symmetry (v: vertical; h: horizontal); *i* is the center of symmetry and S_n are the rotation reflection axes (Ferraro 1969).

2.5. Symmetry and Selection Rules

The selection rules must be applied to each normal vibration in order to determine whether the vibration is active or not in the Raman spectra. Vibrations that do not distort the molecule (symmetric vibrations) are intense in the Raman spectrum. If the atoms involved in these vibrations are highly polarizable, then the Raman intensity is high.

When a molecule is placed in an electric field E (e.g. by means of a laser beam), it suffers distortion since the positively charged nuclei are attracted toward the negative pole, and electrons toward the positive pole. This charge separation produces an induced dipole moment μ given by equation 2.2.

In real molecules, such a simple relationship does not hold since both μ and E are vectors consisting of three components in the x, y, and z directions. Thus equation 2.2 must be written as

$$
\begin{bmatrix} \mu_x \\ \mu_y \\ \mu_z \end{bmatrix} = \begin{bmatrix} \alpha_{xx} & \alpha_{xy} & \alpha_{xz} \\ \alpha_{yx} & \alpha_{yy} & v_{yz} \\ \alpha_{zx} & \alpha_{zy} & \alpha_{zz} \end{bmatrix} \begin{bmatrix} E_x \\ E_y \\ E_z \end{bmatrix} . \tag{2.11}
$$

The matrix on the right-hand side is called the *polarizability tensor*. In normal Raman scattering, this tensor is symmetric: $\alpha_{xy} = \alpha_{yx}$, $\alpha_{xz} = \alpha_{zx}$ and $\alpha_{yz} = \alpha_{zy}$. According to quantum mechanics, the vibration is Raman active if one of these components of the polarizability tensor is changed during the vibration.

A vibration that is symmetrical with respect to the center of symmetry is Raman active but not IR active, whereas those that are anti-symmetric with respect to the center of symmetry are IR active but not Raman active. This condition is known as the *mutual exclusion principle* and holds for any molecules having a center of symmetry.

Molecules can be classified according to symmetry elements or operations that leave at least one common point unchanged. This classification gives the *point group* representation for the molecule. Very useful information about the *point group* is contained in character tables (see Ferraro 1969 and Walton 1998).

When a molecule is relatively small and/or belongs to a *point group* of relatively high symmetry, it is possible to deduce the molecular structure by using the symmetry selection rules. Molecules of XY_2 (linear $D_{\infty h}$ or bent C_{2v}), XY_3 (planar D_{3h} or pyramidal C_{3v}), XY_4 (square planar D_{4h} or tetrahedral T_d), XY_5 (trigonal-bipyramidal D_{3h} or tetragonal-pyramidal C_{4v}) and XY_6 (octahedral O_h) types may take one of the structures indicated in parentheses. Since the number of Raman-active vibrations is different for each structure, the most probable structure can be chosen by comparing the number of observed Raman bands that were predicted for each structure by symmetry selections rules.

On the other hand, Nishimura et al. (Bulkin 1991) have summarized the common observations about Raman spectral intensities in four main points:

1. Stretching vibrations associated with chemical bonds should be more intense than deformation vibrations.

2. Multiple chemical bonds should give rise to intense stretching modes, e.g., a Raman band due to a C=C vibration should be more intense than that due to a C-C vibration.

3. Bonds involving atoms of large atomic mass are expected to give rise to stretching vibrations of high Raman intensity.

4. Those Raman features arising from normal coordinates involving two *in -phase bond stretching motions* are more intense than those involving a 180° phase difference. Similarly, for cyclic compounds the *in-phase "breathing"* mode is usually the most intense.

2.7. Representation of a Raman Spectrum

Normally a Raman spectrum is represented by plotting the intensity of the scattered radiation $I(\tilde{\nu})$ vs. the Raman shift ($\Delta\tilde{\nu} = \tilde{\nu}_0 \pm \tilde{\nu}_m$, $\Delta\tilde{\nu}$ is often written as $\tilde{\nu}$ for brevity). The measured Raman intensity, $I(\tilde{\nu}_i)$, is given by

$$I(\tilde{\nu}_i) = C(\tilde{\nu}_0 - \tilde{\nu}_i)^4 \tilde{\nu}_i^{-1} B^{-1} S_i \qquad (2.12)$$

where C is a constant that depends on the instrument response, on the slit width, on the solid collection angle, and on the attenuation due to the absorptivity (color) of the sample; $\tilde{\nu}_0$ is the absolute frequency of the laser excitation line; $\tilde{\nu}_i$ is the frequency difference of the scattered radiation (i.e. the Raman shift); B is a temperature factor given by

$$B = 1 - \exp\left(-h\tilde{\nu}_i c \Big/ kT\right) \qquad (2.13)$$

when the Boltzmann distribution is applied; and S_i is the intrinsic molar scattering coefficient at frequency $\tilde{\nu}_i$ (Bulkin 1991).

Most of the published spectra of species in solution are presented in this $I(\tilde{\nu})$ vs. $\tilde{\nu}$ format. Furthermore, important additional information can be obtained by separating and measuring the light with different polarizations ($I_{\parallel}$ and $I_{\perp}$).

As above mentioned, the depolarization ratio is a useful parameter because it allows one to designate whether a Raman band originates from a totally symmetric mode of vibration ($\rho < \frac{3}{4}$) or not ($\rho = \frac{3}{4}$). However, there are many cases where the conclusion is ambiguous: $I_{\parallel}$

contains information about both the isotropic and anisotropic polarizability tensor components; $I_\perp$ contains only contributions from the anisotropic polarizability tensor components. Another way of portraying the spectrum is plotting I_{iso} (intensity of isotropic components) versus $\tilde{\nu}$, where

$$I_{iso} = I_{\parallel} - \frac{4}{3} I_{\perp} \ . \tag{2.14}$$

This spectrum contains only the isotropic polarizability elements and thus only contributions from symmetric vibrational modes. The anisotropic spectrum, I_{aniso}, is given by

$$I_{aniso} = \frac{4}{3} I_{\perp} \tag{2.15}$$

For spectra with $\tilde{\nu} < 300$ cm^{-1} a reduced function R($\tilde{\nu}$) is recommended (Brooker 1988, Papatheodorou 1996):

$$R(\tilde{\nu}) = I(\tilde{\nu})(\tilde{\nu}_0 - \tilde{\nu})^4 \tilde{\nu} B \ . \tag{2.16}$$

The important feature of this reduced function is the fact that the corrected Raman scattered intensity is directly proportional to the intrinsic molar scattering coefficient S_i. This quantity removes the temperature and frequency dependent terms from the directly measured $I(\tilde{\nu})$. It essentially removes the contribution from the Rayleigh scattering and thus may reveal Raman bands at low wave numbers. The isotropic and anisotropic spectra can also be presented in the form

$$R_{iso} = R_{\parallel} - \frac{4}{3} R_{\perp} \ \text{ and } \ R_{aniso} = \frac{4}{3} R_{\perp} \tag{2.17}$$

2.8. Fluorescence

The intensity of a Raman band can be affected by some influences. For spectra at high temperatures, the two major influences are *fluorescence* and *blackbody radiation*.

Fluorescence (Fig 2.1) is a strong influence in the Raman spectrum. As a phenomenon, fluorescence is stronger than Raman scattering. Often, when one tries to excite a Raman spectrum, fluorescence is the only observed phenomenon.

There are several methods of minimizing this problem. If impurities in the sample are causing fluorescence, the sample should be purified or irradiated by high-power laser beams

for a prolonged time so that fluorescence impurities are bleached out. If the sample itself is fluorescent, the first thing to do is to change the exciting wavelength. By shifting it to a longer wavelength, fluorescence may be reduced greatly. Addition of quenching agents such as potassium iodide or mercury halides is also effective in some cases. Repetitive scanning, coupled with background subtraction, is also found to be effective. It is also possible to discriminate fluorescence by using pulsed lasers since the lifetime of Raman scattering (10^{-12}-10^{-13} s) is much shorter than that of fluorescence (10^{-7}-10^{-9} s).

The use of UV or near-IR excitation has proved to be effective in reducing this problem (Ferraro 1994). Since fluorescence is normally red-shifted from the exciting line, it interferes mostly with the Stokes spectrum and comparatively less with the anti-Stokes one. It is possible therefore with some samples to obtain a Raman spectrum by using the anti-Stokes signal when the fluorescence obscures the Stokes spectrum (Bulkin 1991).

2.9. Blackbody Radiation

For measurements at high temperatures the *blackbody radiation* is a serious influence on the Raman intensity. Heating and blackbody radiation may be by itself so efficient that it is impossible to observe Raman spectra. A hot object emits electromagnetic radiation, and an appreciable proportion of this radiation is in the visible region of the spectrum at high temperatures; additionally, a higher proportion of short-wavelength blue light is generated as the temperature is raised. This behavior is seen when a heated iron bar, red hot glowing becomes white hot when further heated. The dependence is illustrated in figure 2.5, which shows how the energy output varies with the wavelength at several temperatures. A good approximation of this emission was given by Planck (Atkins 1999)

$$\rho = \frac{2hc^2}{\lambda^5} \left(\frac{1}{e^{hc/\lambda kT} - 1} \right) \tag{2.18}$$

where: $h = 6.62608 \times 10^{-34} \, Js$

$k = 1.381 \times 10^{-23} \, JK^{-1}$

$T = Absolute \ Temperatur$
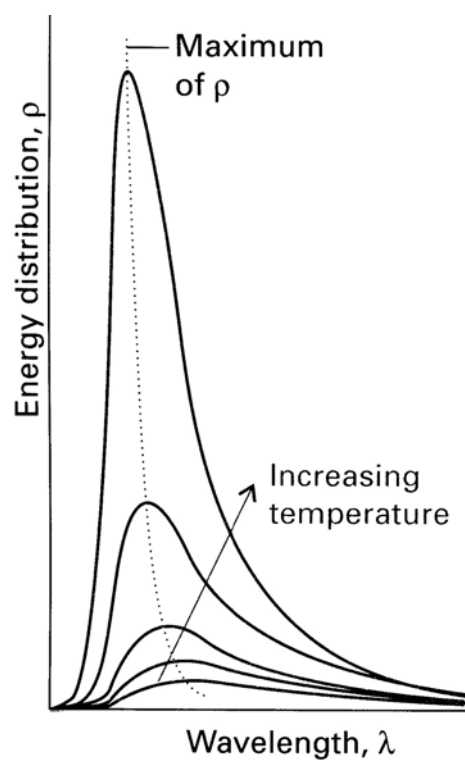
$c = 2.99792458 \times 10^8 \, ms^{-1}$

Figure 2.5: The energy distribution in a black-body cavity at several temperatures. The total energy density (the area under the curve) increases as the temperature is increased as T^4 (Atkins 1999).

3. Experimental Section

The experimental set up of the present work is described in this section. We describe first the preparation of the chemicals: $Ln-LnX_3$ ($Ln = Nd$, Ce; $X = I$, Cl) and ($LiX-KX$) eutectic mixtures. It is known that the $Ln-LnX_3$ melts attack aggressively ceramic materials yielding their oxihalides (Gmelin 1982). Up to now, no corrosion resistant ceramic material has been found. The only suitable materials for crucibles are Mo, Ta, W (Gmelin 1982) and glassy carbon (Jörger 1998). Tantalum is specially recommended for synthesis of rare earth dihalides at high temperature (Corbett 1983).

Due to the high corrodibility and high melting point of the $Ln-LnX_3$ systems, it was necessary to construct different types of optical cells, in which the salt reservoirs were Mo and glassy carbon crucibles. Only those measurements with pure LnX_3, $LnX_3-(LiX-KX)_{eu}$ and LnI_2-LnI_3 melts were performed with quartz cells. They are expected to be less corrosive. Details about these cells are given below.

In addition, a description of the Raman spectrometer is also presented as well as the procedure for recording the spectra in the different cells.

3.1 Preparation of Chemicals

The salts used in this work are extremely hygroscopic. The rare earth metals (Ln) are easily oxidized at the surface in the air atmosphere. Therefore, the materials were handled in a glove box (M. Braun) with an Ar atmosphere (O_2 and H_2O less than 2 ppm) and stored under vacuum in sealed quartz ampoules.

Ln Metals

Rare Earth metal (99.9%, Alfa) were cleaned shortly in HNO_3 and then rinsed with acetone in order to eliminate the oxide at the surface (Kvam 1998). The remaining oxide on the metal surface was removed mechanically in the glove box.

LnCl$_3$

NdCl$_3$ and CeCl$_3$ were synthesized from their oxides at the Technical University in Wroclaw, Poland. The NdCl$_3$ was synthesized according to the following scheme (Gaune-Escard 1994):

1. Chlorination of oxides: Nd_2O_3 + conc. $HCl_{aq} \rightarrow NdCl_3 \cdot 6H_2O$
2. Partial Dehydration: $NdCl_3 \cdot 6H_2O + NH_4Cl \rightarrow NdCl_3 \cdot H_2O + NH_4Cl$
3. Dehydration: $NdCl_3 \cdot H_2O + HCl(g) \rightarrow NdCl_3$

The NdCl$_3$ obtained in this way still contained traces of NdOCl, which is less volatile than NdCl$_3$. Thus, NdCl$_3$ can be further purified by distillation about 10 K above its melting points [T_m(NdCl$_3$)=758 °C (Bredig 1964)] with the equipment displayed schematically in Fig 3.1. Because of the reactivity of rare earth trihalide melts with quartz at high temperature, which results in the formation of oxyhalide, the distillation temperature must not exceed 920°C. Under an inert atmosphere, raw salt was introduced in a quartz reservoir, it was connected to the vacuum pump (~10^{-5} mbar) and the distillation was started. Only the left side of the reservoir was heated; for this reason, the distilled halides were deposited on the cold side (right side) whereas the residual salt remained in the left side. The distilled NdCl$_3$ was

carefully separated from the quartz reservoir under Ar atmosphere and stored in a glass ampoule which was sealed under vacuum. A typical distillation took 3 hrs.
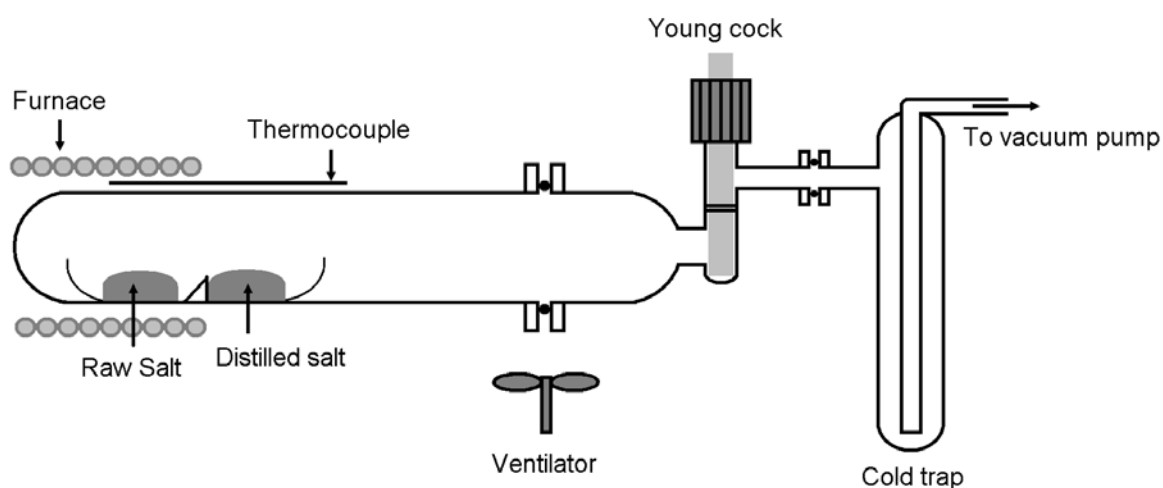

Fig 3.1: Distillation apparatus for rare earth trihalides.

LnI$_3$

Neodymium and Cerium triiodide were prepared by direct reaction of the metals with iodine vapor using a modified method of Druding and Corbett (Druding 1961, Bogacz 1999) at the Technical University in Wroclaw, Poland.

In the case of NdI$_3$, neodymium metal and iodine (10 mol% in excess with respect to stoichiometry) were loaded into a tantalum crucible, which was placed inside a quartz ampoule with a side arm and evacuated up to about 10^{-5} mbar. Then, the ampoule was heated up to 80°C. The temperature of the ampoule section with neodymium was gradually increased up to 800°C, whereas the temperature of the side-arm with iodine was increased up to 180°C for about 20 hours. This time was necessary for complete reaction. Finally, a vacuum sublimation was performed at 750°C during 60-70 hours. As product the light green, pure NdI$_3$ was obtained.

LnX₂

LnX₂ were prepared by reaction of stoichiometric amounts of LnX_3 and Ln metal (Technical University Wroclaw, Poland). The reagents were loaded into a tantalum crucible, which was placed inside the quartz reactor, filled with high purity argon (H_2O and O_2 = 1 ppm). The temperature of the reaction mixture was increased up to 850°C and kept during approx. 5 hours.

Alkali Halides (LiX and KX)

LiX and KX were acquired as follows: LiCl: 99.99% (Aldrich); KCl, 99.999% (Alfa); LiI, 99.999% (Alfa); KI, 99.99% (Alfa). The LiX and KX were dried and recrystallised in a furnace connected to a glove box. Each salt was first heated to 400 °C under vacuum in a glassy carbon crucible. After several hours argon gas was introduced inside the furnace, and then heated up slowly ca. 50 K above the melting point of the respective salt. Finally, the furnace was cooled at a rate of 1.5 K/h and the melt crystallized. After this treatment, impurities gathered in the center of the crystal could easily be removed.

LnX₂-LnX₃-(LiX-KX)ₑᵤ Mixtures

Since only the phase diagram of the $NdCl_3$-LiCl-KCl is known (Nakamura 1997), the mixtures of LnX₂-LnX₃ with (LiX-KX) eutectic systems were prepared with the proper amounts of salt mixtures in quartz ampoules at ca. 600°C in order to be certainly above the liquid lines for about one hour. The polycrystalline mixture was then powdered with a mortar. A slight corrosion of the ampoules was found for higher composition of the rare earth dichlorides.
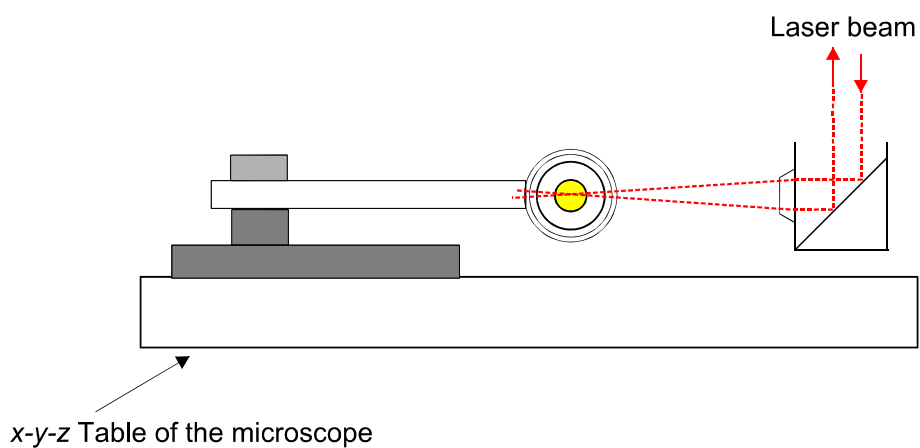
3.2 Construction of the Optical Cell

Because of the different corrosion characteristics of the molten salt systems, three kinds of optical cells were used in this work: quartz cell (cell 1), windowless cell with an internal furnace (cell 2) and windowless cell with an external furnace (cell 3). Windowless means that the liquid metal salt system does not have a direct contact with the guarding optical window (Young 1964, Quist 1971, Booker 1995, Dai 1998). Because the $Ln-LnX_3$ melts do attack the quartz aggressively it was necessary to use crucibles of Mo (Gmelin 1982) and glassy carbon (Jörger 1998) as melt reservoirs.

3.2.1. Cell 1: Quartz Cell

The optical quartz cell was made up of a cylindrical quartz tube (2 mm outer diameter and 30-40 mm length) and filled with the proper amount of lanthanide salts in the glove box. The filled cells were then sealed under vacuum using a glass blower torch. These optical cells were placed inside the furnace and positioned on the microscope table of the Raman system to get a good alignment for recording the spectra (Fig 3.2).

The furnace (Fig 3.2) was made of a standard heating alloy (Kanthal). It had a total length of 690 mm and an inner diameter of 3.2 mm. The windings had a spacing of about 1.5 mm, enough to illuminate the sample with the laser. This furnace was mounted inside a quartz carrier, which had an internal diameter of 8 mm and a length of 85 mm. The quartz carrier was fixed to the table of the microscope, which could be finally positioned in three dimensions with respect to the laser beam. The furnace was connected to a PID temperature controller (Eurotherm). A thermocouple was positioned between the furnace and the cell, which was calibrated in a preceding experiment with respect to the exact temperature of the sample using a second thermocouple inside the quartz cell.

Side view

Laser beam

x-y-z Table of the microscope

Top view

Quartz carrier

Quartz cell

Objective of the
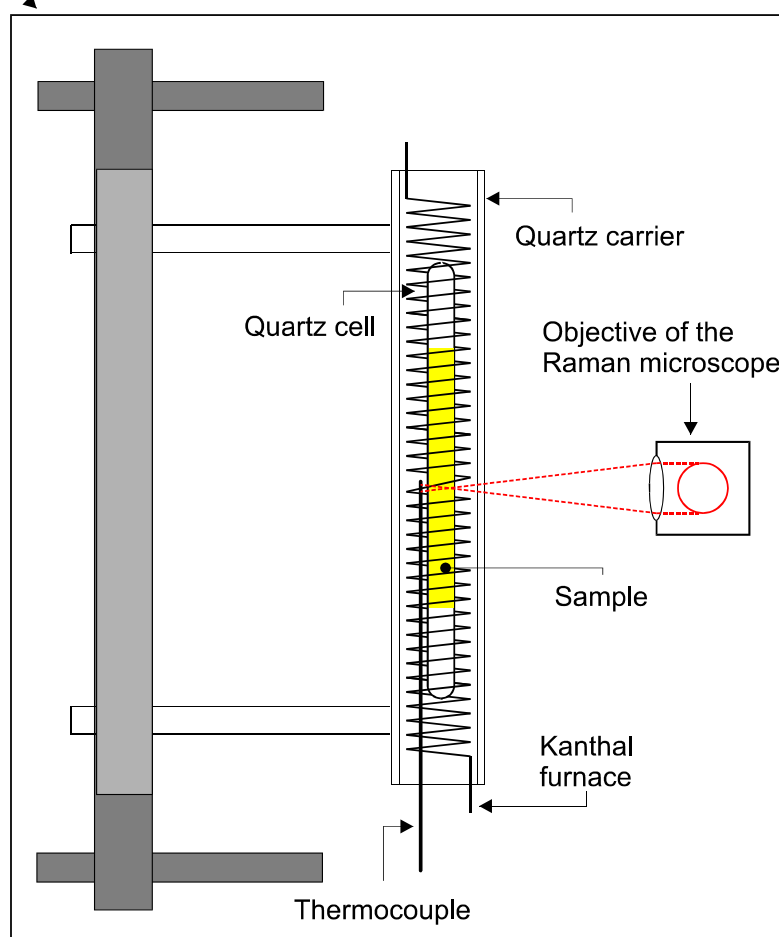Raman microscope

Sample

Kanthal
furnace

Thermocouple

Figure 3.2: Quartz cell (cell 1) and furnace.

3.2.2. Windowless Cell with Internal Furnace

The Fig 3.3 shows a sketch of a new windowless cell constructed in this work for high temperature Raman experiments. The sample was contained inside of an open molybdenum crucible. The crucible and the furnace are placed inside a chamber which can be evacuated or refilled with argon under high temperature conditions. The laser beam can be focused into the sample from outside the chamber.

The furnace has been constructed from molybdenum wire isolated by corund capillaries, appropriate for temperatures up to 1000°C, and was connected to a PID controller. The temperature was measured by two thermocouples: one in the furnace and one close to the sample. The outer window (optical window) was protected against condensation of the evaporating sample by a second movable window, which was only opened during the recording of the Raman spectra.

Unfortunately this sophisticated construction was not as successful as desired, due to the irreversible reactions of the sample with the Mo-heater via the gas phase. This is discussed later.

3.2.3. Windowless Cell with External Furnace

The experiences with cell 2 mentioned above led to a new cell construction. Again, glassy carbon served as crucible. This was placed inside a quartz tube, covered with an optical quartz window using graphite foil as sealing material (Fig 3.4). The filling and sealing procedure was carried out in the glove box. The quartz tube was then placed inside a cylindrical heating element as depicted in Fig 3.4. The furnace was connected to a PID controller. The laser beam of the Raman spectrometer was focused through the window into the sample.

For temperature calibration, a thermocouple was placed right in the middle of the crucible within the quartz tube. The reading of this thermocouple was compared at various temperatures with the thermocouple placed within the furnace.
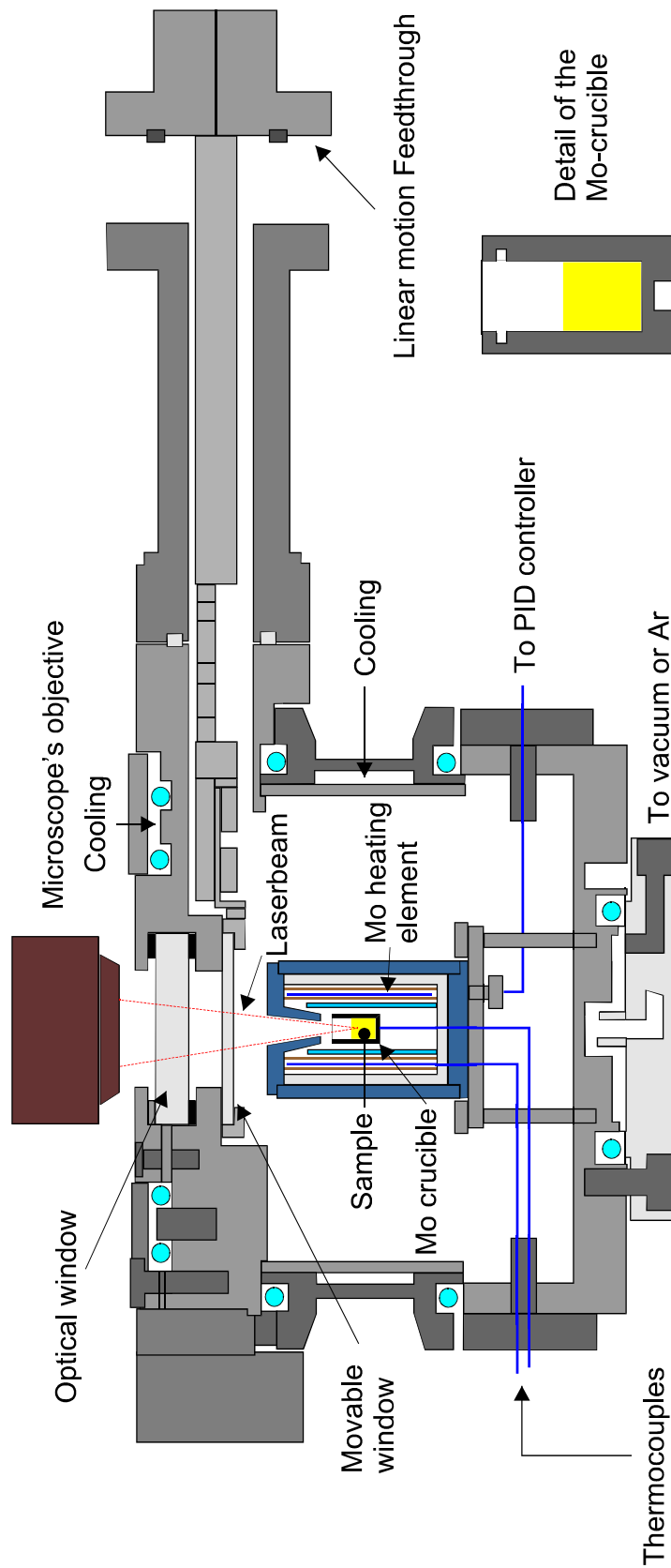
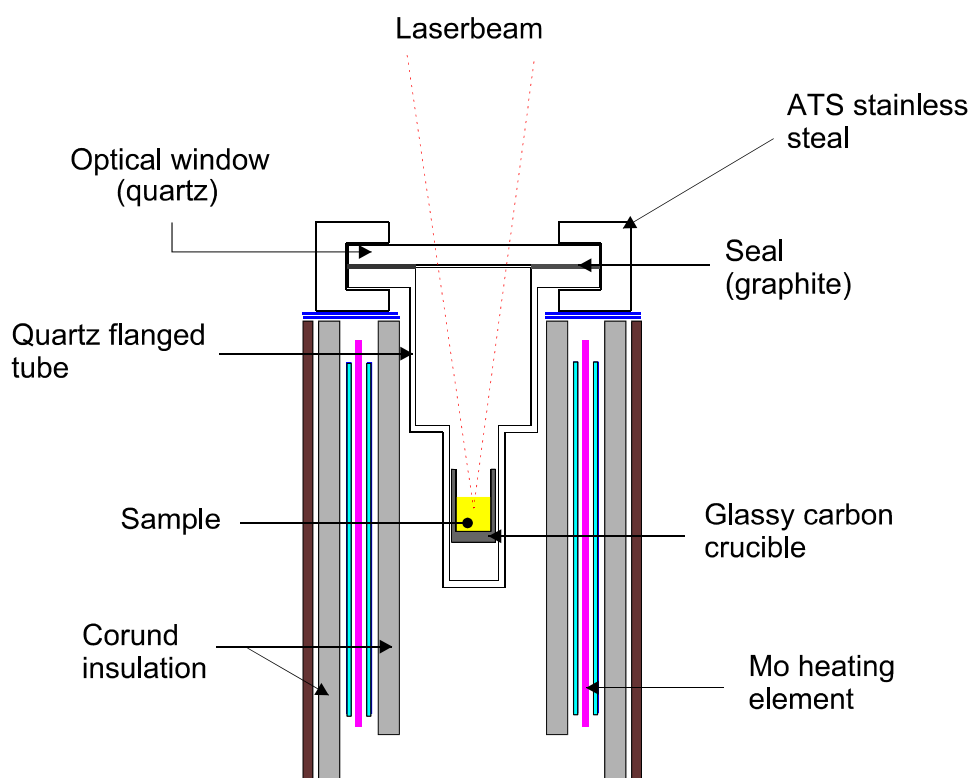Fig 3.3: Windowless cell with an internal furnace (cell 2).

Figure 3.4: Windowless cell with external furnace (cell 3).

3.3. Description of the Raman Spectrometer

The spectra were recorded using a commercial Raman spectrometer (LabRaman, Jobin Yvon, Dilor). The main features of the spectrometer system are as follows: the beam of the internal He-Ne Laser (λ_0=632.8 nm, 15802.78 cm^{-1}) is focused via suitable optics through the objective of a microscope onto the sample. In selected experiments, an external Ar-Laser (λ_0=514.5 nm, 19436.34 cm^{-1}) was employed. The scattered Rayleigh and Raman lights are collected by the same microscope objective.

The optical element for the suppression of the Rayleigh scattering is a notch filter. It acts as an extreme interference filter with a maximum optical density of 6.0, spectral bandwidth of 250 cm^{-1}. Due to the small but finite bandwidth of this filter, the lowest wave number that can reliably be measured is around 100-120 cm^{-1} for the He-Ne laser (Fig 3.5) and 50-70 cm^{-1} for the Ar laser. This depends on the setting of the notch filter angle using suitable spacers.

In addition, a polarizer was used in order to perform the two intensity Raman measurements: parallel (I_{II}) and normal ($I_{\perp}$) to the polarization of the electric field vector of the incoming laser beam. Behind the polarizer the light enters the monochromator; light detection is performed by a CCD camera.
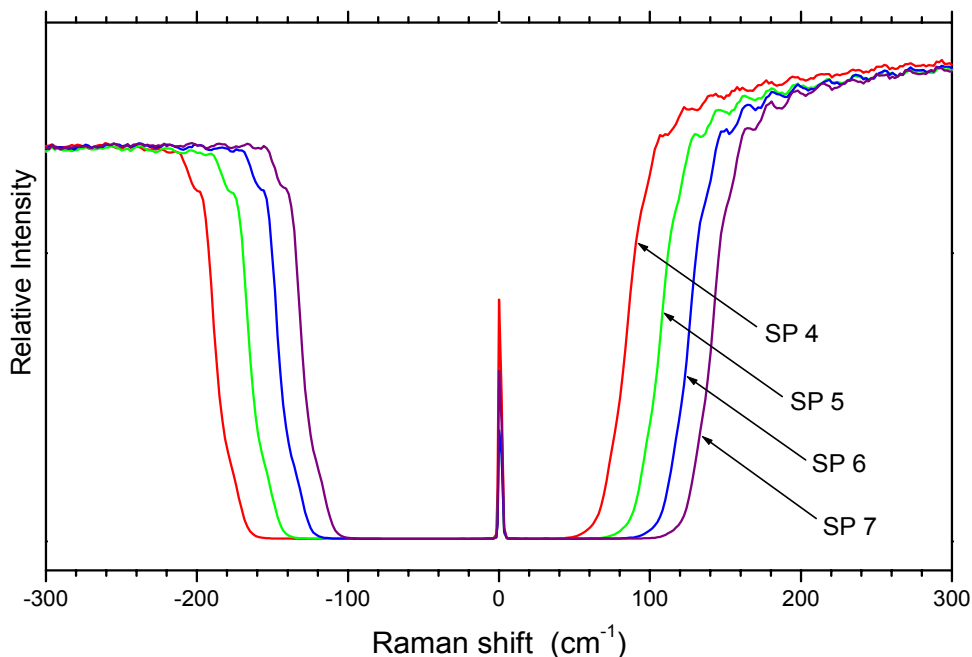

Fig 3.5: Transmission spectrum of the notch filter using a white lamp with different notch filter angles (SP in the figure means the different spacer numbers). At 0 cm^{-1} the breakthrough of the He-Ne laser is visible. The Rayleigh intensity is strongly attenuated. Note that the cut-off of the notch is often asymmetrical, to move the filter edge to lower wavenumbers. The position of the cut-off can be slightly changed with different spacers:

Spacer number (SP):	4	5	6	7
Diameter (mm):	7	8	9	10
Angle of the notch:	6.59°	5.69°	4.86°	4.05°

3.4. Experimental Procedures

3.4.1. Preparation of the Sample

Quartz cell (cell 1): The quartz tubes were cleaned with a mixture of acetone, petroleum ether and ethanol ("washing-up liquid") in an ultrasonic bath and heated to higher temperatures (~1000°C) under vacuum for a couple of minutes. Still hot (~100°C) they were

transferred into the glove box, filled with the right amounts of sample, and sealed under an argon atmosphere using a Young stop cock. After it, they were evacuated and sealed using a glass blower torch. Finally, the quartz cell was introduced into the respective furnace (see Fig 3.2).

Windowless cells (cell 2 and cell 3): The crucibles (Mo or glassy carbon), the flanged quartz tube (cell 3), and the optical windows of the cells 2 and 3, were washed with the washing-up liquid in an ultrasonic bath. Then the crucibles were placed into an induction furnace (Hüttinger), where they were heated up to 1000 °C under vacuum (~10^{-5} mbar) for a couple of minutes in order to eliminate volatile impurities. After that, they were transferred in a sealed quartz tube under argon into the glove box and filled with the right amount of sample.

In the case of the internal furnace (cell 2), the chamber with the furnace was also transferred into the glove box, the crucible was placed inside it and then the whole chamber was sealed under an Ar-atmosphere.

On the other hand, for the cell 3, the quartz flanged tube was introduced into the glove box and then the crucible with the sample was placed inside it. The quartz tube was sealed under an Ar-atmosphere and then introduced into the respective furnace (see Fig 3.4)

3.4.2. Recording of the Raman Spectra

Before recording a spectrum, it was necessary to calibrate the Raman spectrometer. One way for us to see if the spectrometer was perfectly calibrated was to record the spectrum of a Silicon sample. In this test, the Si ν_1 line should be found at 520.7 cm^{-1}.

After the calibration of the spectrometer, the beam was focused onto the powered sample by means of the microscope and the HV, VV and without-polarizer spectra were recorded at room temperature (25°C) in the Stokes and anti-Stokes range[1]. Then the sample was stepwise heated up in order to record the spectra at different temperatures. The maximal temperature at which the spectra were recorded was about 100 K above the melting point. A characteristic recording time was 30-60 s for the solids and of 120-300 s for the liquids.

---

[1] Since most Raman bands detected in our spectra lay in the spectral range below of 500 cm^{-1}, the Stokes and the anti-Stokes spectra were recorded in a single shot.

4. Experimental Problems, Spectra Analysis and Error Discussion

The Raman spectrum can be affected by many influences, including physical characteristics of the substances (e.g. fluorescence), undesired physical/chemical phenomena (e.g. cell corrosion), as well as influences of the instrument (e.g. calibration of the spectrometer). All these factors are of course sources for errors in the measurements and they should be considered when carrying out an interpretation of the Raman spectra.

4.1. Experimental Problems

4.1.1. Cell Corrosion

A substantial problem for the present work was the corrosion of the cell. As it was previously mentioned, at high temperatures the molten $Ln-LnX_3$ systems are very corrosive. In the case of quartz cells, the formation of silicon oxihalides is possible in the corrosion process (Gmelin 1982). These may interfere considerably in the observation of the Raman spectrum. This can be seen in Fig 4.1 at 500 cm^{-1} in the Raman spectrum of a NdI_3-NdI_2 mixture at 700°C.

The grade of corrosion of the cells was different in the measurements at high temperature. To give a rule of thumb for the corrodibility of the samples: it was higher for the chloride system than for the iodides, lower for the pure trivalent systems than for doped

systems (e. g. Ln-LnX$_3$ or LnX$_2$-LnX$_3$), and lower in eutectic alkali-halides mixtures as solvent. Finally, it was not surprising that the corrodibility increased with temperature. The selection of the system was not the only strategy to diminish this problem. We also employed windowless cells. However, as mentioned in the previous chapter, the corrosion of the Mo-parts of the furnace was also a problem. With the corrosion process via the gas phase new compounds were formed and the observed Raman spectra where strongly altered.
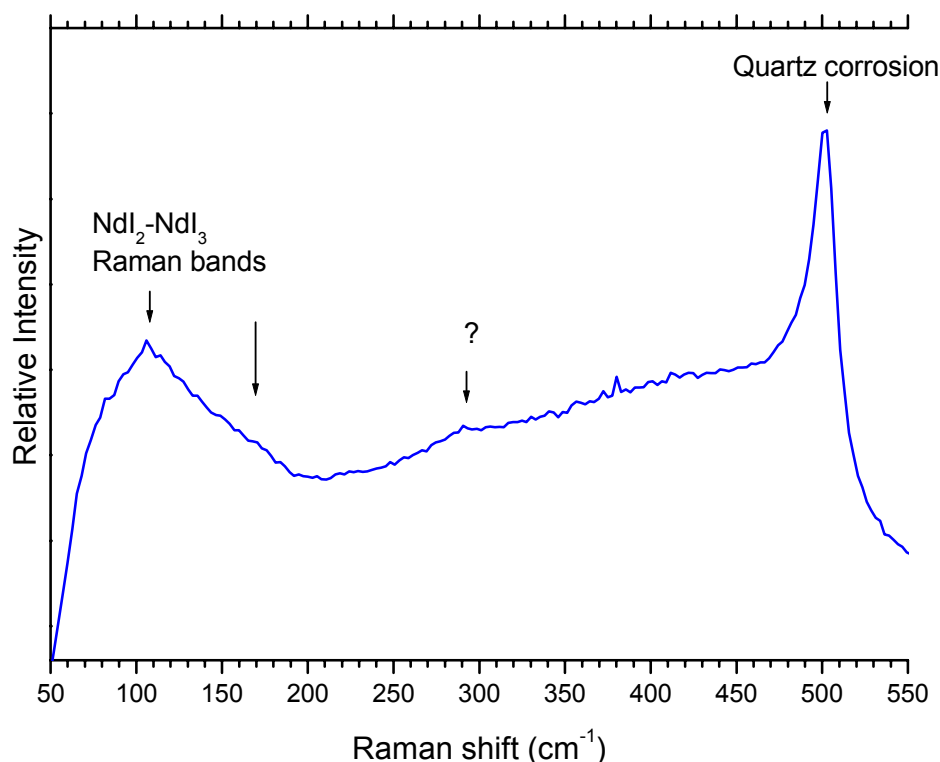

Figure 4.1: Raman spectra of molten NdI$_{3(0.5)}$-NdI$_{2(0.5)}$ at 700°C in the quartz cell. The spectra were recorded with an Ar laser (λ_0=514.5 nm), a notch filter angle of 4.05° and a recording time of 300 s. The very weak peak at about 280 cm^{-1} can not be exactly identified.

4.1.2. Background Emission of the Thermal Radiation

An additional problem was the blackbody radiation of the sample at elevated temperatures. This is caused by the detection technique of the Raman spectrometer which does not employ lock-in-amplifier technology.

Fig 4.2 shows the theoretical black-body emission at different temperatures, calculated with Planck's approximation (see chapter 2, section 2.9), for a range of wavelengths $\lambda_0 = 500$ nm to 650 nm. This range was chosen because it comprises the range of the two lasers used in the present work. In the temperature and the wavelength range of interest the blackbody emission increases not only with increasing temperature, but also with increasing wavelengths. Therefore, for measurements at high temperatures ($T \geq 600°C$), the use of a laser with low wavelength is more advisable. However, as we explain below, this may enhance the problem of fluorescence.
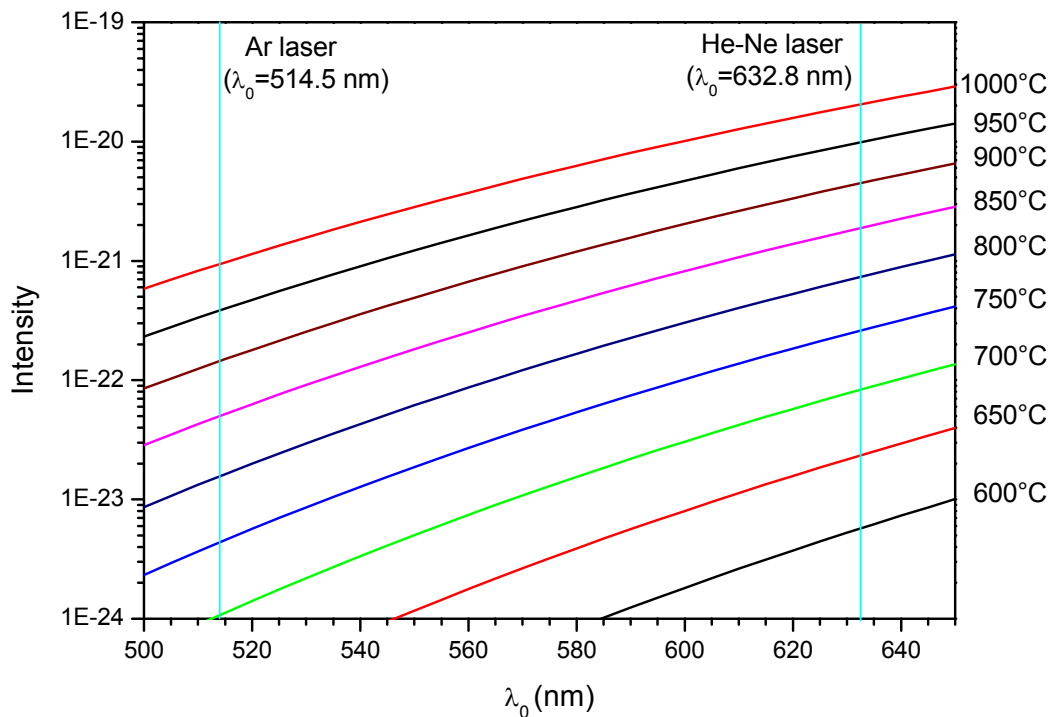

Figure 4.2: Dependence of the blackbody emission on wavelength at different temperatures. The curves were calculated with the Planck distribution (eqn 2.12, chapter 2, section 2.9)

The effect of the blackbody radiation in the typical spectral range of interest is depicted in Fig 4.3. It is interesting to note, that the background emission does not appear with the same intensity in every spectrum. It turned out that this influence depends on the nature of the sample and the possible advancement of corrosion. As an example, the spectra for dark samples, like LnX_2, have shown a higher background emission than the spectra of

LnX$_3$, whose salts are clearer, at the same temperature. In addition, the Raman spectra of strong Raman scatterers can be observed to higher temperatures.
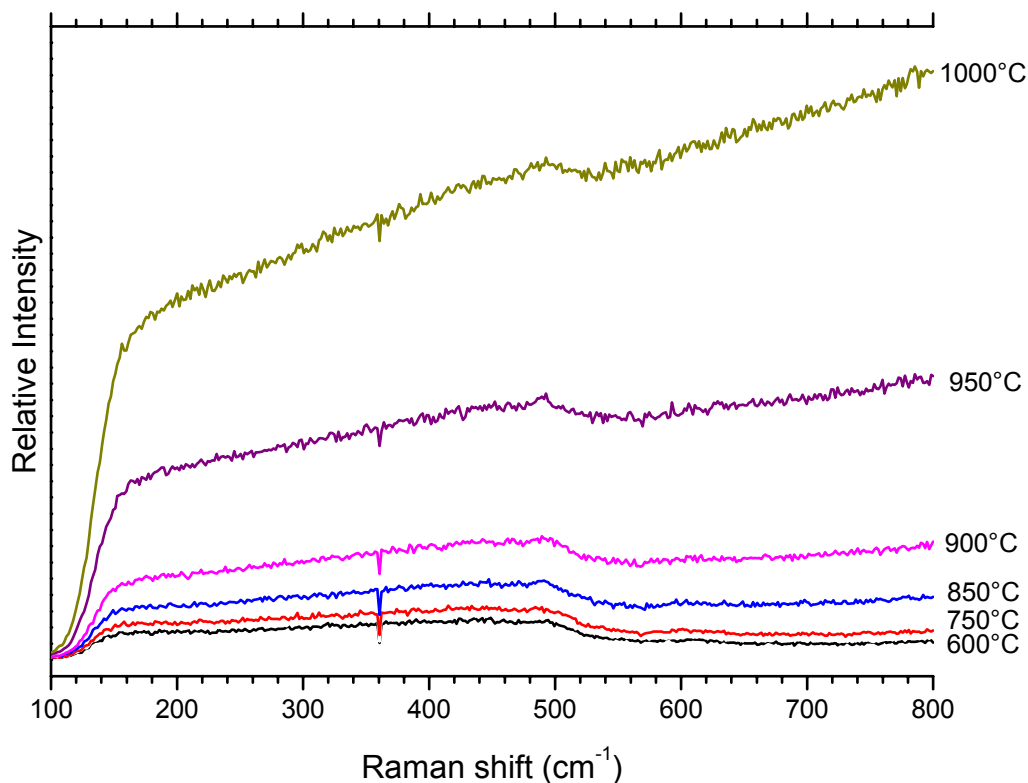

Figure 4.3: This figure shows the black body emission of the furnace and quartz cell as function of the temperature. The spectra were recorded with He-Ne laser (632.8 nm), 6.59° notch filter angle, without polarizer and an integration time of 20 s.

4.1.3. Fluorescence

Fluorescence can also have some influence on a Raman spectrum. It can be stronger than Raman scattering (Bulkin 1991). The example of solid and liquid NdCl$_3$ is shown in Fig 4.4. The strategy to reduce fluorescence is to use lasers with longer wavelength.

Because the fluorescence is normally red-shifted from the exciting line, it interferes with the Stokes spectrum but not with the anti-Stokes. Therefore, when the fluorescence

"obscures" the Stokes spectrum, it is possible for some samples to obtain a Raman spectrum by means of the anti-Stokes signal[1]. For $NdCl_3$ it was not difficult to determine the Raman bands, since the spectrum is known from the literature (Photiadis 1993, Photiadis 1998), which is not the case for NdI_3.
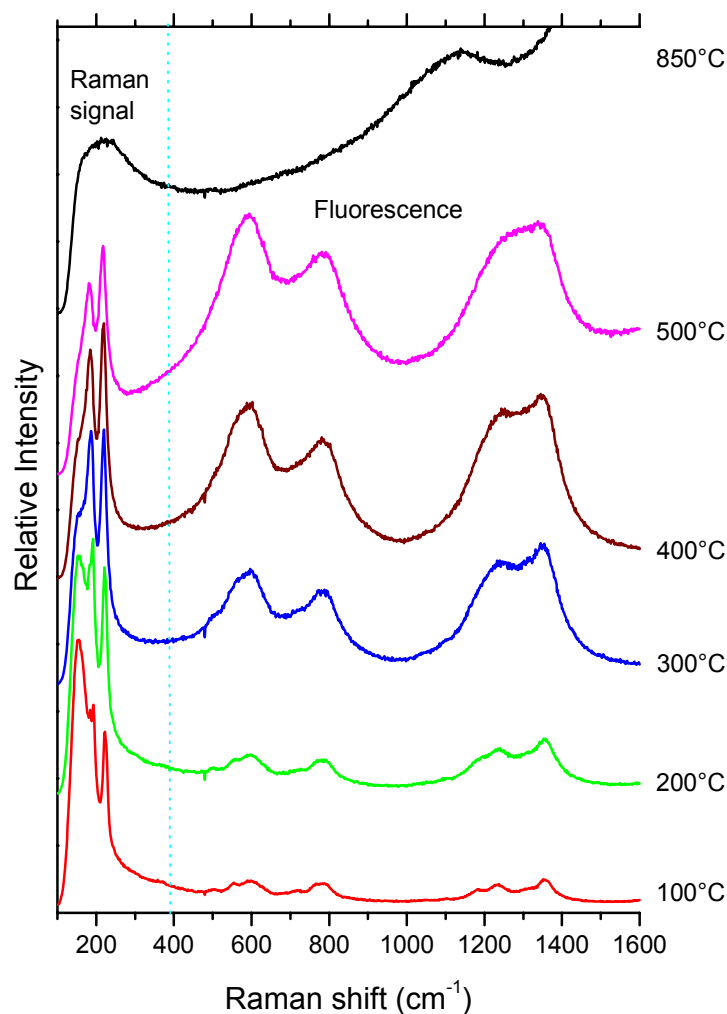

Figure 4.4: Raman and fluorescence spectra of $NdCl_3$ as function of the temperature in the quartz cell. The spectra were recorded with a He-Ne laser (λ_0=632.8 nm), 6.59° notch filter angle, without polarizer, 10 s of integration time. Below 400 cm^{-1} Raman signals can be obtained. Above is mainly fluorescence.

---

[1] In chapter 6 (Raman spectra of Ln-LnI$_3$) we will present the spectra obtained at different temperatures for LnI$_3$, where laser induced fluorescence appeared in both signals: Stokes and anti-Stokes.

4.1.4. Metal Dissolution in Rare Earth Halide-Alkali Halide Mixtures

Taking into account the problems of measuring the Raman spectra of the Ln-LnX_3 melts, we tried to eliminate the fluorescence, the corrosion problems, and the blackbody emissions at high temperatures, by studying the Ln-LnX_3 systems in mixtures with $(LiX$-$KX)_{eu}$. However, the phase diagrams of Ln-LnX_3-$(KX$-$LiX)_{eu}$ are not known in detail (Janz 1967) To obtain homogeneous samples we heated the mixture for some minutes to about 800°C prior the Raman experiment, since the liquidus lines are not known. Furthermore, it is sometimes difficult to assign the spectra to a specific melt concentration. The compositions mentioned in this work are always the weighted, nominal compositions.

4.1.5. Film Formation

It was observed in several measurements of metal doped melts that the quartz window was covered with a thin opaque film. This strongly disturbed the Raman spectra. These film deposits were analyzed with electron microscopy. The corresponding element identification is shown in Fig 4.5. The approximate composition was estimated to be Nd:Cl=1:3. The most probable mechanism for this effect is sublimation of a component of our mixture. As a consequence the measurements had to be performed fast.

4.2. Data Analysis and Error Discussion

4.2.1. Analysis of the Experimental Data

In order to obtain the main characteristics of the Raman bands (maximum frequency, integrated intensity, depolarization degree, and band width), it is necessary to perform a correction of the spectra.
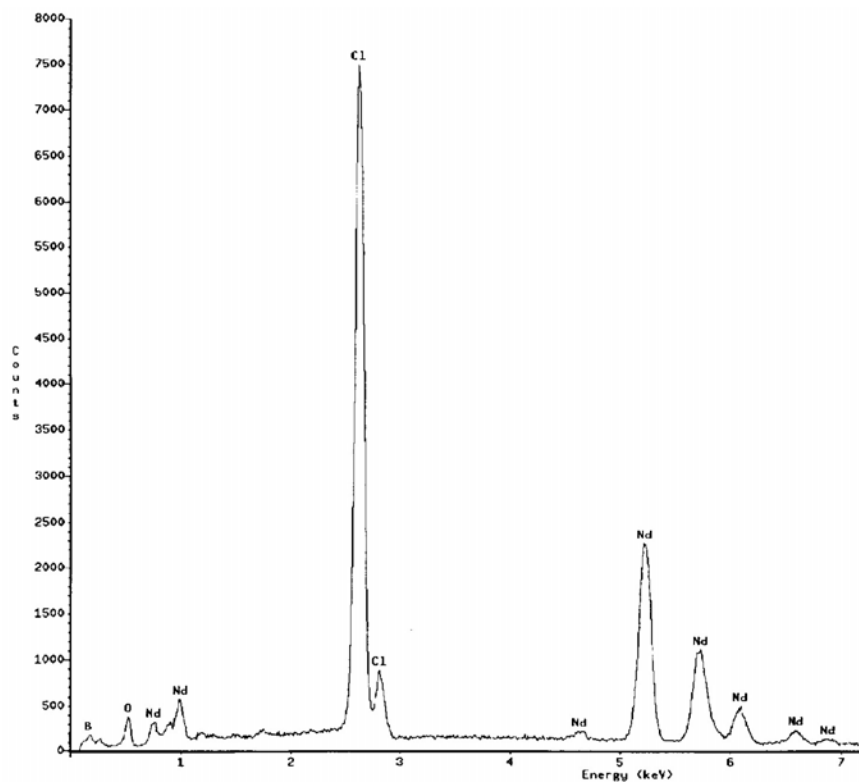
Figure 4.5: Electron microscope analysis of a typical film deposit on the quartz optical window in an Nd-NdCl$_3$ melt. Each peak was assigned to a corresponding element (Laboratorium für Elektronen Mikroskopie, Universität Karlsruhe).

As it was mentioned in chapter 3, section 3.3, the Raman spectrometer in the present work had a notch filter for the suppression of the Rayleigh scattering. For this reason, the spectra recorded with the He-Ne laser were cut off at 120 cm^{-1} (Fig 3.5) and at 70 cm^{-1} for those recorded with the Ar laser. Subsequently, for the spectra recorded at T $\geq$ 400°C, a baseline correction was performed by subtracting an artificially constructed background from the Raman spectra. It has to be mentioned, that the uncertainty of this baseline is a significant source of error (Bulkin 1991, Bulmer 1975) and its choice can often be the limiting factor in the quantitative analysis. In this work we use the Labspec® software package supplied with the spectrometer.

Figs 4.6 *a* and *b* show schematically how this baseline correction had influence on the analysis of the Raman intensities. We show the very difficult case of NdI$_{3(0.5)}$-NdI$_{2(0.5)}$. This spectrum suffered from strong quartz corrosion, and a base line hardly discernable. The background subtraction was performed using two different interpolation functions: one linear

and one polynomial (5th degree). The obtained values with the two different baseline corrections differ considerably strong for the integrated intensities for all bands. The band width is less influenced (exception: the small band around 280 cm^{-1} which is hardly recognizable) but the peak position is nearly unaffected.

To be able to perform a comparative analysis of the spectra it was necessary to use the same baseline correction scheme for all spectra.
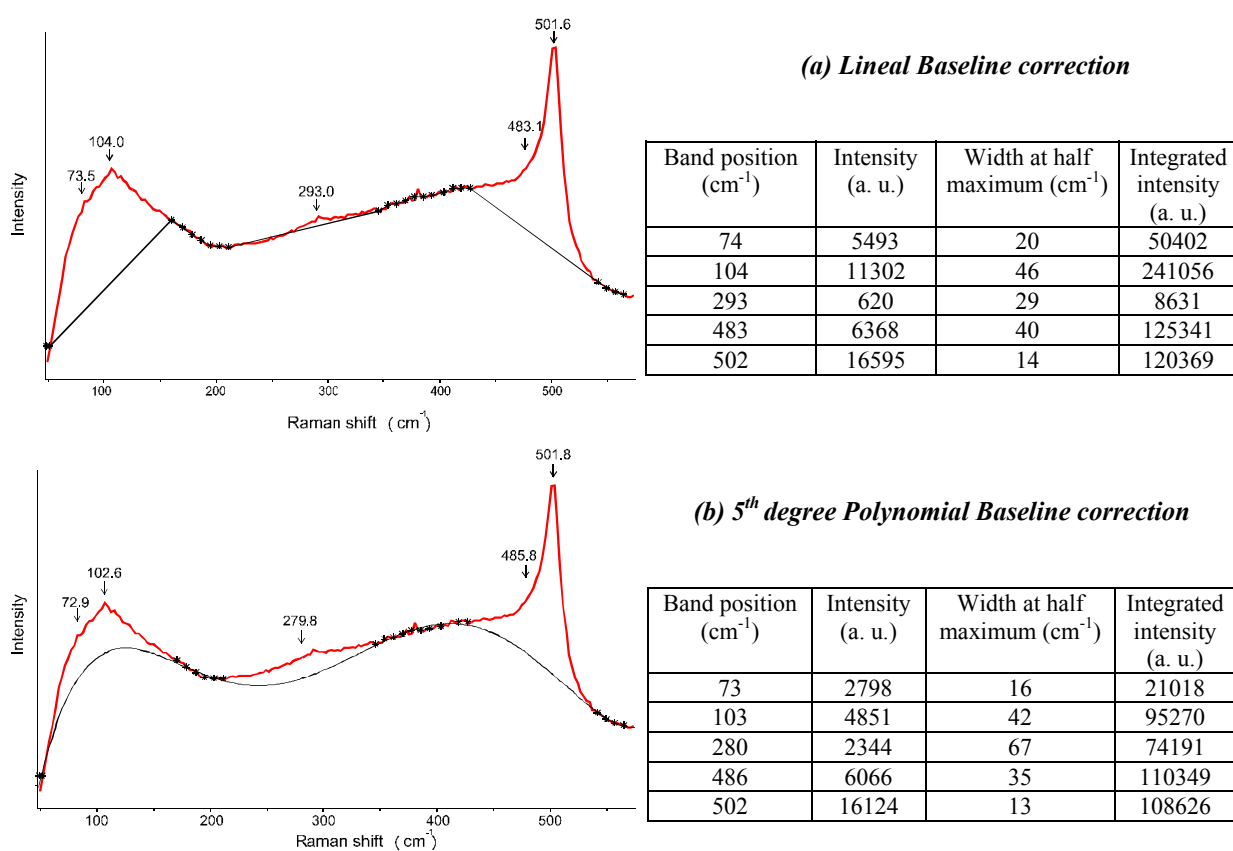

(a) Lineal Baseline correction

Band position (cm^{-1})	Intensity (a. u.)	Width at half maximum (cm^{-1})	Integrated intensity (a. u.)
74	5493	20	50402
104	11302	46	241056
293	620	29	8631
483	6368	40	125341
502	16595	14	120369

(b) 5th degree Polynomial Baseline correction

Band position (cm^{-1})	Intensity (a. u.)	Width at half maximum (cm^{-1})	Integrated intensity (a. u.)
73	2798	16	21018
103	4851	42	95270
280	2344	67	74191
486	6066	35	110349
502	16124	13	108626

Figure 4.6: a) Lineal and b) Polynomial baseline subtraction and fitting of the resulting bands of the liquid NdI$_{3(0.5)}$-NdI$_{2(0.5)}$ spectrum, in the quartz cell. The spectrum was recorded with the Ar laser (514.5 nm), 4.05° notch filter angle, without polarizer and an integration time of 120 s. The presented data are just an approximation; for this reason, the error for each date does not appear in this table.

After this correction, we were able to fit the peaks using different band shapes, like Gaussian, Lorentzian, or a combination of both. For this objective, we used the Origin® software package. An example is given in Fig 4.7.
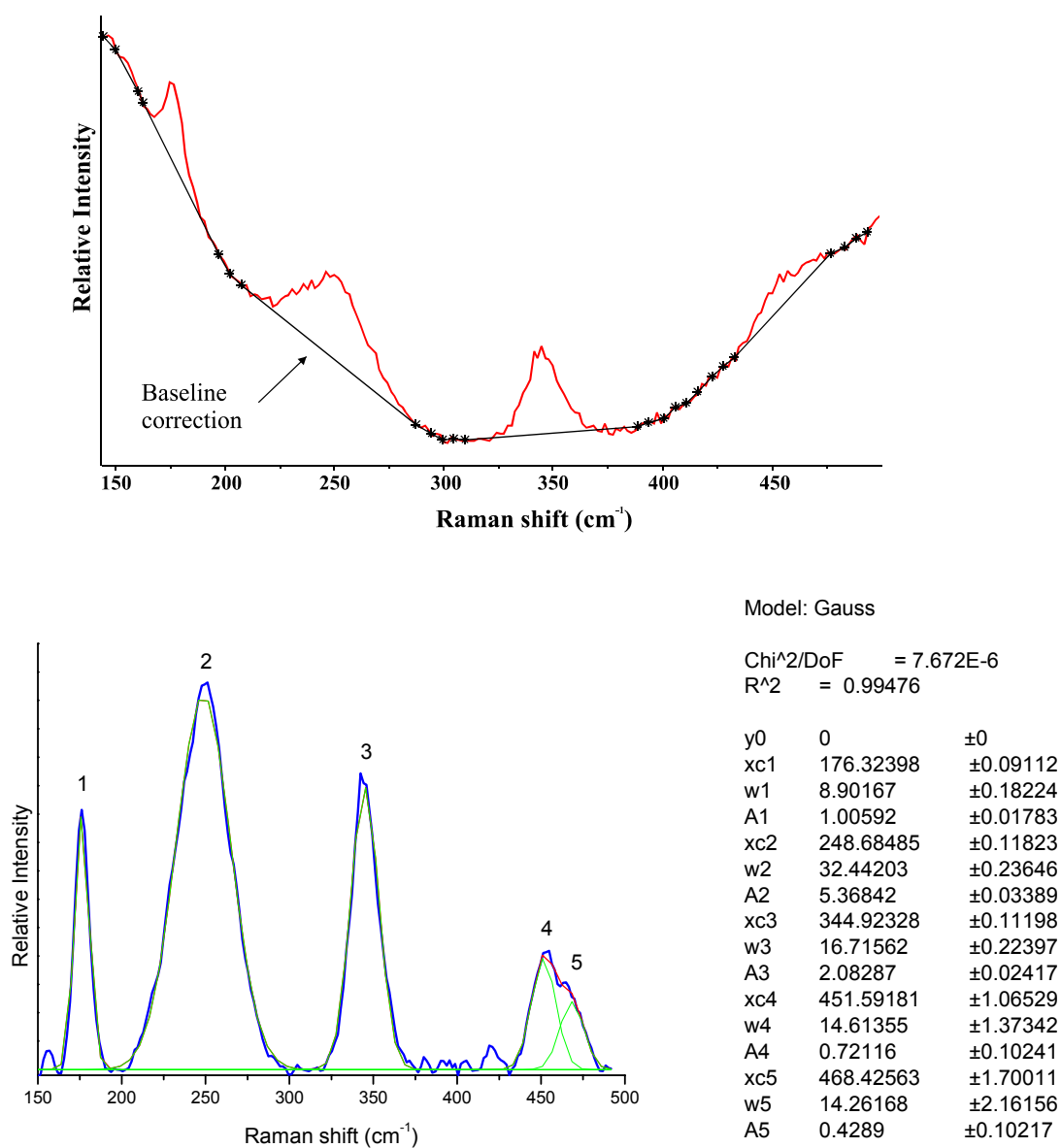
Model: Gauss

Chi^2/DoF   = 7.672E-6
R^2   = 0.99476

y0	0	±0
xc1	176.32398	±0.09112
w1	8.90167	±0.18224
A1	1.00592	±0.01783
xc2	248.68485	±0.11823
w2	32.44203	±0.23646
A2	5.36842	±0.03389
xc3	344.92328	±0.11198
w3	16.71562	±0.22397
A3	2.08287	±0.02417
xc4	451.59181	±1.06529
w4	14.61355	±1.37342
A4	0.72116	±0.10241
xc5	468.42563	±1.70011
w5	14.26168	±2.16156
A5	0.4289	±0.10217

Figure 4.7: Data analysis of a spectrum of liquid $(NdCl_3)_{0.05}$-$(NdCl_2)_{0.01}$-$(LiCl-KCl)_{eu, 0.94}$. The procedure:
1. Baseline correction with Labspec®
2. Fitting of the bands with Origin®

Notation: $xc = \nu$ (cm^{-1}, peak position), w = width at half maximum (cm^{-1}), A = band area (a. u.)

4.2.2. Error Discussion

In this section we describe the error analysis based on the mentioned experimental conditions and difficulties. For this reason, all the following influences should be considered in the interpretation of the Raman spectra.

Wave number: Beside the wave number calibration with the Rayleigh break through and the Si-sample, we employed for each sample an intrinsic check of the wave number calibration. In most cases we measured the Stokes and anti-Stokes spectra. The peaks had to be symmetrically grouped around the central Rayleigh peak. In this way a wave number precision of ± 1 cm^{-1} was achieved.

Intensities: The intensities are strongly affected by the base line correction. A qualitative error can only be given when the Raman bands are not too broad and clearly above the background. Consequently, the integrated intensity can be just a measure for the order of magnitude or it can be a number with a precision of a few percent.

Temperature: The error of the temperature is mainly caused by the temperature gradient across the sample (especially true for cell 1) and by the fact that we only measure the temperature of the furnace. The calibration was obtained by separate experiments where a second thermocouple instead of the sample was used, and by comparison of the temperature reading with known phase diagram data (like melting point). In such a way the temperature error was estimated to $\pm 5°C$.

Concentration: The main contribution to the concentration error is the lack of the phase diagram data for some of the investigated systems. This is difficult or even impossible to estimate. The concentration error arising from weighting uncertainties is relatively small. The mol fraction error was: $\delta x \approx \delta y = \pm 0.001$ for $(LnX_2)_x$-$(LnX_3)_y$ and $\delta x \approx \delta y = \pm 0.0015$ for mixtures in LiX-KX eutectic solvent.

5. Raman Spectra of Ln-LnCl₃ (Ln = Nd, Ce) Melts

In this chapter representative Raman spectra of Ln-LnCl₃ are presented. A large number of spectra have been accumulated and stored in digital form, but the most representative spectra are shown here in order to give an overall descriptive picture of the systems studied. The spectra are presented in the conventional form: intensity (I, I_{VV} and I_{HV}) vs. Raman shift.

If not quoted otherwise the conditions of the spectrometer for the recording of the Raman spectra were the following: the samples were excited with a He-Ne laser (λ_0=632.8 cm⁻¹), the notch filter angle was 6.59°, confocal hole aperture of 200 μm, grating of 1200 g/mm, slit aperture of 100 μm. The used microscope objective was an achromatic lens with 50 mm focal length. The spectra were recorded for different concentrations of Ln-LnCl₃ at various temperatures and in some cases as function of the time.

Additionally, a common feature of all Raman spectra shown in this chapter is the strong decrease of the relative intensity in the range between 100 and 120 cm⁻¹. This is due to the notch filter characteristics, as explained in the chapter 3, section 3.3.

5.1. Nd-NdCl₃

5.1.1 NdCl₃

The Raman spectra of liquid NdCl₃ were recorded with and without polarizer in the quartz cell and are shown in Fig 5.1. These spectra were compared with those published previously by Photiadis et al. (Photiadis 1993 and Photiadis 1998). They find two polarized bands (P₁ and P₂) and two depolarized bands (D₁ and D₂), which are attributed to the distorted octahedral $NdCl_6^{3-}$ species.
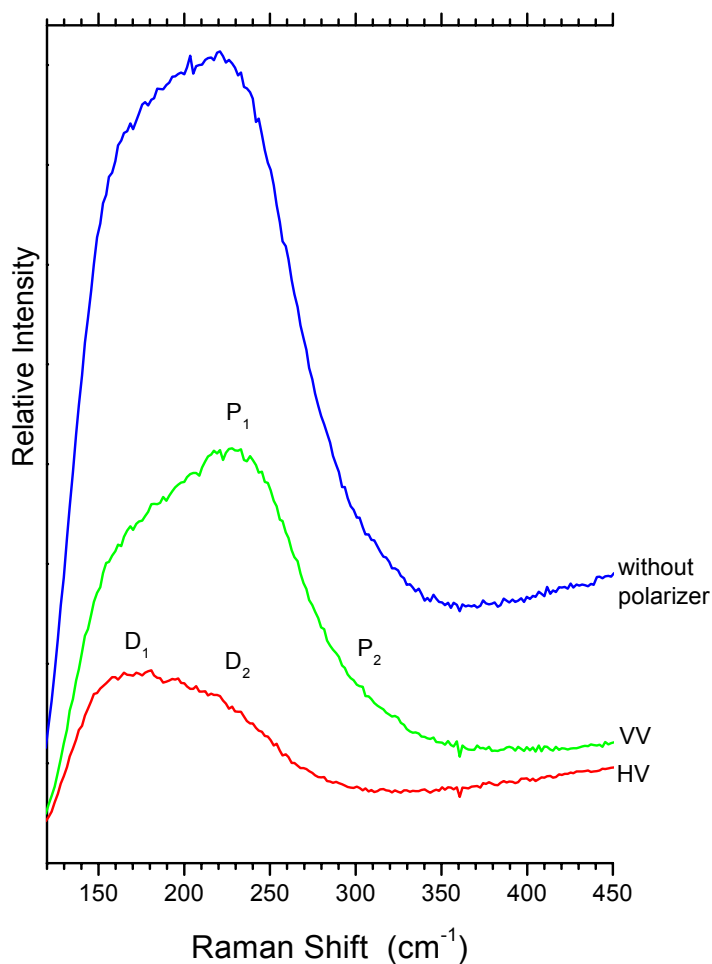

Figure 5.1: Raman spectra of NdCl₃ liquid at 800°C, with and without polarizer, in cell 1. The spectra were recorded with the He-Ne laser (λ_0=632.8 nm), a 6.59° notch filter angle and an integration time of 120 s. (a) HV: the electrical vector of the incident light is perpendicular to the electrical vector of the excited light. (b) VV: the electrical vector of the incident light is parallel to the electrical vector of the excited light.

As mentioned before, for pure $NdCl_3$ there is no problem with corrosion of the quartz cell at high temperatures, but with lanthanide metal doping of lanthanide halides mixtures, ion which we are interested, the problem of the cell corrosion is high, and it was necessary therefore to use an open *windowless cell*.

In order to test the constructed windowless cell (cell 2), we recorded the spectrum of the liquid $NdCl_3$ (Fig 5.2) and compared with the spectrum using cell 1. The spectrum recorded in the cell 2 shows four main relatively sharp bands (v_1', v_1, v_3 and v_4, respectively), while in the spectrum of the cell 1 only two main overlapping bands can be identified.
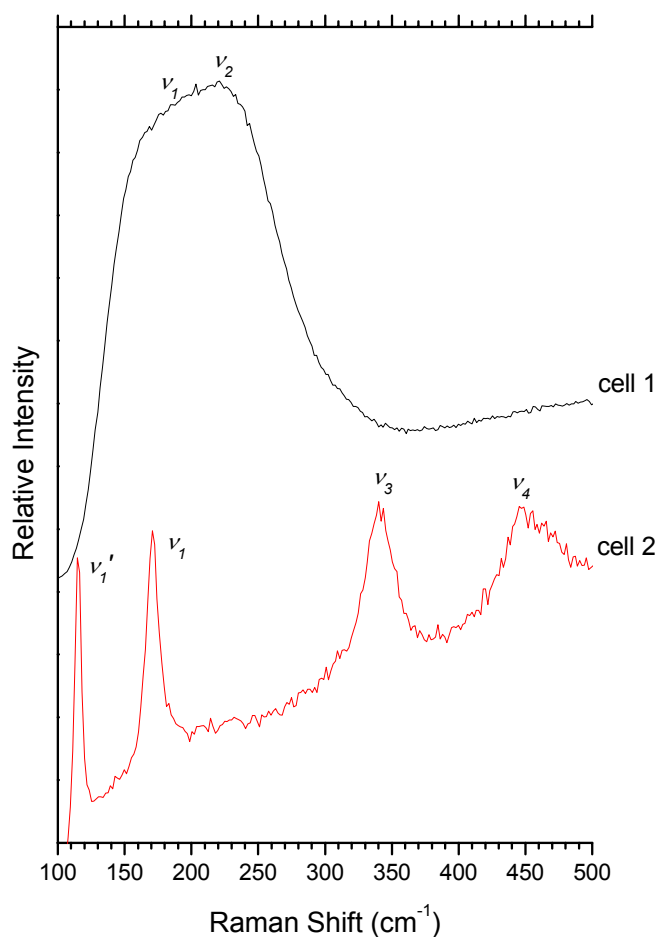
Figure 5.2: Raman spectra comparison of liquid $NdCl_3$ with the quartz cell (cell 1) and with the windowless cell (cell 2) at 800°C, without polarizer, 120 s of integration time and the same conditions as the spectra in Fig 5.1.

After this surprising result, the spectra were recorded at various temperatures. The development of these spectra is shown in Fig 5.3, starting with pure solid $NdCl_3$ (25°C). Up to

a temperature of 300°C is possible to observe the v_1 (~176 cm^{-1}) and v_2 (~208 cm^{-1}) bands, which correspond to the solid NdCl$_3$ (Photiadis 1998). Surprisingly, the character of the spectra changed strongly at 400°C: three new bands v_1', v_3 and v_4 appear (~116 cm^{-1}, ~347 cm^{-1} and ~456 cm^{-1}, respectively). At 550°C the band v_2 disappears and the bands v_3 and v_4 become stronger. In the temperature range between 550°C and 760°C the only change was a strong increase of the black-body background emission. This is also surprising since, at 760°C, the NdCl$_3$ is expected to be liquid (Bredig 1964). The characteristic Raman bands exhibit a small shift to lower wave numbers with increasing temperature.
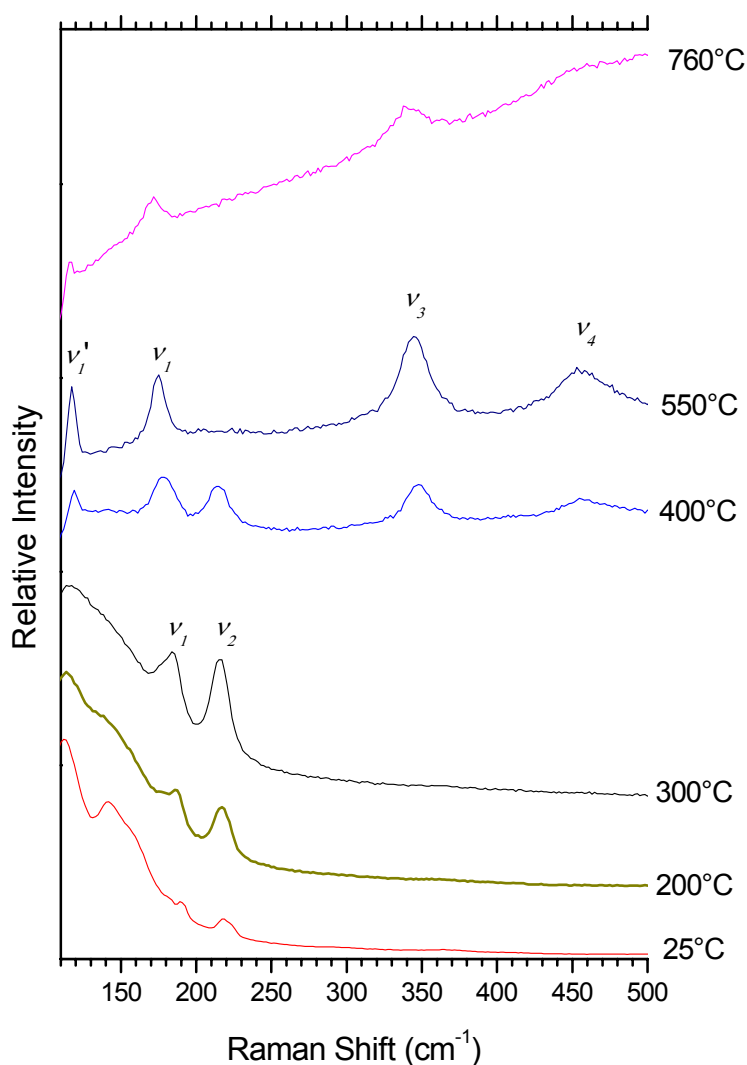
Figure 5.3: Raman spectra of NdCl$_3$ at various temperatures in the windowless cell with internal furnace. The spectra were recorded without polarizer at the same conditions as in Fig 5.1.

A concluding note about our findings: at temperatures above 300°C the Raman spectra of $NdCl_3$ recorded in the cell 2 have no similarity with those previously published by Photiadis et al. (Photiadis 1993). Furthermore, the strong change of the characteristics of the spectra indicates a decomposition of $NdCl_3$ in the cell 2. A possible decomposition reaction would be:

$$NdCl_3 \rightarrow NdCl_2 + 1/2 \; Cl_2,$$

i.e. producing $NdCl_2$ in the crucible. Volatile Cl_2 may give rise to corrosion products acting with the hot metallic parts in the cell 2 (eventually the Mo-wiring of the furnace).

5.1.2. NdCl₂

Under the assumption that in cell 2 a reduction reaction of $NdCl_3$ occurs, we recorded the spectra of $NdCl_2$ and compared with those obtained for $NdCl_3$ in the cell 2; but before this we recorded the spectrum of solid $NdCl_2$ in the cell 1 at 25°C as control. These latter spectra are shown in Fig 5.4, with and without polarizer.

The HV and the VV spectra are almost the same: in both cases the four main bands (v_1', v_1, v_3 and v_4) appear, being only different in the intensity. Furthermore, the spectra differ only in a weak polarized band (v_2') at about 215 cm^{-1}. The comparison of Figs 5.3 and 5.4 reveals that the main strong bands of $NdCl_2$ appear above 400°C in "pure" $NdCl_3$ measured in cell 2. This observation strongly supports the idea of a reduction reaction in cell 2. A collection of spectra in the cell 1 at various temperatures was not possible due to the high corrodibility of the salt.
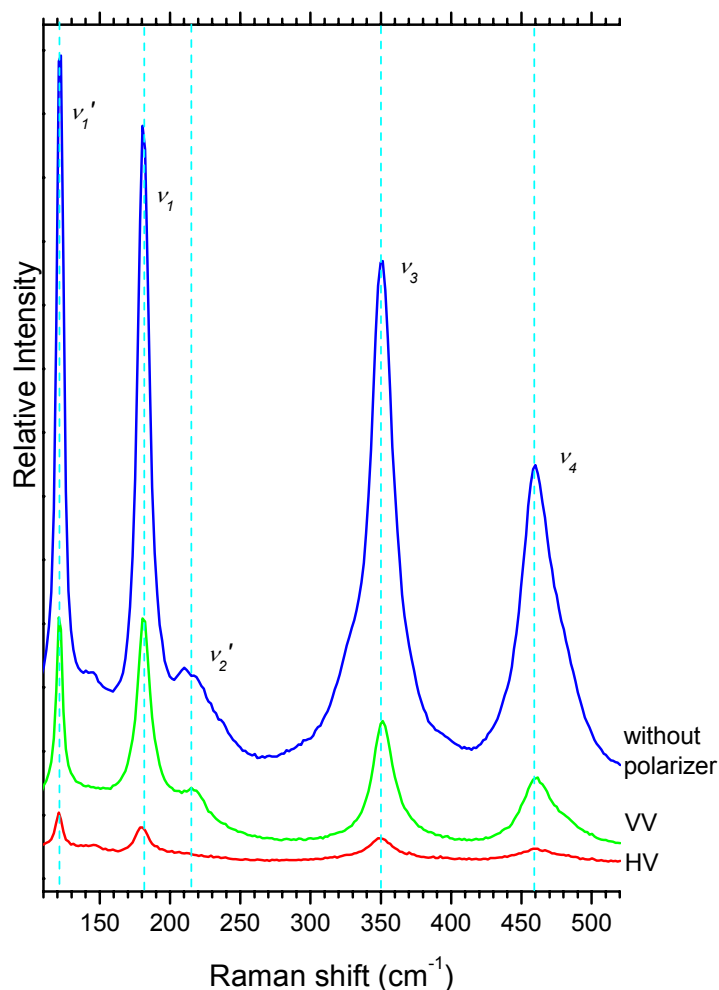
Figure 5.4: Raman spectra of $NdCl_2$ with the quartz cell (cell 1) at 25°C, with and without polarizer and 20 s of integration time. All spectra were recorded at the same conditions as in Fig 5.1. (Lines are added for a better localization of the bands).

In Fig 5.5 are shown the Raman spectra of solid $NdCl_2$ measured in the windowless cell 2 at various temperatures. The spectrum at 25°C is in agreement with the unpolarized one of Fig 5.4. However, the intensity of v_2' seems somewhat higher. This band seems to split off into two bands with the increasing of the temperature. The other bands v_1, v_3 and v_4 seem to be more intensive when heating. It is difficult to judge the intensity of band v_1' since it is very close to the notch filter edge.

A surprising fact in this series of spectra (Fig 5.5) is that a background emission increases considerably with the rise of the temperature, even though these spectra did not

exceed 300°C. At temperatures over 300°C it was almost impossible to obtain a spectrum due to the high background emission.
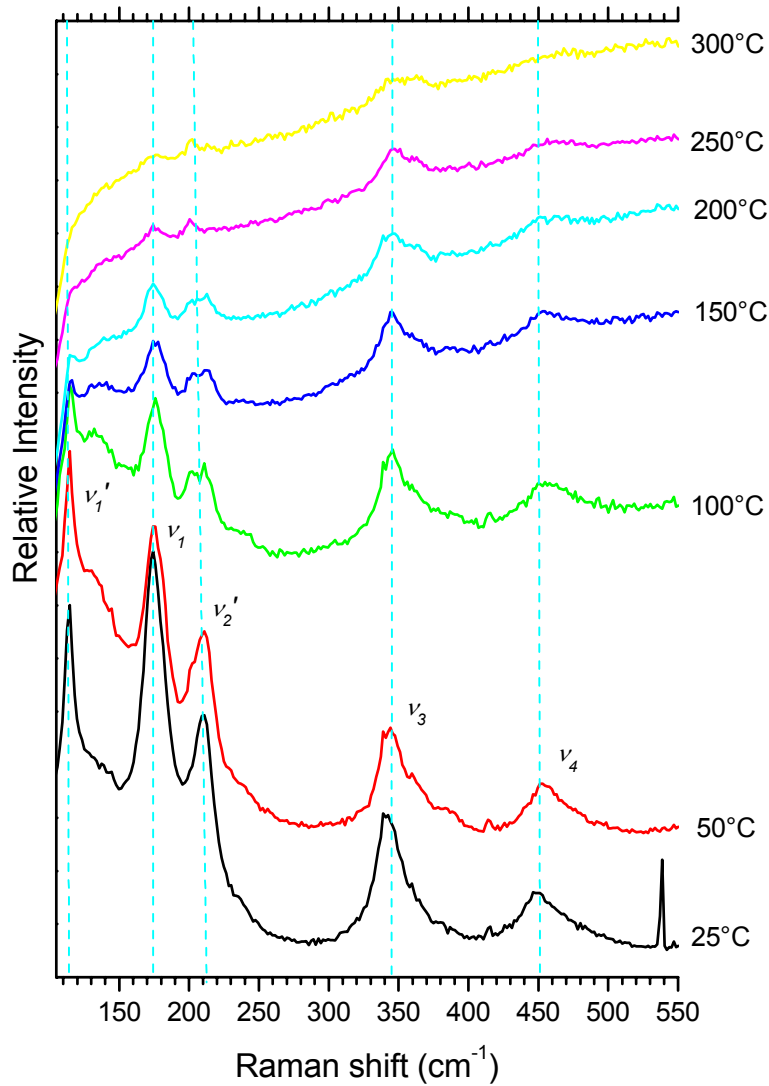
Figure 5.5: Raman spectra of $NdCl_2$ in the cell 2 at various temperatures. All spectra were recorded without polarizer and at the same conditions as in Fig 5.1.

5.1.3 $(NdCl_3)_x -(LiCl-KCl)_{eu, 1-x}$

In order to be able to measure at lower temperatures, to avoid the blackbody background emission and to diminish the corrosion, it was necessary to use an inert low

melting salt as solvent. For this, the LiCl-KCl eutectic (x_{KCl}=0.415, Janz 1967) was a promising candidate.

The Raman spectra of liquid $(NdCl_3)_{0.10}$-$(LiCl\text{-}KCl)_{eu,\ 0.90}$ measured in the cells 1 and 2 are shown in the following figures (Figs 5.6 and 5.7, respectively). In the spectra of cell 1 (Fig 5.6) a strong polarized band at about 250 cm^{-1} (ν_2) is observed, which is completely in agreement with the literature, and attributed to normal octahedral $NdCl_6^{3-}$ species (Photiadis 1993 and Photiadis1998). By means of this comparison is possible to establish the position of a depolarized band (D_1) at ~132 cm^{-1}. This band is difficult to observe in our spectrometer since it interferes with the notch filter edge.
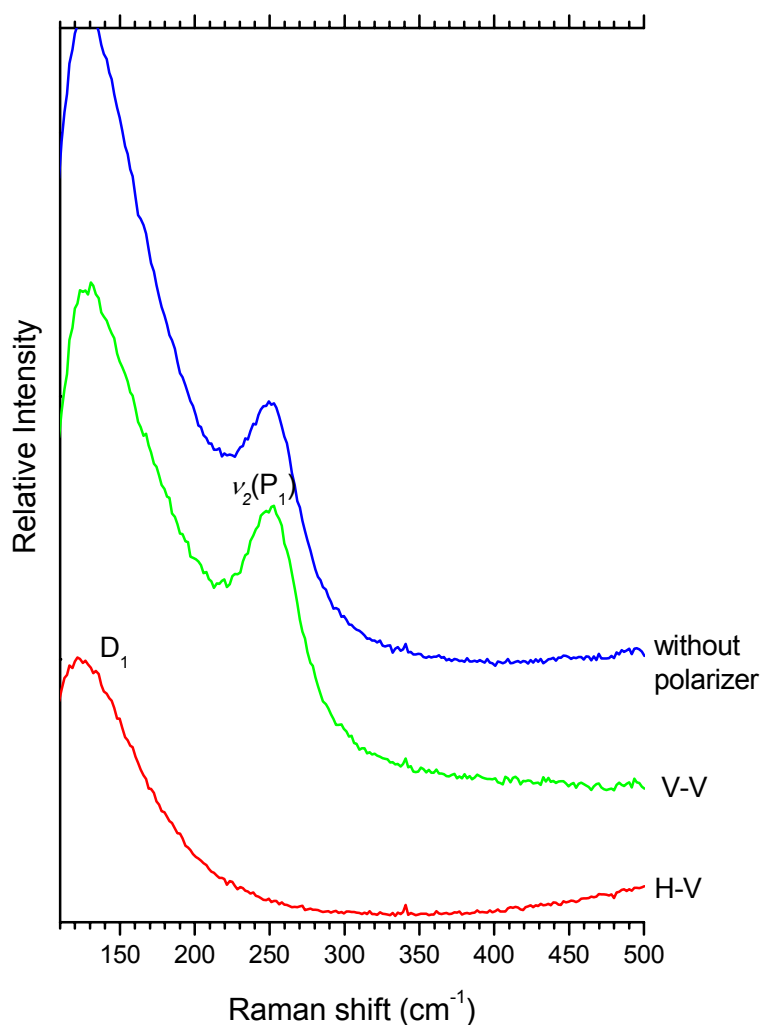
Figure 5.6: Raman spectra of liquid $(NdCl_3)_{0.10}$-$(LiCl\text{-}KCl)_{eu,\ 0.90}$ at 500°C, with and without polarizer. The spectra were recorded at the same conditions as the previous spectra and with a integration time of 120 s.

The same system, $(NdCl_3)_{0.10}$-$(LiCl\text{-}KCl)_{eu,\ 0.90}$, was studied in the windowless cell with internal furnace (cell 2), with molybdenum and glassy carbon crucibles. As can be seen in Fig 5.7, similar reduction patterns have been obtained in both cases (see bands ν_1', ν_1, ν_3 and ν_4). The polarized band ν_2 at 250 cm^{-1} persists with lower intensity. It should be also noted that the band ν_2' (ca. 210 cm^{-1}), which was observed in $NdCl_2$, does not appear under the present experimental conditions. We can conclude for the moment that in the melts, and in this special cell 2, an equilibrium between dissolved $NdCl_6^{3-}$ species and solid or liquid $NdCl_2$ exist.
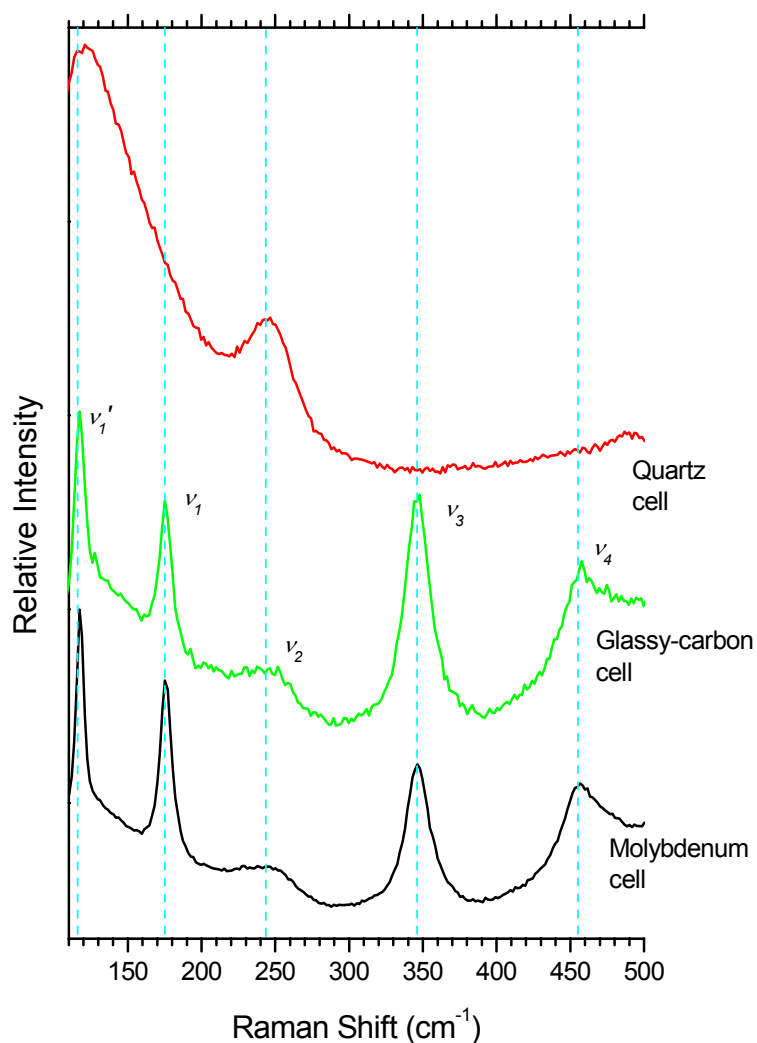
Figure 5.7: Comparison of the Raman spectra of liquid $(NdCl_3)_{0.10}$-$(LiCl\text{-}KCl)_{eu,\ 0.90}$ in the quartz, glassy-carbon and Mo-cells at 500°C, without polarizer and at the same conditions as before. The glassy-carbon and Mo-cells are of the cell type 2.

Additionally, we observed corrosion in the Mo-parts of the equipment, although we operated at a lower temperature (500°C) and at lower concentration of $NdCl_3$. Therefore, we used glassy carbon as cell material. A new series of spectra was recorded at various temperatures, with and without polarizer, and the result was remarkably always the same (see appendix A.2.2). It is interesting to note, comparing Fig 5.7 and appendix A.2.2, that the spectra are really the same, supporting the idea of a vapor-phase reaction.
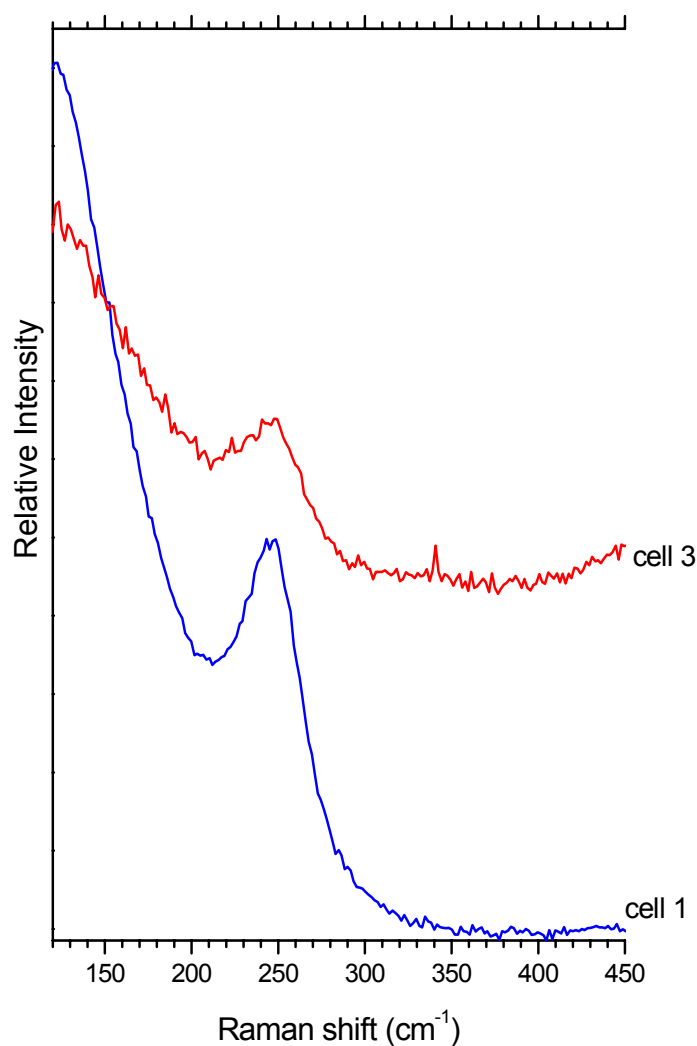
Figure 5.8: Comparison of the Raman spectrum of liquid $(NdCl_3)_{0.10}$-$(LiCl-KCl)_{eu,\ 0.90}$ at 500°C in the cell 1 (quartz) and the cell 3 (windowless with external furnace). The spectra were recorded without polarizer and at the same conditions as in Fig 5.1.

So as to finally solve this corrosion problem we carried on the spectroscopic experiments with the externally heated windowless cell (cell 3; for further details see section 3.2.3). In order to test this new cell type we recorded once again the spectrum of the mixture $(NdCl_3)_{0.10}$-$(LiCl\text{-}KCl)_{eu,\ 0.90}$. This time the spectrum agreed with that one in the quartz cell and with the literature (Fig 5.8). The resolution in the cell 3 was worse because, after some time, sublimated salt deposited on the optical window, interfering with the spectrum. In such a manner, the above mentioned reduction reaction was avoided, and we were able to record the spectra of different $(NdCl_3)_x$-$(NdCl_2)_y$-$(LiCl\text{-}KCl)_{eu,\ 1\text{-}x\text{-}y}$ melts.

5.1.4. $(NdCl_2)_y$ -$(LiCl\text{-}KCl)_{eu,\ 1\text{-}y}$

The spectra of $(NdCl_2)_y$-$(LiCl\text{-}KCl)_{eu,\ 1\text{-}y}$ mixtures were recorded in the cells 2 and 3. It was not possible to obtain any analyzable spectrum with cell 1 due to the corrosion of the quartz cell, although very low concentrations (y = 0.05) have been employed. Only with the windowless cells was possible to get reliable spectra (Fig 5.9). We recorded the spectra at various temperatures. The spectra in solution with eutectic were very similar to those for the pure solid $NdCl_2$. Above 500°C the presence of a considerable blackbody background emission was observed, which made impossible to observe any band. Unfortunately, the phase behavior of $NdCl_2$-LiCl-KCl system is not known and, therefore, we do not know the solubility of $NdCl_2$ at various temperatures. For this reason, before a measurement, the mixtures were heated up until 800°C for some minutes.

Fig 5.9 shows a temperature series spectra of $(NdCl_2)_{0.10}$-$(LiCl\text{-}KCl)_{eu,\ 0.90}$ after preheating and homogenizing the mixture. The spectrum at 25°C is very complex and shows many bands, which are presumably due to a new structure between $NdCl_2$ and eutectic ($Li_yNd_xK_zCl_{1\text{-}x\text{-}y\text{-}z}$). These spectra demonstrate that $NdCl_2$ was partially dissolved since the characteristic bands of the pure salt (the four main bands v_1', v_1, v_3 and v_4) are clearly observed. In addition, we can see that this complex structure disappears with increasing temperature, and the structure of pure $NdCl_2$ is finally reached. At 500°C the signal to noise ratio becomes worse due to the sublimation of the salt on the quartz window, although the $NdCl_2$-bands are still visible.
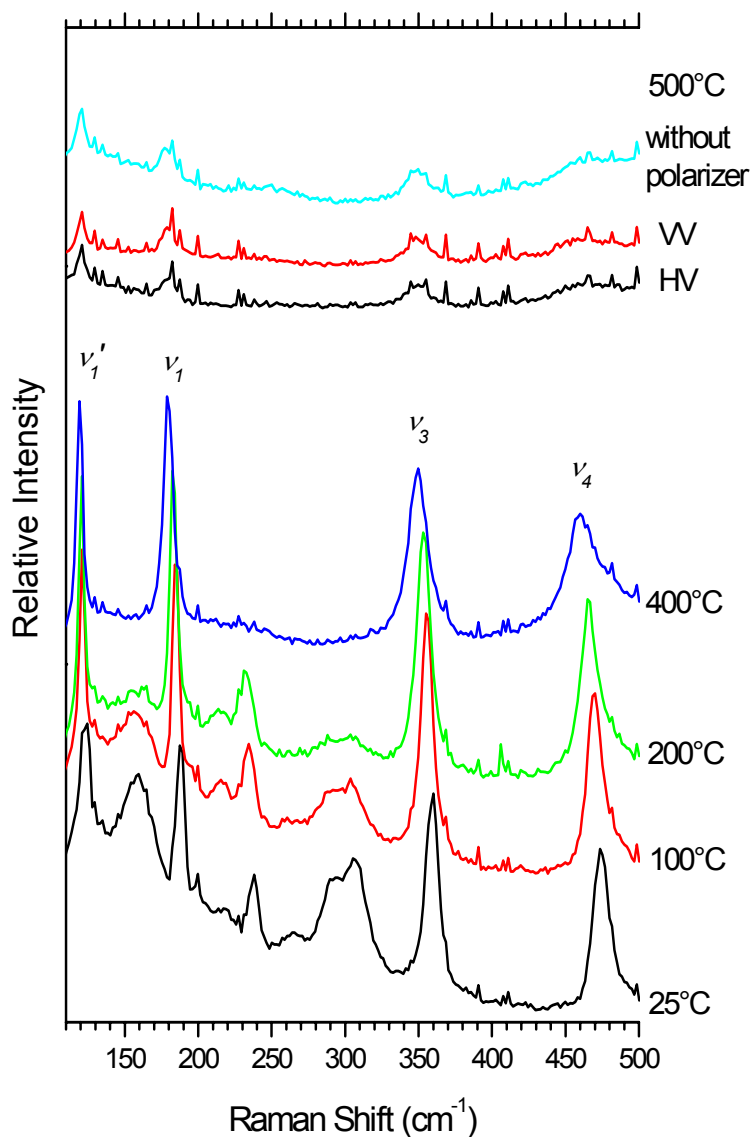
Figure 5.9: Raman spectra of preheated $(NdCl_2)_{0.10}$-$(LiCl-KCl)_{eu,\ 0.90}$ at various temperatures in the cell 3 (windowless with external furnace) without polarizer. The HV- and VV- spectra were recorded for the liquid mixture at 500°C and 500 s of integration time. All spectra were recorded at the same conditions as in Fig 5.1. The low resolution was caused by the sublimate deposited on the optical window

5.1.5. $(NdCl_3)_x$-$(NdCl_2)_y$-$(LiCl-KCl)_{eu,\ 1-x-y}$

Fig 5.10 shows a series of Raman spectra of $(NdCl_3)_x$-$(NdCl_2)_y$-$(LiCl-KCl)_{eu,\ 1-x-y}$ mixtures; the mole fraction x and y are given in the figure's caption. The spectrum *a* shows

the well known spectrum of the normal octahedral $NdCl_6^{3-}$ species in the $(NdCl_3)$-$(LiCl$-$KCl)_{eu}$ melt. Besides, the band ν_2 spectrum *b* (y=0.01) shows the relatively intense bands ν_1 and ν_3 (~ 116 cm^{-1} and ~ 342 cm^{-1} respectively). The bands ν_1' and ν_4 are weakly identifiable.
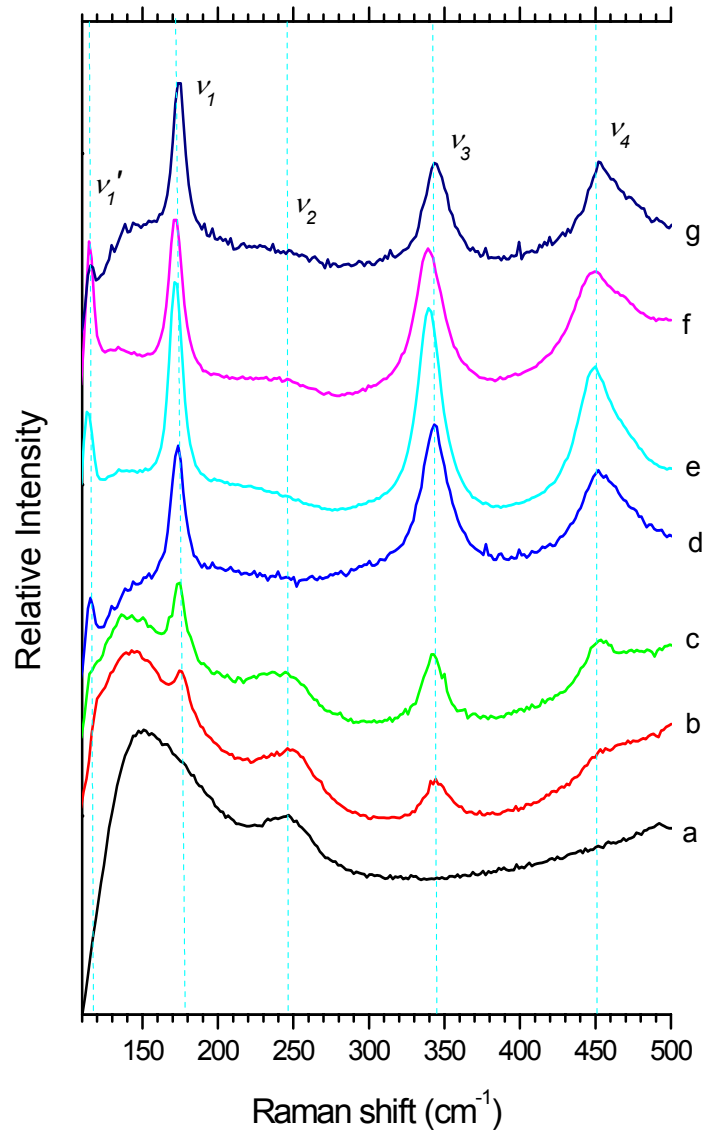
Figure 5.10: Raman spectra of $(NdCl_3)_x$-$(NdCl_2)_y$-$(LiCl$-$KCl)_{eu,\ 1-x-y}$ melts without polarizer, 120 s of integration time and at the same conditions as Fig 5.1.
   a) $(NdCl_3)_{0.05}$-$(LiCl$-$KCl)_{eu,\ 0.95}$ at 450°C.
   b) $(NdCl_3)_{0.05}$-$(NdCl_2)_{0.01}$-$(LiCl$-$KCl)_{eu,\ 0.94}$ at 500°C.
   c) $(NdCl_3)_{0.05}$-$(NdCl_2)_{0.02}$-$(LiCl$-$KCl)_{eu,\ 0.93}$ at 500°C.
   d) $(NdCl_3)_{0.05}$-$(NdCl_2)_{0.03}$-$(LiCl$-$KCl)_{eu,\ 0.92}$ at 530°C.
   e) $(NdCl_3)_{0.05}$-$(NdCl_2)_{0.04}$-$(LiCl$-$KCl)_{eu,\ 0.91}$ at 600°C.
   f) $(NdCl_3)_{0.05}$-$(NdCl_2)_{0.05}$-$(LiCl$-$KCl)_{eu,\ 0.90}$ at 600°C.
   g) $(NdCl_2)_{0.05}$-$(LiCl$-$KCl)_{eu,\ 0.95}$ at 600°C.

At higher NdCl$_2$ concentrations $(0.02 \leq y \leq 0.05)$ the NdCl$_2$ bands increase continuously and, even though the NdCl$_3$ concentration is constant (x=0.05) in spectra *a* to *f*, the intensity of the ν_2-band decrease. Concluding the results of Fig 5.10: those NdCl$_2$ species which dominate the spectra of the solid salt (Fig 5.4), and the spectra of a mixture of NdCl$_2$ with LiCl-KCl-eutectic (Fig 5.9), are also present and presumably unaltered in the (NdCl$_3$)$_x$-(NdCl$_2$)$_y$-(LiCl-KCl)$_{eu, 1-x-y}$ mixtures.

5.2. Ce-CeCl$_3$ Melts

5.2.1. CeCl$_3$ and (CeCl$_3$)$_x$-(LiCl-KCl)$_{eu, 1-x}$

CeCl$_3$ has the same molecular structure as NdCl$_3$ (C$_{6h}$, crystal form; Brown 1968, Gmelin 1982). For this reason, one can expect that the spectra in the solid and liquid state are similar in character. The spectra of pure CeCl$_3$ liquid are not presented here because the melt point of the pure salt is 812°C (Mellors 1959), and at this temperature the emission of the blackbody background is very high, which makes it impossible to observe analyzable bands (see spectra in appendix A.4.2). On the other hand, at lower temperatures (~500°C), a solution of CeCl$_3$ in (LiCl-KCl)$_{eu}$ can be studied (Fig 5.11).

Fig 5.11 shows the Raman spectra of (CeCl$_3$)$_{0.25}$-(LiCl-KCl)$_{eu, 0.75}$ melt (500°C) with the conventional quartz cell (cell 1). In these spectra one can see a strong polarized band ν_2 at ~235 cm^{-1}, resembling that of NdCl$_3$ at ~250 cm^{-1} (Fig 5.6). Until now, no Raman spectra of (CeCl$_3$)$_x$-(LiCl-KCl)$_{eu, 1-x}$ melts have been published in the literature, but comparing with those of NdCl$_3$ it is obvious to attribute the observed bands to octahedral $CeCl_6^{3-}$ species.
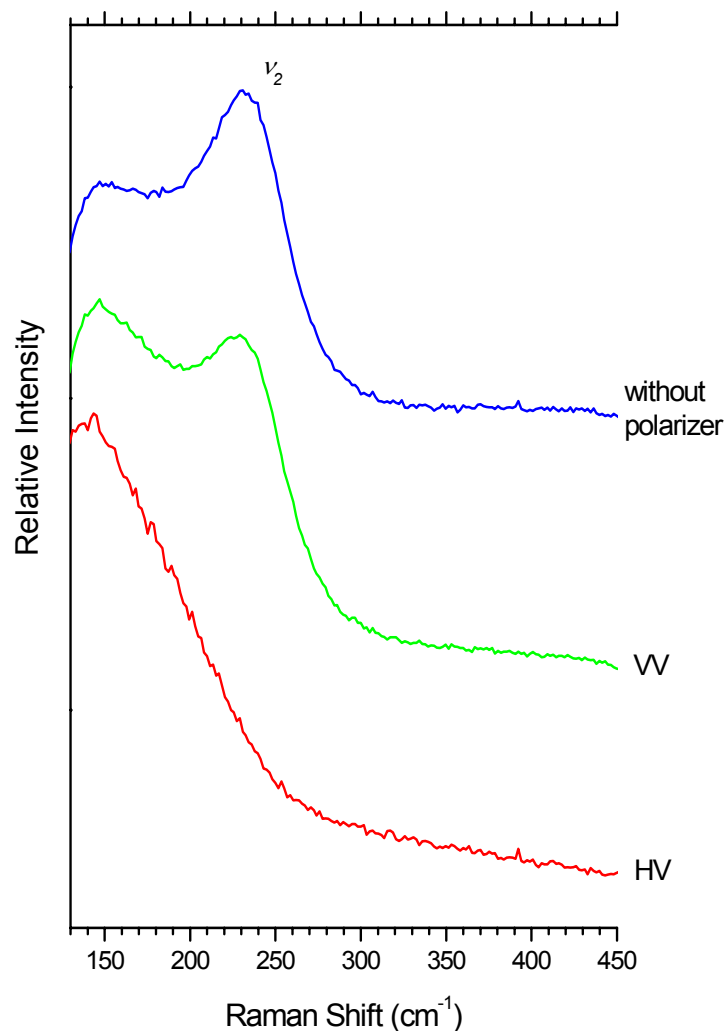
Figure 5.11: Raman spectra of liquid $(CeCl_3)_{0.25}$-$(LiCl-KCl)_{eu,\ 0.75}$ at 500°C, with and without polarizer. The spectra were recorded at the same conditions as the Fig 5.1 and with 120 s of integration time.

As for $NdCl_3$, the Raman spectra of the $(CeCl_3)_{0.25}$-$(LiCl-KCl)_{eu,\ 0.75}$ melt were recorded in the three different cells (Fig 5.12).

It is highly surprising to observe three different spectra. All the spectra show the broad octahedron vibration (ν_2): stronger in cells 1 and 3, weaker in cell 2. It is reasonable to regard the spectrum of cell 1 as the true spectrum of $CeCl_3$-$(LiCl-KCl)_{eu}$ for the given composition. The spectrum of cell 3 differs from the others by an extraordinarily strong band at about 450 cm^{-1}. Furthermore, the spectrum of the cell 2 (with the internal furnace) is extremely different from both spectra of cell 1 and cell 3. In this spectrum the band ν_2 is very weak and four new bands ν_1', ν_1, ν_3

and v_4 do appear. This resembles strongly to the spectra of $NdCl_3$-$(LiCl$-$KCl)_{eu}$ in the same cell (see Fig 5.13). Evidently, similar structures develop in the Ce-system like in the Nd-system with this cell type. In contrast to the Nd-system, the bands v_1 and v_4 are substantially stronger in the Ce-system. Here it is worth to notice that the oxidation state II for cerium chlorides is not stable in such melts (Mellors 1959). Perhaps the special design of cell 2 with the internal furnace provides the possibility of a reduction reaction where a Ce(II)-species appears, at least temporarily.
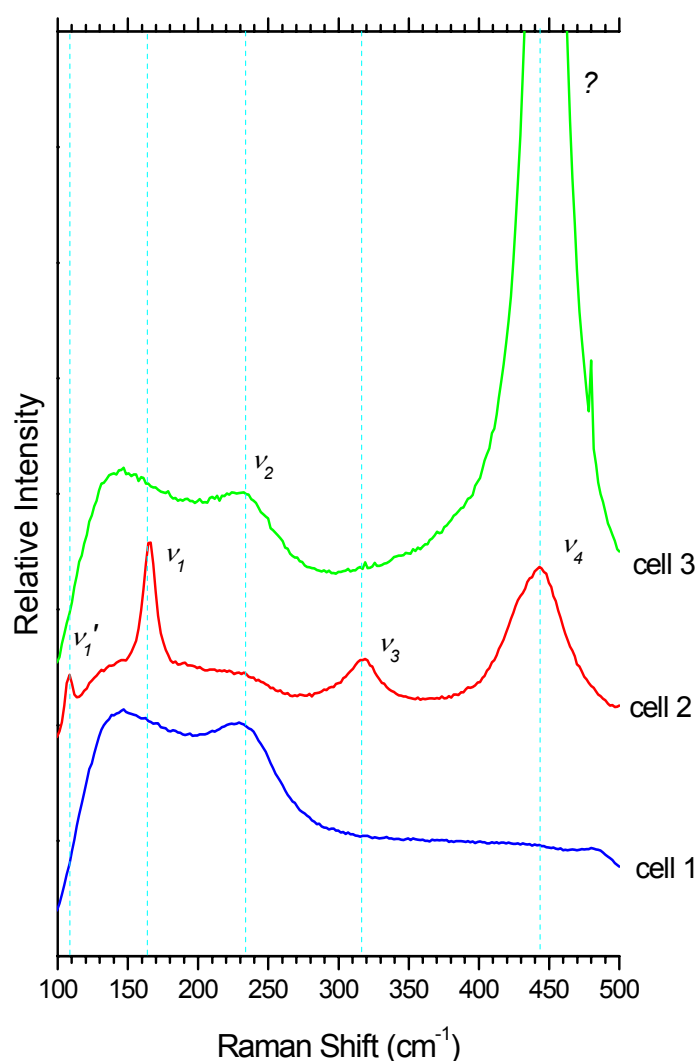
Figure 5.12: Raman spectra of liquid $CeCl_{3(x=0.25)}$-$(LiCl$-$KCl)_{eu(x=0.75)}$ in cell 1 (quartz cell), cell 2 (windowless cell with internal furnace) and cell 3 (windowless cell with external furnace). All spectra were recorded at 500°C, without polarizer and at the same conditions as Fig 5.1.
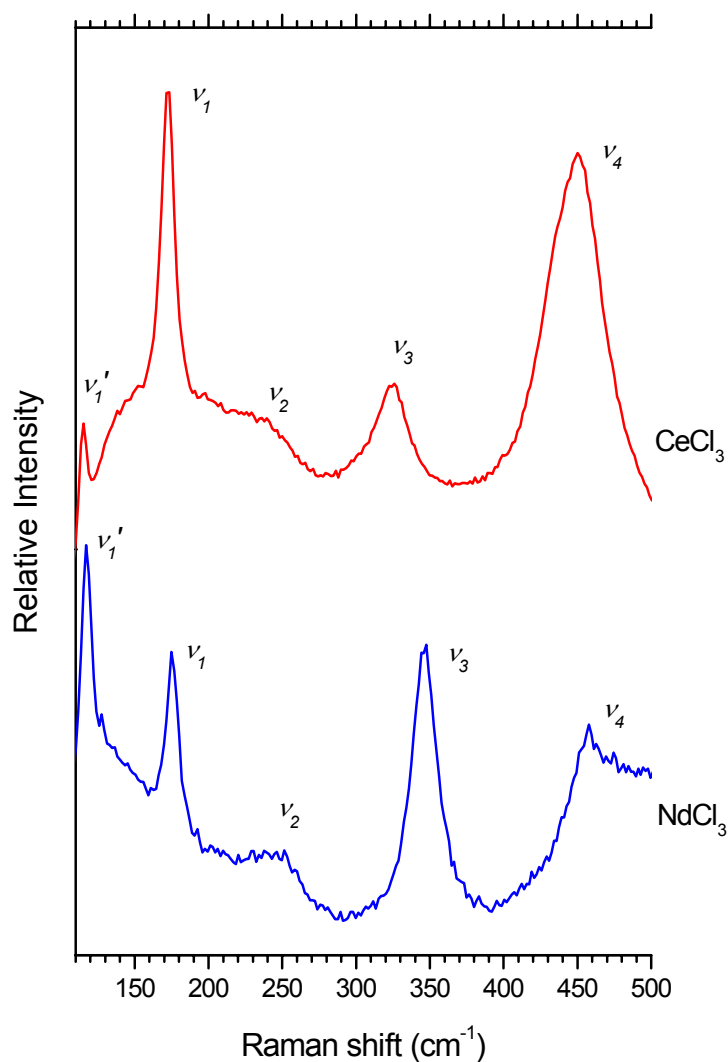
Figure 5.13: Comparison of the Raman spectrum of liquid $(NdCl_3)_{0.10}$-$(LiCl-KCl)_{eu, \, 0.90}$ at 500°C with the spectrum of liquid $CeCl_{3(x=0.25)}$-$(LiCl-KCl)_{eu(x=0.75)}$ recorded in the cell 2. The spectra were recorded without polarizer, at the same conditions as in Fig 5.1 and 120 s integration time.

5.2.2. $(Ce)_y$-$(LiCl-KCl)_{eu}$

Since we were interested in spectra of mixtures of Ce-CeCl₃ in LiCl-KCl eutectic, we also have studied the second limiting cases: the $(Ce)_y$-$(LiCl-KCl)_{eu, \, 1-y}$ melts. Because the solubility of Ce in the eutectic is low we did not expect any Raman active vibration. Nevertheless, the spectra (Fig 5.14) showed a strong band at about 450 cm^{-1}. This was essentially due to the addition of Ce, since the spectra of pure LiCl-KCl eutectic did not show any band (appendix A.2.1). A possible

explanation for this surprisingly strong band would be the existence of oxide impurities on the surface of the metal. To verify this hypothesis we also recorded Raman spectra from the metal surface, which also showed the strong band at 450 cm^{-1} (see appendix A.4.1). A comparison with the literature confirms that the band is caused by CeO_2 (Weber 1993, Wang 2001).
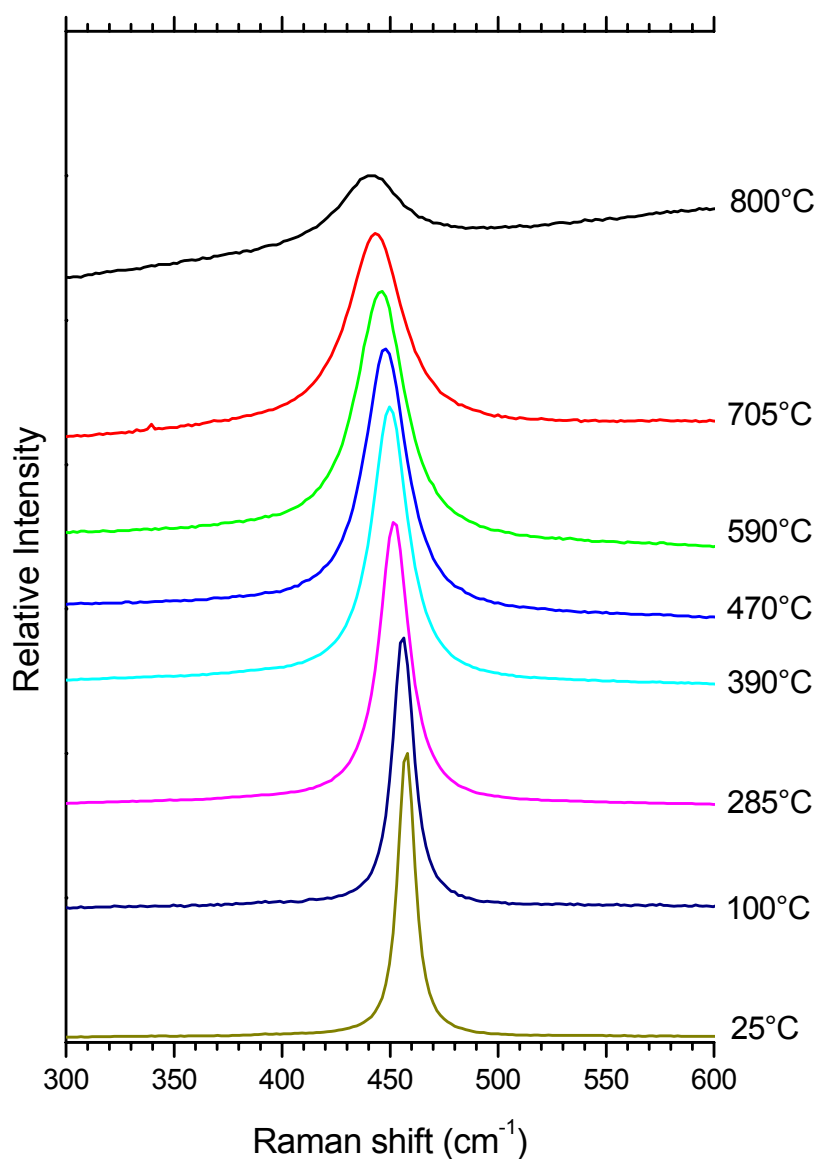
Figure 5.14: Raman spectrum of $(Ce)_{0.035}$-$(LiCl-KCl)_{eu,\ 0.965}$ at various temperatures, without polarizer and 30 s of integration time. The spectra were recorded at the same conditions as Fig 5.1.

Although Ce was always stored in the glove box, only a trace of oxygen was necessary to oxidize the Ce-metal. From these experiments it was not very clear when and how the oxide reaches

the crucible and how it is dissolved in the eutectic. In comparison to solid CeO_2, it seems to be unaltered, but if it happens to be suspended, dissolved or attached to the Ce-surface, can not be certainly determined.

5.2.3. $(CeCl_3)_x$-$(Ce)_y$-$(LiCl-KCl)_{eu}$

The Fig 5.15 shows the spectra series of $(CeCl_3)_x$-$(Ce)_y$-$(LiCl-KCl)_{eu}$ mixtures as function of the concentration. According to the phase diagram (appendix A.1.4), the maximum concentration of Ce metal that can be dissolved in liquid $CeCl_3$ above 770°C is 10 % mol. The phase diagram of Ce-$CeCl_3$-$(LiCl-KCl)_{eu}$ is not known but it is reasonable to expect that the solubility of Ce in $(CeCl_3)_x$-$(LiCl-KCl)_{1-x}$ is smaller than in pure $CeCl_3$. For this reason, an analysis as function of the composition can give only a qualitative insight. In addition, it is necessary to notice here the difficulty to work with small amounts of Ce metal, due to its hardness. The amount of sample necessary for each experiment was approximately 0.05 g; in consequence, for the mixture with a higher concentration of Ce metal (y=0.02), only 0.0015 g of Ce metal were needed.

The spectra in Fig 5.15 are characterized by the octahedron band at about 240 cm^{-1}, and with increasing Ce concentration, by a growing oxide band at ∼ 450 cm^{-1}. In these spectra there is no indication for the Ce-species found in cell 2 (Figs 5.12 and 5.13).

In this respect, the spectra of $(CeCl_3)_{0.25}$-$(Ce)_{0.005}$-$(LiCl-KCl)_{eu, 0.745}$ shown in Fig 5.16 are of special interest, where we recorded them immediately after melting and after one hour. The first spectrum showed all bands v_1', v_1, v_2, v_3 and v_4 like those of Fig 5.13. After one hour, v_1 and v_4 are visible, but v_1 and v_3 are strongly reduced. Then, under the special conditions of this experiment, the bands v_1', v_1, v_2, v_3 and v_4 could be observed as an intermediate state.
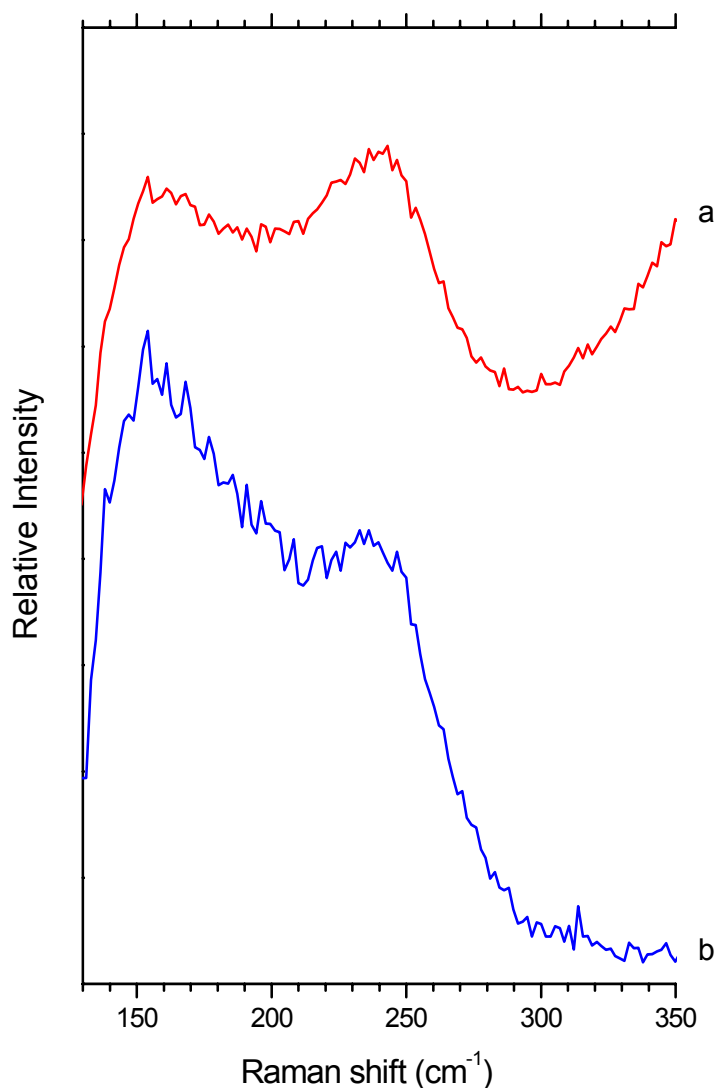
Figure 5.15: Raman spectra of $(CeCl_3)_x$-$(Ce)_y$-$(LiCl\text{-}KCl)_{eu,\ 1\text{-}x\text{-}y}$ melts in the cell 3. The samples were heated up to 600°C, recorded the spectra without polarizer after about 6 hours, with 120 s of integration time, and at the same conditions as Fig 5.1.

　　　a) $(CeCl_3)_{0.20}$-$(Ce)_{0.005}$-$(LiCl\text{-}KCl)_{eu,\ 0.795}$
　　　b) $(CeCl_3)_{0.20}$-$(Ce)_{0.02}$-$(LiCl\text{-}KCl)_{eu,\ 0.78}$

The interesting, and in some manner surprising, result of Fig 5.16 let us study the dissolution process of Ce and $CeCl_3$ in LiCl-KCl eutectic in more detail. We recorded spectra at various temperatures and as function of time for mixtures with low and high concentrations of Ce metal. The spectra at various temperatures of the mixtures $(CeCl_3)_{0.25}$-$(LiCl\text{-}KCl)_{eu,\ 0.75}$, $(CeCl_3)_{0.20}$-$(Ce)_{0.005}$-$(LiCl\text{-}KCl)_{eu,\ 0.795}$, and $(CeCl_3)_{0.20}$-$(Ce)_{0.02}$-$(LiCl\text{-}KCl)_{eu,\ 0.78}$, were very similar. Fig 5.17

shows for example the spectrum of $(CeCl_3)_{0.20}$-$(Ce)_{0.005}$-$(LiCl$-$KCl)_{eu, 0.795}$ (other spectra can be found in the appendices A.4.3 and A.4.5).
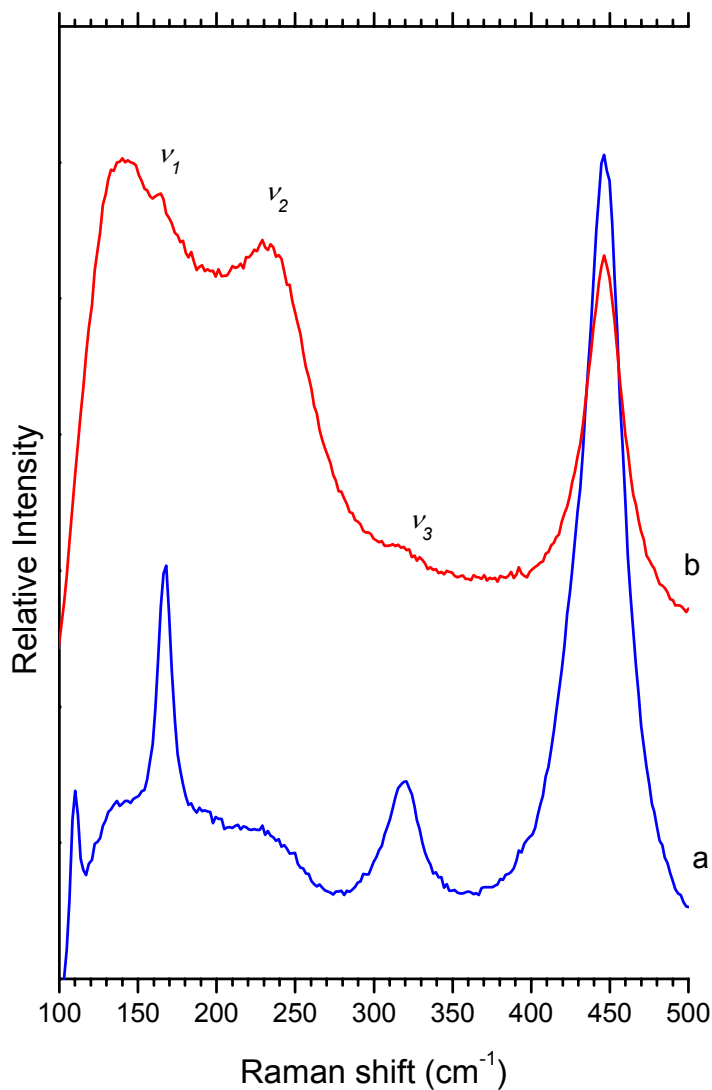
Figure 5.16: Raman spectra of $(CeCl_3)_{0.25}$-$(Ce)_{0.005}$-$(LiCl$-$KCl)_{eu, 0.745}$ melt in the cell 3. The spectra were recorded at 585°C without polarizer, 120 s of integration time and at the same conditions as Fig 5.1.
    a) First spectrum.
    b) One hour later.

In the Fig 5.17 is possible to observe a change in the appearance of the spectra at 450 °C; at this temperature the mixture melts and the dissolution process of the metal in the chloride begins. For this reason, we recorded the spectra as function of the time at this temperature.
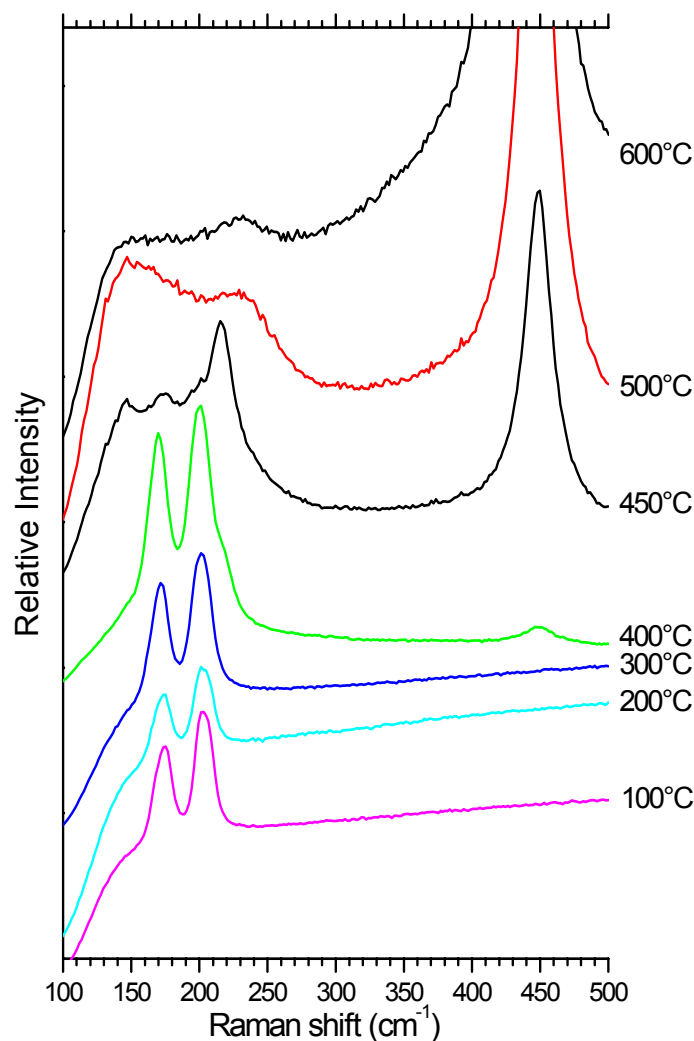
Figure 5.17: Raman spectra of $(CeCl_3)_{0.20}$-$(Ce)_{0.005}$-$(LiCl-KCl)_{eu, 0.795}$ at various temperatures in the cell 3. The spectra were recorded without polarizer, 120 s of integration time and at the same conditions as Fig 5.1.

Fig 5.18 shows spectra of the $(CeCl_3)_{0.20}$-$(Ce)_{0.005}$-$(LiCl-KCl)_{eu, 0.795}$ at 450°C as function of the time. For this sample, the dissolution process lasted 300 s. With the exception of the strong v_4-band, the dissolution process looks very similar to that of pure $CeCl_3$ (appendix A.4.4). Fig 5.19 shows the dissolution process of $(CeCl_3)_{0.20}$-$(Ce)_{0.02}$-$(LiCl-KCl)_{eu, 0.78}$ at 500°C. Contrary to the spectra from the left side, the v_1, v_3 and v_4 bands are clearly visible, indicating again the intermediate presence of a possible Ce (II) species.

Observing in detail: as function of time, the v_2 band due to the $CeCl_6^{3-}$ species became weaker and the band v_4 became broader. At t = 1800 s, the CeO_2 band (at ~450 cm⁻¹) merged in the high energy shoulder of the v_4-band and became stronger with the time. From t = 2520 s, the bands

ν_1, ν_3 and ν_4 became weaker, until they disappeared, whereas the bands ν_2 and ν_{CeO_2} became stronger and remained in the spectra. In this case the dissolution process lasted approximately 3600 s.
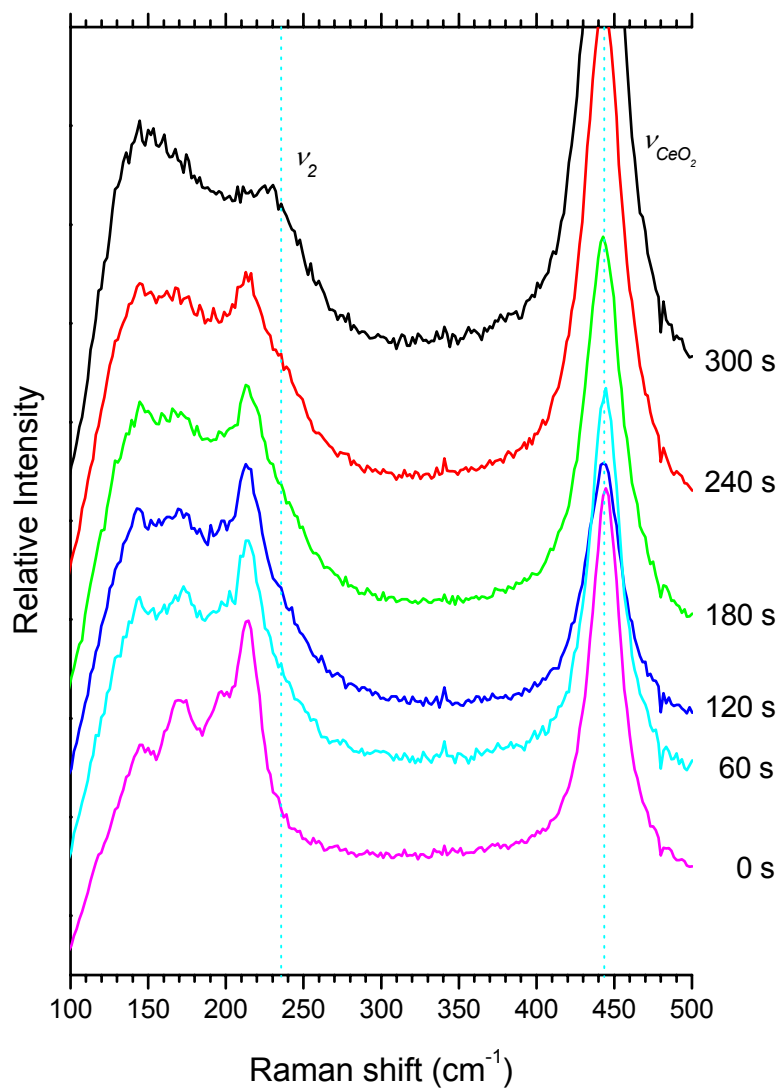
Figure 5.18: Raman spectra of $(CeCl_3)_{0.20}$-$(Ce)_{0.005}$-$(LiCl\text{-}KCl)_{eu,\ 0.795}$ mixture at 450°C and as function of the time in the cell 3. The spectra were recorded without polarizer and at the same conditions as Fig 5.1.
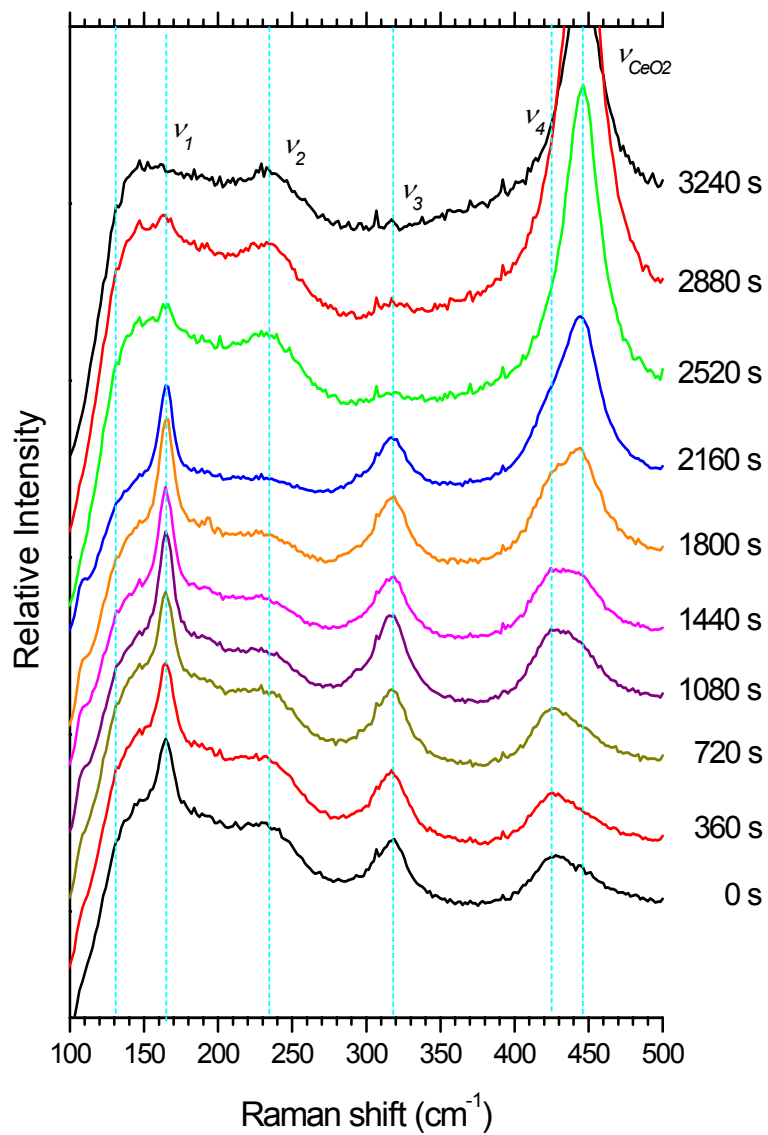
Figure 5.19: Raman spectra of $(CeCl_3)_{0.20}$-$(Ce)_{0.02}$-$(LiCl\text{-}KCl)_{eu,\ 0.78}$ mixture at 500°c and as function of the time in the cell 3. The spectra were recorded without polarizer and at the same conditions as Fig 5.1.

6: Raman Spectra of Ln-LnI$_3$ (Ln = Nd, Ce)

In this chapter we show representative spectra of the rare earth metal-rare earth iodide systems Ln-LnI$_3$ (Ln=Nd, Ce).

For the excitation of the samples, a He-Ne-laser (λ_0=632.8 nm) and an Ar-laser (λ_0=514.5 nm) were used. If not otherwise stated the recording conditions were as follows: the notch filter angle for the He-Ne laser was 4.05° and for the Ar laser 6.59°. The confocal hole aperture was 200 μm, the gratin 1200 g/mm and the slit aperture was 100 μm. The laser beam was focused with the macro objective of the microscope using an achromatic lens with 40 mm focal length. The spectra were recorded for different concentrations of Ln-LnI$_3$ at various temperatures and for some samples as function of the time. As will be explained below all spectra were recorded in cell 1.

6.1 Ce-CeI$_3$ Melts

6.1.1. CeI$_3$

In this section the Raman spectra of the CeI$_3$ melts are presented. They have been recorded in cell 1 since LnI$_3$ did not corrode quartz in the temperature range of interest. Fig 6.1 shows spectra of CeI$_3$ at various temperatures. At first glance it was very surprising to see

a series of nearly equidistant bands developing at a temperature of 50°C. These bands became stronger and broader with increasing temperature.
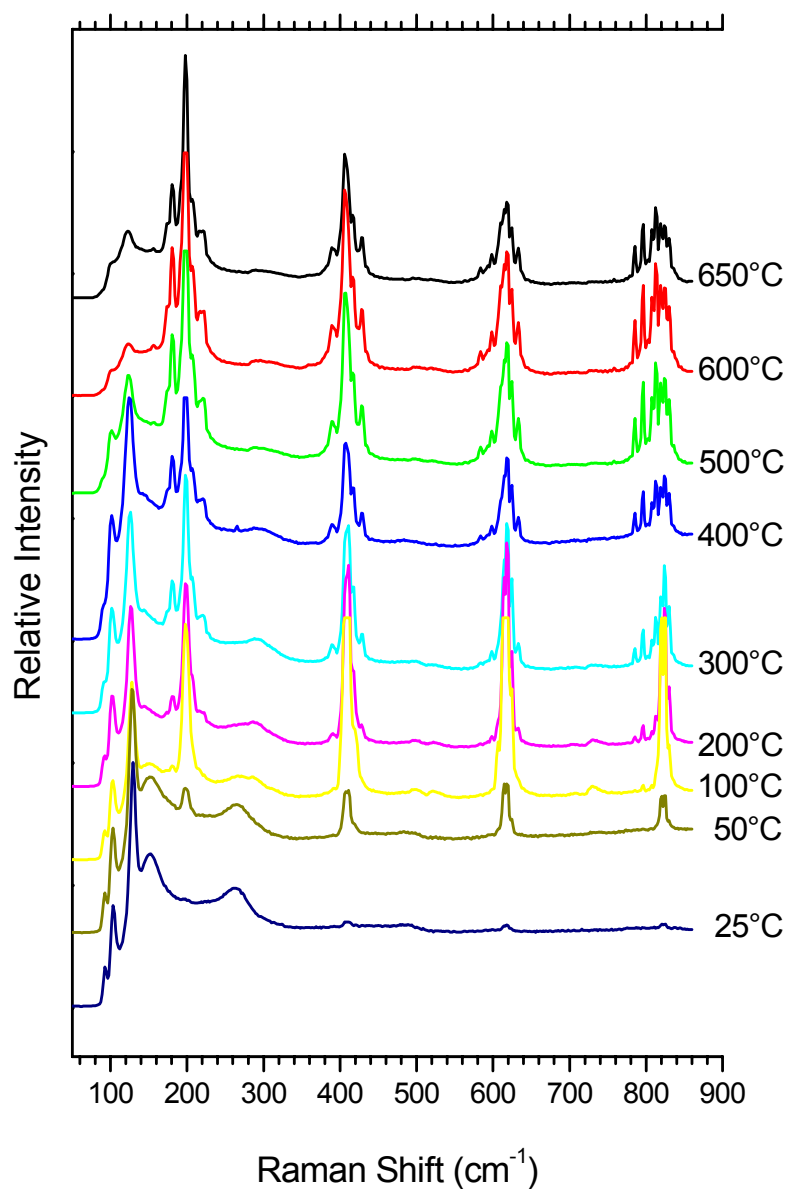

Figure 6.1: Raman spectra of solid CeI$_3$ at various temperatures obtained in the quartz cell (cell 1). The quartz tube with the sample was evacuated before sealing. The spectra were recorded without polarizer, 30 s of recording time, λ_0=632.8 nm and a notch filter angle of 6.59°.

In this experiment, the formation of a dark red gas was observed, which is due to the formation of I$_2$ gas by the following reaction:

$CeI_3 \rightarrow CeI_2 + \frac{1}{2} I_2$

As shown in Fig 6.2, the iodine can be clearly identified by its typical fluorescence patterns (Muenter 1996). I_2 fluorescence is an example of a strong disturbance not only for the Stokes Raman spectrum but also for the anti-Stokes spectrum. This is due to the fact that the He-Ne laser can exact the following transitions: $v''= 3$, $j''= 33$ of the electronic ground state to $v'= 6$, $j'= 32$ of the electronic excited state and $v'' = 5$, $j''=127$ to $v'= 11$, $j'= 128$. According to the Franck-Cordon principle, the $v'' < 3$ and $v'' < 5$ have a finite, non-zero probability. This leads to fluorescence lines in the anti-Stokes spectrum.
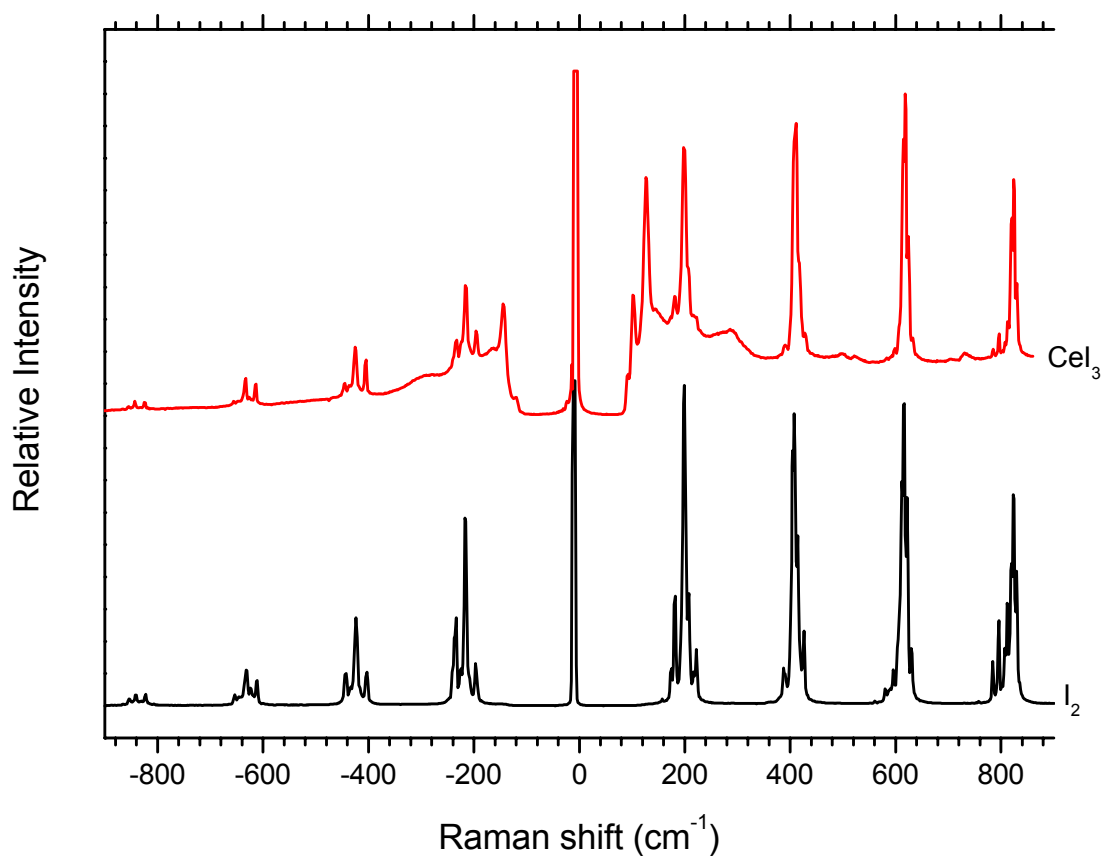
Figure 6.2: Comparison of the Raman spectra of CeI_3 solid and induced fluorescence spectrum of I_2 gas, both at 200°C. The spectra were recorded in the cell 1, without polarizer, 30 s of integration time and at the same conditions as Fig 6.1. Note the occurrence of fluorescence lines in the anti-Stokes spectrum.

As can be seen in Fig 6.1 we observed Raman bands from the solid CeI$_3$ (~110, ~150 and ~260 cm^{-1}) besides the I$_2$ fluorescence. These spectral components became weaker with increasing temperature due to the blackbody background emission and due to the absorption of the exciting beam by the I$_2$ vapor. To reduce the fluorescence and the blackbody (see Fig 4.2) problems the Argon line at 514.5 nm was employed for the Raman measurements.

Spectra of CeI$_3$ in the solid state (25°C-700°C) and in the liquid state are shown in Figs 6.3 (solid) and 6.4 (liquid).
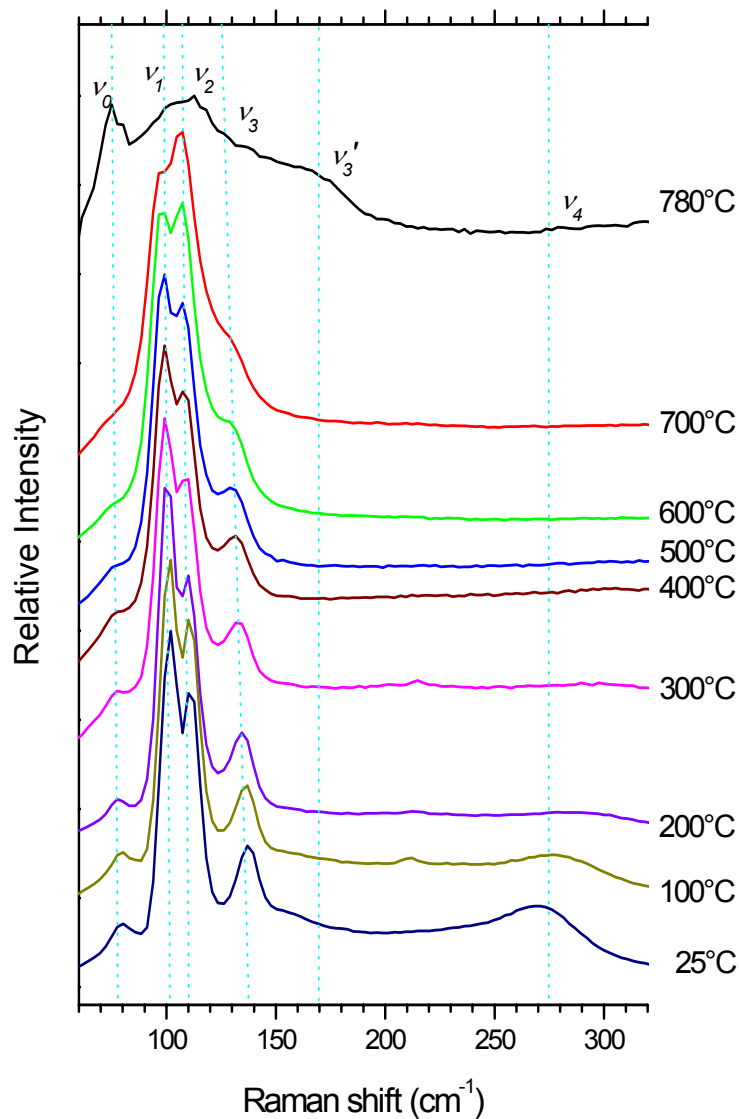
Figure 6.3: Raman spectra of CeI$_3$ at various temperatures in the quartz cell (cell 1). The spectra were recorded with the Ar laser (λ_0=514.5nm), a 4.05° notch filter angle, an integration time of 300 s and without polarizer.
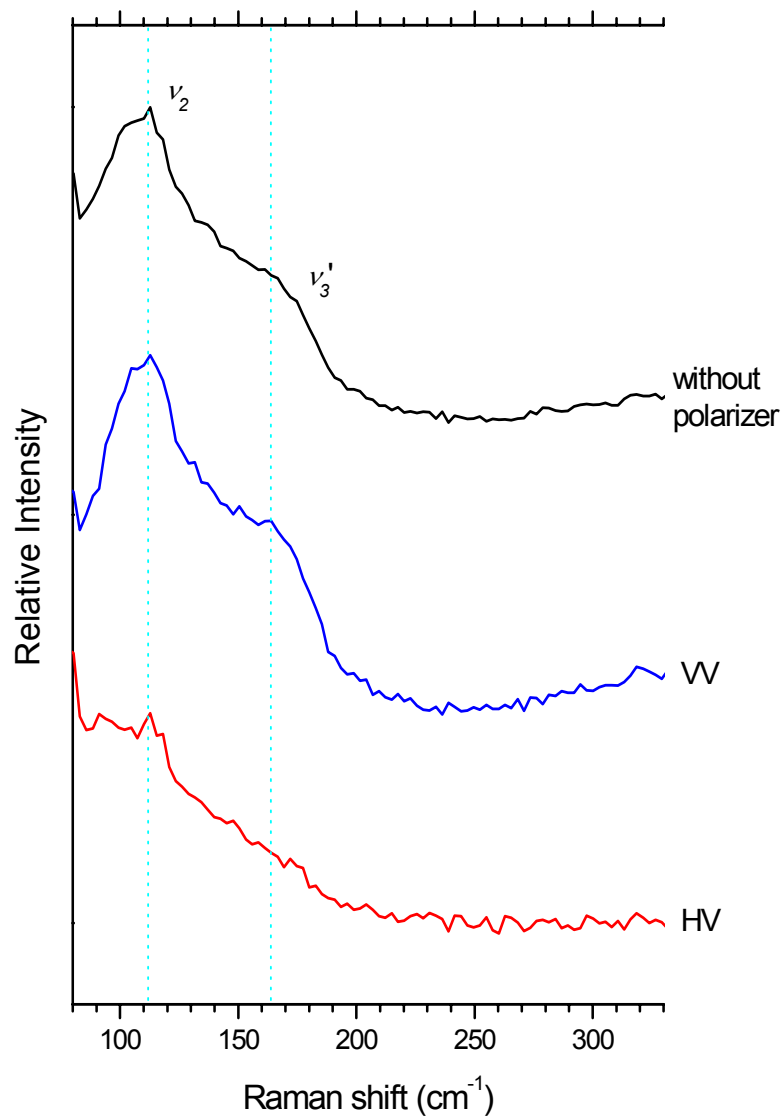
Figure 6.4: Raman spectra of CeI_3 liquid at 780°C, with and without polarizer. The spectra were recorded at the same conditions as Fig 6.3. HV-spectrum: the electrical vector of the incident light is perpendicular to the electrical vector of the excited light. VV-spectrum: the electrical vector of the incident light is parallel to the electrical vector of the excited light.

It is interesting to see that neither the blackbody radiation nor the I_2-fluorescence is visible even though the formation of a dark red film was observed in the cell. This film makes

only difficult the focusing of the beam onto the sample and, in consequence, leads to a lower intensity of the obtained spectra. In the solid state at 25°C five Raman bands are discernible. They are labeled as ν_0, ν_1, ν_2, ν_3 and ν_4. ν_0 is very close to the cut off of the Ar-notch filter and a discussion of its intensity is therefore questionable. ν_4 at about 270 cm^{-1} disappears with increasing temperature and can not be seen at 200°C. A similar trend is observed in Fig 6.1. With increasing temperature ν_1 and ν_3 become continuously weaker whereas ν_2 becomes stronger.

On melting, ν_1 and ν_3 disappear and a new band, ν_3', appears at ~162 cm^{-1}. The liquid spectra consist at least of two polarized bands (Fig 6.4). A depolarized band is weakly visible around 110 cm^{-1}. Until now, no Raman spectra of liquid CeI$_3$ are reported. We note furthermore that the appearance of the spectrum is similar to that of liquid NdCl$_3$.

6.1.2. CeI$_2$

The spectra of CeI$_2$ were recorded in the quartz cell (cell 1). The spectra are shown in Fig 6.5 at various temperatures. In the spectrum at 25°C three bands are distinguishable: ν_1 (~100 cm^{-1}), ν_2 (~110 cm^{-1}) and ν_3 (~135 cm^{-1}). The solid CeI$_2$ spectra are very similar in comparison to the solid CeI$_3$ spectra. This is also true for the behavior with increasing temperature. The ν_1 and ν_3 bands become weaker with increasing temperature and the ν_2 band becomes stronger. A new band ν_3' (~167 cm^{-1}) appears at 500°C. This band is not visible in the solid CeI$_3$ spectra (Fig 6.3). For temperatures above 600°C it was not possible to obtain an analyzable spectrum because CeI$_2$ is extremely corrosive and dark. We tried to record the spectra in the windowless cell 3 but a dark and thick film of sublimated salt was deposited on the optical window, impeding the observation of a spectrum.
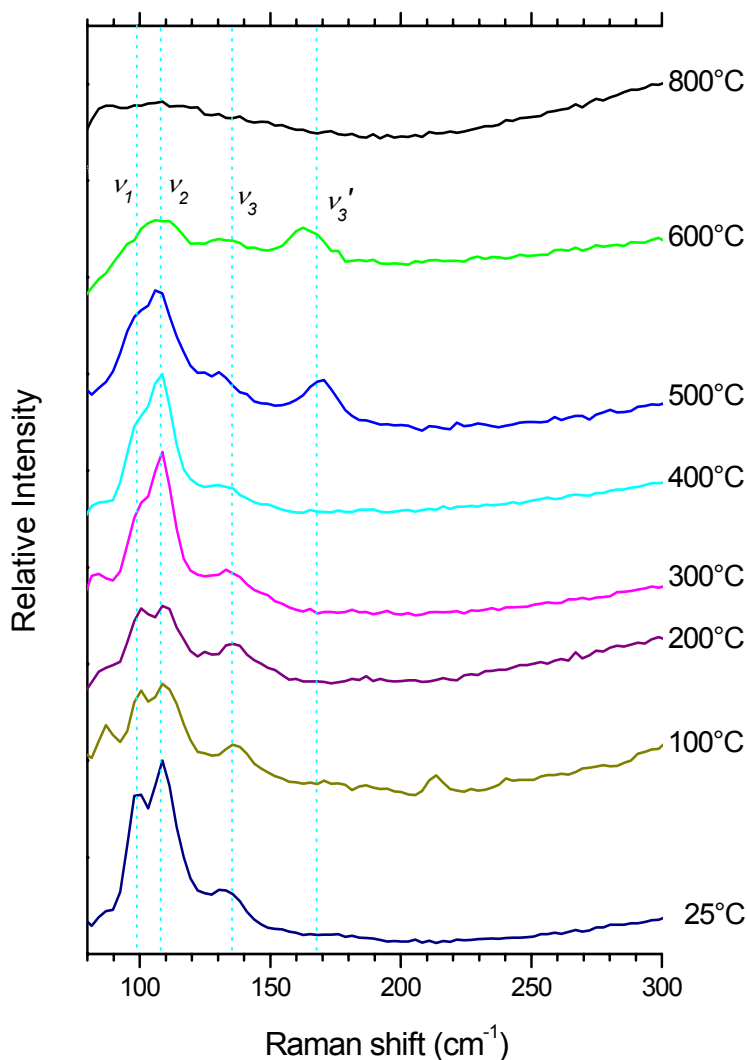
Figure 6.5: Raman spectra of CeI$_2$ at various temperatures in the quartz cell (cell 1). The spectra were recorded without polarizer, an integration time of 300 s and at the same conditions as Fig 6.3.

6.1.3. (CeI$_3$)$_x$-(CeI$_2$)$_{1-x}$

The Raman spectra of the liquid (CeI$_3$)$_x$-(CeI$_2$)$_{1-x}$ are shown in the Figure 6.6. Due to the sublimation problem it was only possible to try to record the spectra in cell 1. The laser wavelength was 514.5 nm (19436 cm^{-1}). The spectrum of liquid CeI$_3$ which was already presented in Fig 6.4 shows two bands: ν_2 at ~110 cm^{-1} and ν_3' at ~170 cm^{-1}. On addition of a small amount of CeI$_2$ ($x_{CeI_2} = 0.06$) these two bands are still visible but the quality of the

spectra decreased strongly. This must be due to the onset of the quartz corrosion by CeI_2. As a consequence, the laser beam can not be focused with the same quality, the scattering volume becomes diffuse and the spectrum is more and more influenced by the blackbody radiation. At higher CeI_2 concentration it was not possible to get interpretable spectra of the liquid. The series of the CeI_3-CeI_2 spectra on heating from room temperatures to the temperatures indicated in Fig 6.6 are shown in the appendices A.5.2 to A.5.4.
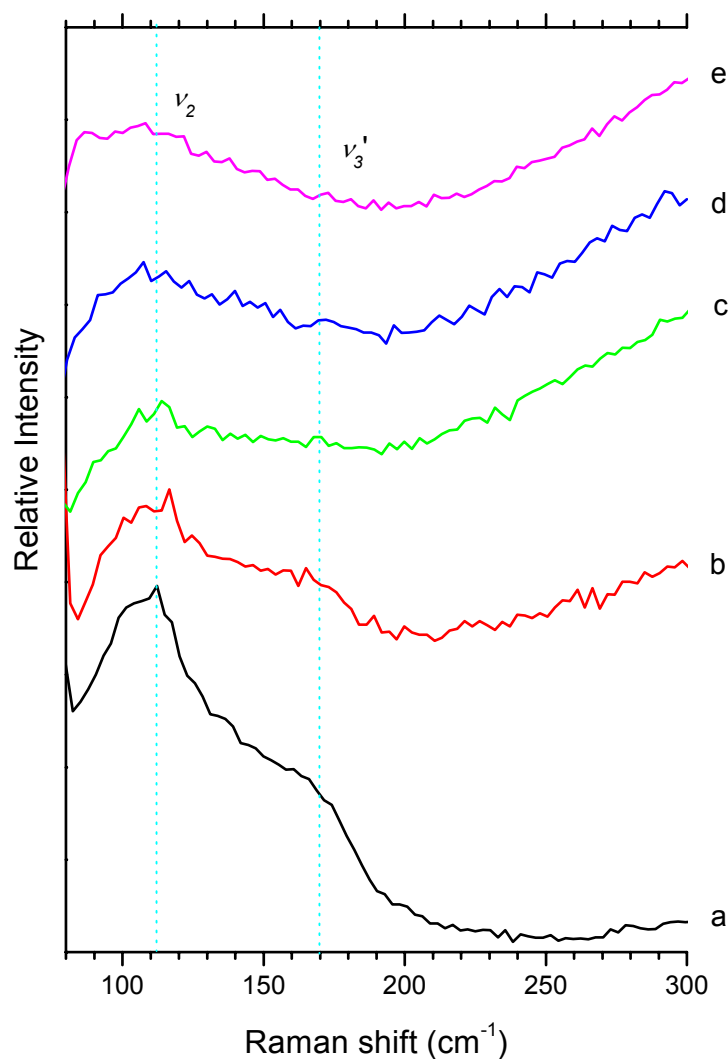
Figure 6.6: Raman spectra of $(CeI_3)_x$-$(CeI_2)_y$ melt with the cell 1. The spectra were recorded without polarizer, 300 s of integration time and at the same conditions as Fig 6.3.
  a) CeI_3 at 780°C.
 b) $(CeI_3)_{94}$-$(CeI_2)_{06}$ at 750°C.
  c) $(CeI_3)_{76}$-$(CeI_2)_{24}$ at 720°C (eutectic mixture, see phase diagram in appendix A.1.4).
  d) $(CeI_3)_{50}$-$(CeI_2)_{50}$ at 730°C
  e) CeI_2 at 810°C

6.1.4. (CeI₃)ₓ-(LiI-KI)ₑᵤ, ₁₋ₓ

As it was shown in the previous sections of this chapter, it was hardly possible to record Raman spectra of the liquid CeI_3-CeI_2 mixtures. As for the chlorides, we present in the following Raman spectra the CeI_3-CeI_2 dissolved in eutectic LiI-KI (melting point 260°C, Janz 1967). Unfortunately, the solubility of CeI_3 or CeI_2, is not reported in the literature. Thus, the exact composition of the liquid phase may be unknown when solid CeI_3 or CeI_2 coexists as precipitate with the liquid phase. For the interpretation of the spectra this has to be kept in mind.
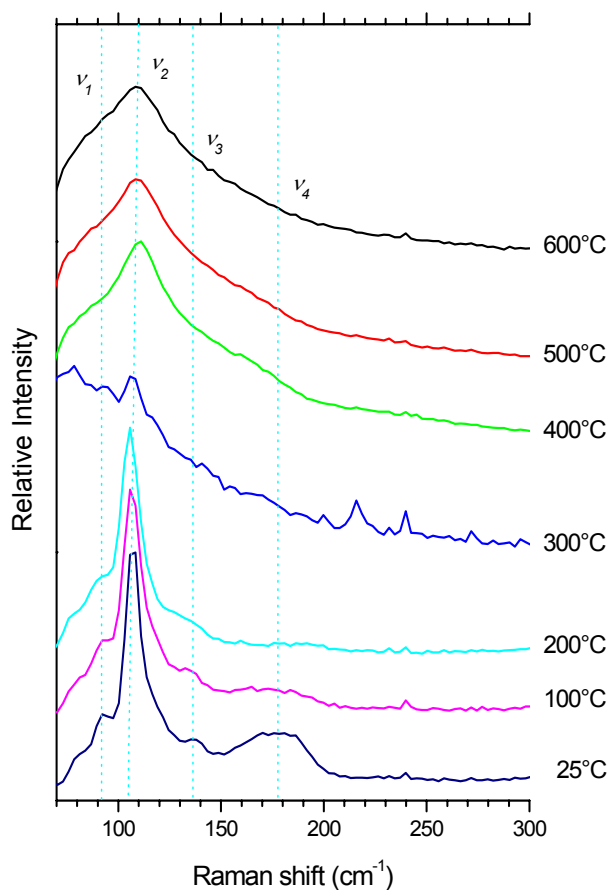
Figure 6.7: Raman spectra of $(CeI_3)_{0.05}$-$(LiI-KI)_{eu, 0.95}$ at various temperatures in the quartz cell (cell 1). The spectra were recorded without polarizer, 300 s of integration time and at the same conditions as Fig 6.3.
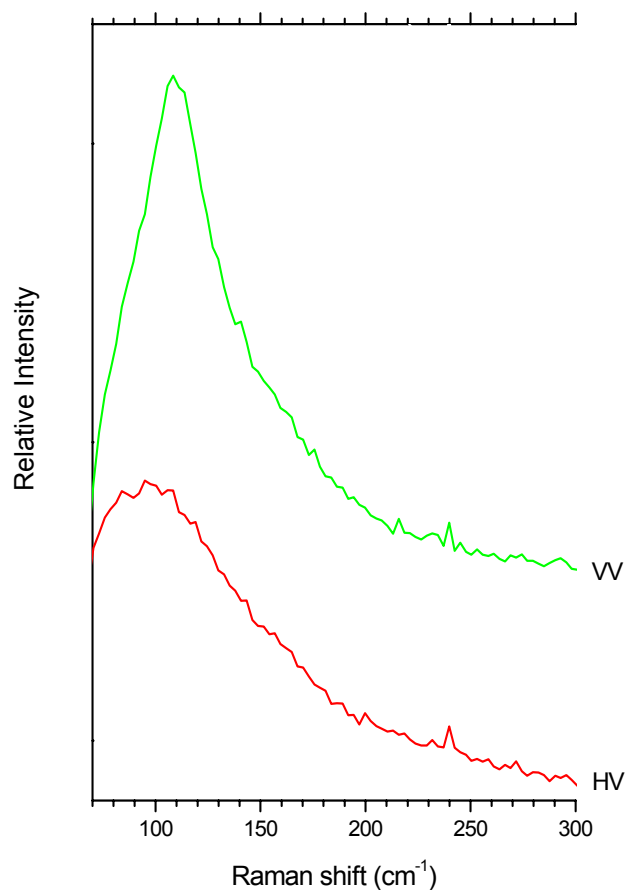
Figure 6.8: Raman spectra of liquid $(CeI_3)_{0.05}$-$(LiI-KI)_{eu, 0.95}$ at 600°C in the quartz cell (cell 1). The spectra were recorded with 300 s of integration time and at the same conditions as Fig 6.3.

Fig 6.7 shows the Raman spectra of $(CeI_3)_{0.05}$-$(LiI-KI)_{eu,\ 0.95}$ with increasing temperature after they have been grinded and intensively mixed. At 25°C the ν_2 and ν_3 bands of Fig 6.3 are clearly visible despite of the dilution of CeI_3. Differently to Fig 6.3 is the weak ν_1 band and the occurrence of a broad band in the 170 to 190 cm^{-1} range. The latter disappears on heating. The weak ν_1 band may be due to accidental different orientation of the crystallites to respect to the laser. On melting of the eutectic LiI-KI all CeI_3 bands disappear, but with increasing temperature a broad polarized band centered at ~110 cm^{-1} is recovered. This band is presumably due to CeI_6^{3-} species. The bad resolution of the spectra at 300°C is due to the misalignment of the Raman excitation volume on melting.

6.1.5 $(CeI_2)_y$-$(LiI-KI)_{eu,\ 1-y}$

For the measurements with the $(CeI_2)_y$-$(LiI-KI)_{eu,\ 1-y}$ melts we used mixtures with very low concentration of CeI_2 (y < 0.025) to diminish the corrosion of the cell. After measurements of various mixtures with different concentrations of CeI_2 we found fairly good spectra at y = 0.02.

The spectra of a $(CeI_2)_{0.02}$-$(LiI-KI)_{eu,\ 0.98}$ mixture, are shown in Fig 6.9 at various temperatures. Surprisingly, the spectra at temperatures below 200°C look very similar to those of $(CeI_3)_{0.05}$-$(LiI-KI)_{eu,\ 0.95}$ (Fig 6.7) and the behavior with increasing temperature is also similar. But in contrast to CeI_3 the CeI_2 mixture exhibits a strong ν_1 band at 300°C. ν_1 is now even stronger than ν_2. This drastic change is probably due to the phase change from solid to liquid. At temperatures up to 500°C the band ν_1 becomes broader and overlaps the band ν_2. The liquid spectra at 600°C (HV and VV, Fig 6.10) show a strong polarized band ν_2 and one depolarized ν_1.
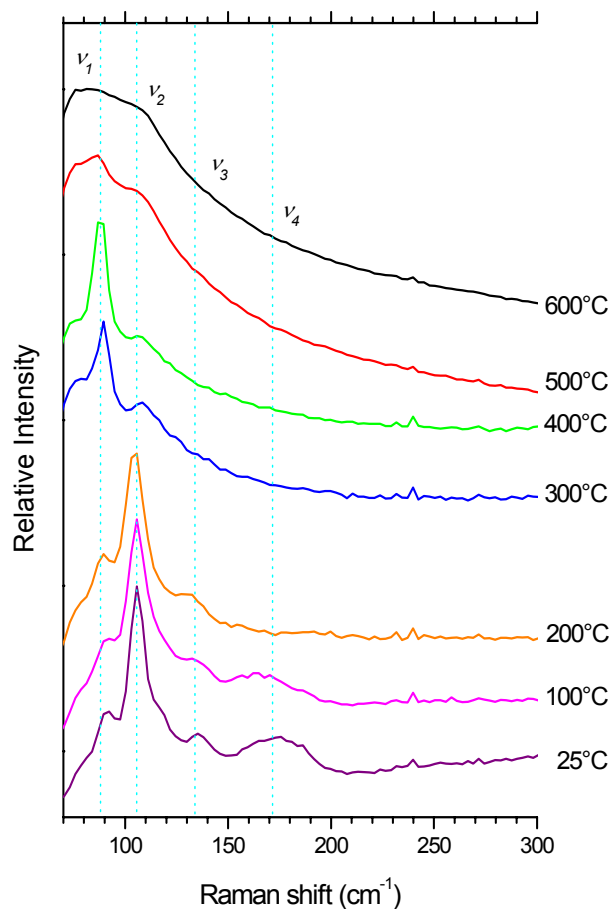
Figure 6.9: Raman spectra of $(CeI_2)_{0.02}$-$(LiI-KI)_{eu, 0.98}$ at various temperatures in the quartz cell (cell 1). The spectra were recorded without polarizer, 300 s of integration time and at the same conditions as Fig 6.3.
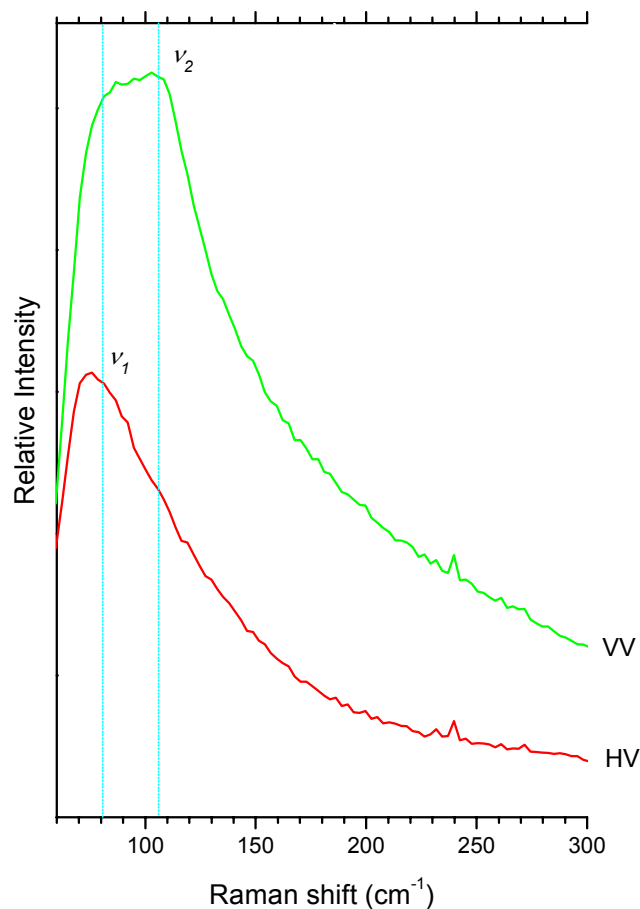
Figure 6.10: Raman spectra of liquid $(CeI_2)_{0.02}$-$(LiI-KI)_{eu, 0.98}$ at 600°C in the quartz cell (cell 1). The spectra were recorded with 300 s of integration time and at the same conditions as Fig 6.3.

6.1.6. $(CeI_3)_x$-$(CeI_2)_y$-$(LiI-KI)_{eu, 1-x-y}$

Spectra of $(CeI_3)_x$-$(CeI_2)_y$-$(LiI-KI)_{eu, 1-x-y}$ at a constant temperature of 500°C are showed in Fig 6.11. They have been recorded without polarizer. The spectra at various temperatures as well as the HV- and VV-spectra in the liquid state for each mixture are presented in the appendices A.6.5 to A.6.8.

The spectrum CeI_3 (spectrum *a*) was previously presented. With the addition of a low concentration of CeI_2 (y = 0.006) to CeI_3 (x = 0.094) the new band ν_1 appears (~75 cm^{-1}). The intensity of the band ν_1 is smaller than the intensity of the band ν_2, but increases with increasing

CeI_2 concentration, and for a concentration $CeI_3:CeI_2=1:1$ the intensity of both bands becomes similar (spectrum *d*).

According with the HV and VV spectra of the molten mixtures (appendix A.5.5), the band ν_1 is depolarized and the ν_2 is polarized. Finally, the spectrum *e* corresponds to the molten CeI_2 in which the ν_1 band becomes broader and the two bands (ν_1 and ν_2) are overlapped.
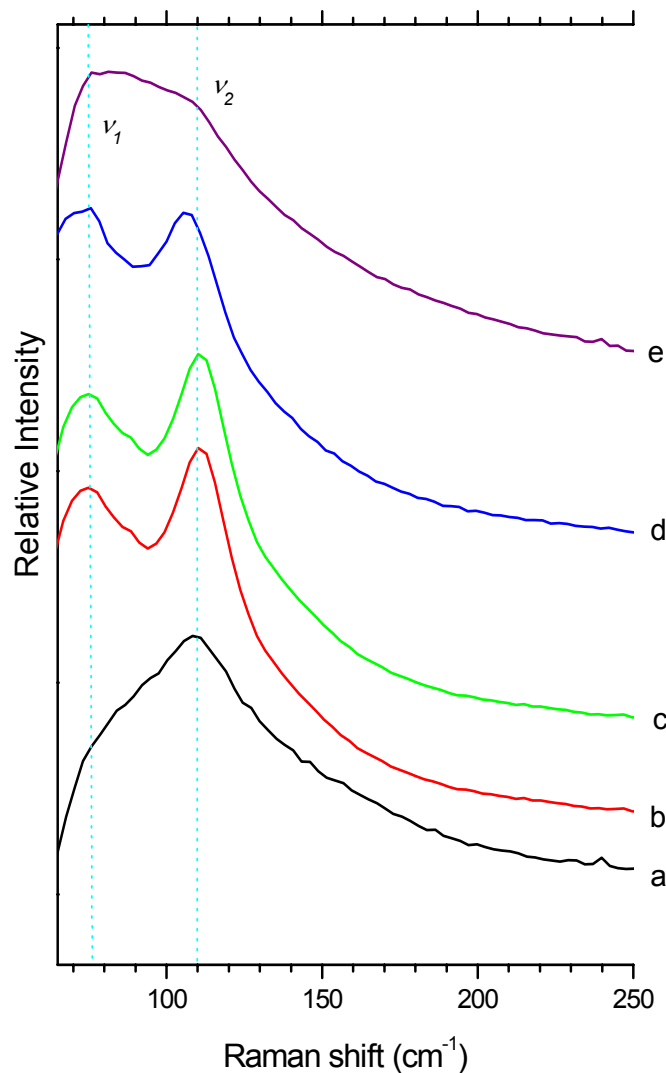

Figure 6.11: Raman spectra of $(CeI_3)_x$-$(CeI_2)_y$-$(LiI-KI)_{eu,\ 1-x-y}$ melts in the cell 1. The spectra were recorded without polarizer, at 500°C, 100 s of integration time and at the same conditions as Fig 6.3.

        a) $(CeI_3)_{0.05}$-$(LiI-KI)_{eu,\ 0.95}$.
        b) $(CeI_3)_{0.094}$-$(CeI_2)_{0.006}$-$(LiI-KI)_{eu,\ 0.90}$.
        c) $(CeI_3)_{0.076}$-$(CeI_2)_{0.024}$-$(LiI-KI)_{eu,\ 0.90}$.
        d) $(CeI_3)_{0.05}$-$(CeI_2)_{0.05}$-$(LiI-KI)_{eu,\ 0.90}$.
        e) $(CeI_2)_{0.02}$-$(LiI-KI)_{eu,\ 0.98}$.

6.2. Nd–NdI$_3$ Melts

The last class of systems studied in the present work is NdI_3-NdI_2 and its solution in eutectic LiI-KI. No Raman spectra have been found in the literature so far. The organization of this section is similar to that for Ce-CeI$_3$ in section 6.1. For all spectra the Ar-ion laser was used (λ_0=514.5 nm).

6.2.1. NdI$_3$

Fig 6.12 shows Raman spectra of NdI$_3$ at various temperatures. In the solid state spectra (25°C-500°C) one observes three bands: ν_1 (~102 cm^{-1}), ν_2 (~115 cm^{-1}) and ν_3 (~136 cm^{-1}). At 25°C the intensities of the bands ν_1 and ν_2 are almost the same. With increasing temperature ν_1 becomes smaller, ν_2 stronger, and ν_3 broader.

According to the phase diagram (see appendix A.1.5), NdI$_3$ exhibits a solid-solid phase transition at 574°C. This is clearly seen in the Raman spectra at 600°C: ν_2 is now the dominant band, ν_1 disappears, a new band develops at ~88 cm^{-1} and ν_3 shifts a little bit to higher wave numbers and is now well separated from ν_2. The liquid state spectra are characterized by two polarized bands at ~110 cm^{-1} and ~175 cm^{-1}.

6.2.2. NdI$_2$

In contrast to other rare earth iodides it was not possible to obtain an analyzable Raman spectrum of NdI$_2$. A sample of solid NdI$_2$ was heated slowly from room temperature to 800°C in increments of 50 K. We found an increase of the background radiation and the development of a strong band at about 500 cm^{-1}, which has to be assigned to corroded quartz. It was noted that the corrodibility of NdI$_2$ was higher than of CeI$_2$.
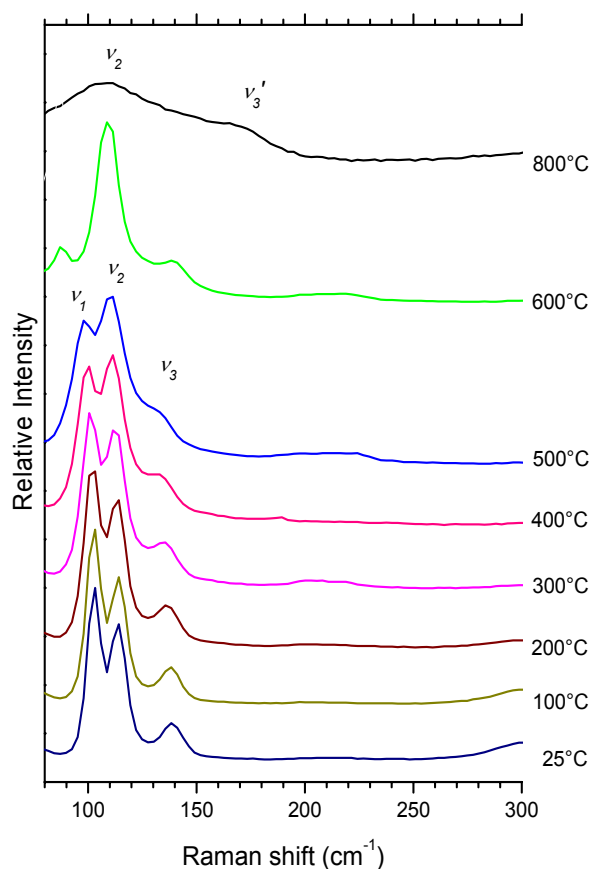
Figure6.12: Raman spectra of NdI$_3$ at various temperatures in the quartz cell (cell 1). The spectra were recorded without polarizer, a integration time of 400 s and at the same conditions as Fig 6.3.
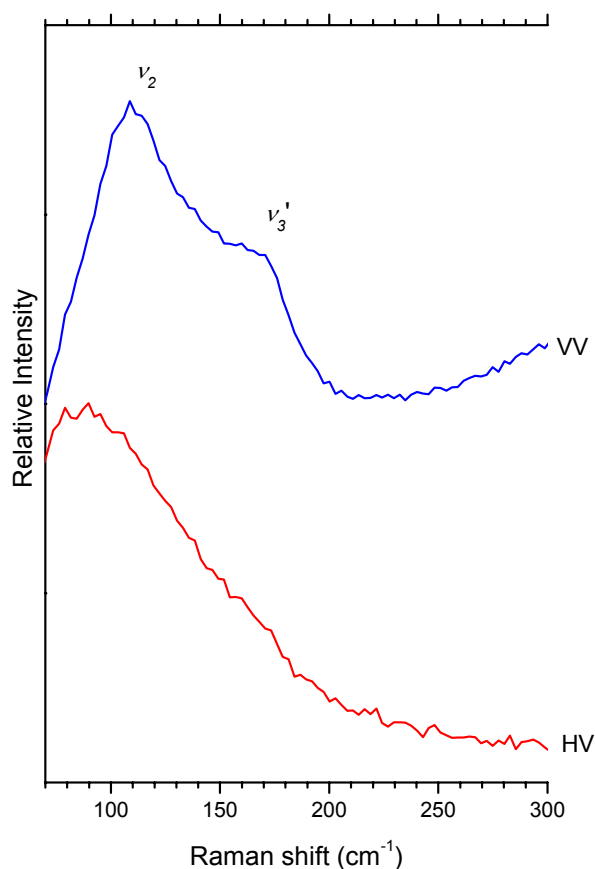
Figure 6.13: Raman spectra of liquid NdI$_3$ at 800°C in the quartz cell (cell 1). The spectra were recorded with 400 s of integration time and at the same conditions as Fig 6.3.

6.2.3. (NdI$_3$)$_x$-(NdI$_2$)$_{1-x}$

NdI$_2$:NdI$_3$ have been investigated for three values of x: 0.25, 0.5 and 0.75. At x=0.25 the system has a deep lying eutectic (497°C, Bredig 1964). At x=0.5 a maximum in the specific conductivity was found (Bredig 1964, Zein El Abedin 2002) which is due to an inter-valence charge transfer mechanism. Fig 6.14 shows the Raman spectra of the liquid mixtures together with those of the pure components. The full series at various temperatures can be found in the appendices A.6.1 to A.6.4. Besides the spectrum of pure NdI$_3$, there is only one point to mention: at x=0.5 the ν_1 and ν_2 bands of NdI$_3$ are still fairly visible. All other spectra are distorted by corrosion.
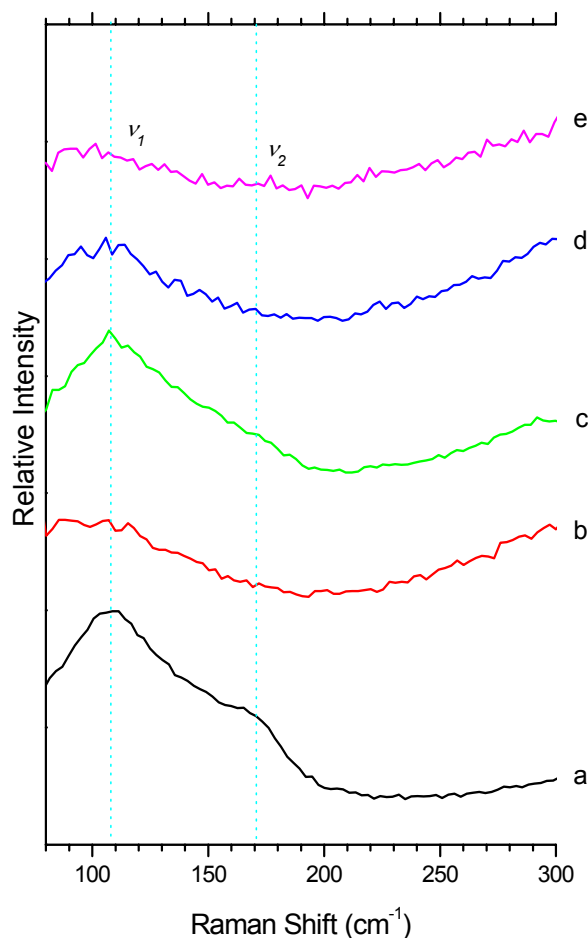
Figure 6.14: Raman spectra of (NdI$_3$)$_x$-(NdI$_2$)$_y$ melt in the cell 1. The spectra were recorded without polarizer, 400 s of integration time and at the same conditions as Fig 6.3.

     a) NdI$_3$ at 800°C.
     b) (NdI$_3$)$_{0.75}$-(NdI$_2$)$_{0.25}$ at 700°C.
     c) (NdI$_3$)$_{0.50}$-(NdI$_2$)$_{0.50}$ at 700°C
     d) (NdI$_3$)$_{0.25}$-(NdI$_2$)$_{0.75}$ at 600°C (eutectic).
     e) NdI$_2$ at 600°C

6.2.4. (NdI$_3$)$_x$-(LiI-KI)$_{eu, 1-x}$

The Raman spectra of (NdI$_3$)$_{0.05}$-(LiI-KI)$_{eu, 0.95}$ at various temperatures from 25°C to 600°C are shown in the Figures 6.15 and 6.16. The spectra of NdI$_3$ in the eutectic solvent are very similar to the corresponding CeI$_3$ spectra. The spectrum at 25°C shows a strong ν_2 band (~107 cm^{-1}), one broad ν_4 band (~172 cm^{-1}) which disappears at temperatures around 100°C, and three weak bands: ν_1 (~91 cm^{-1}), ν_3 (118 cm^{-1}), and ν_3' (~135 cm^{-1}). With increasing temperature the

bands ν_1 and ν_3 became broader. As the eutectic becomes molten (see spectra at $T \geq 300°C$) the character of the spectra change. They are now characterized by a single broad and polarized band shifted about 5 cm^{-1} to higher wave numbers with respect to the solid state ν_2 band.
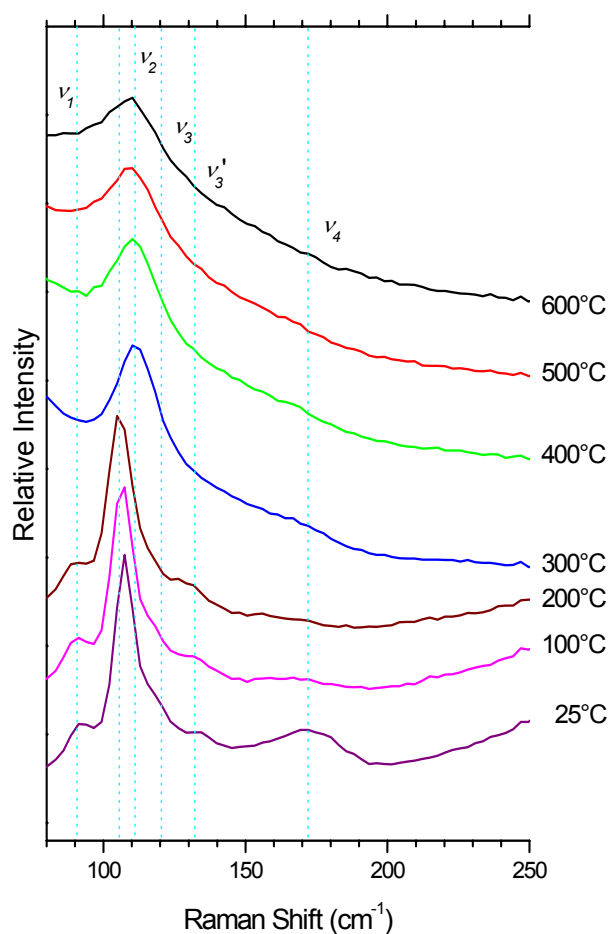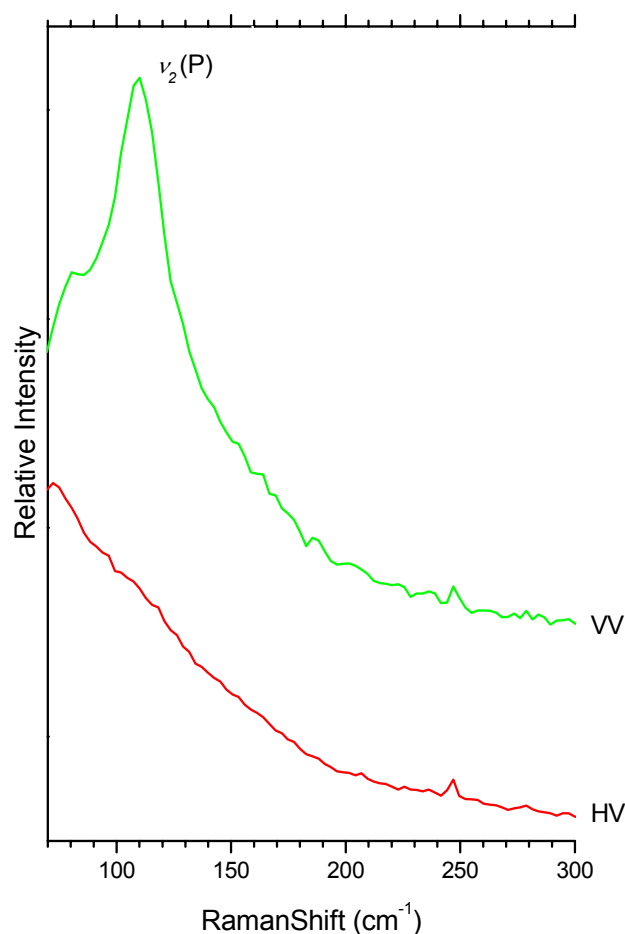

Figure 6.15: Raman spectra of $(NdI_3)_{0.05}$-$(LiI$-$KI)_{eu,\ 0.95}$ as function of the temperature in the quartz cell (cell 1). The spectra were recorded without polarizer, 200 s of integration time and at the same conditions as Fig 6.3.

Figure 6.16: Raman spectra of liquid $(NdI_3)_{0.02}$-$(LiI$-$KI)_{eu,\ 0.98}$ at 600°C in the quartz cell (cell 1). The spectra were recorded with 200 s of integration time and at the same conditions as Fig 6.3.

For the $(NdI_3)_x$-$(LiI$-$KI)_{eu,\ 1-x}$ mixtures there are no Raman spectra reported in the literature but, comparing them with the $NdCl_3$ in $(LiCl$-$KCl)_{eu}$, the polarized band may be attributed to octahedral NdI_6^{3-} species. In addition, complexation experiments of NdI_3-LI suggest the formation of octahedral species (Foosænas 1981) which supports our assumption.

6.2.5 $(NdI_3)_x$-$(NdI_2)_y$-$(LiI$-$KI)_{eu,\ 1-x-y}$

The Raman spectra of $(NdI_3)_x$-$(NdI_2)_y$-$(LiI$-$KI)_{eu,\ 1-x-y}$ melts are presented in Fig 6.17 without polarizer. The spectra at various temperatures as well as the HV- and VV-spectra in the liquid state can be found in the appendices A.6.5 to A.6.8.
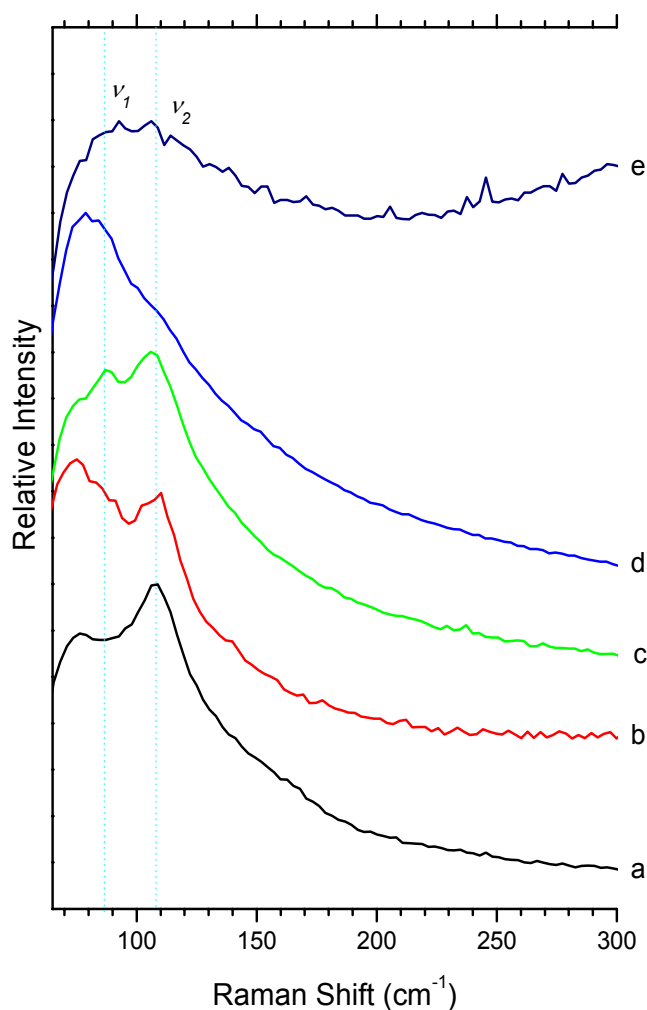

Figure 6.17: Raman spectra of liquid $(NdI_3)_x$-$(NdI_2)_y$-$(Li$-$KI)_{eu,\ 1-x-y}$, in the cell 1. The spectra were recorded without polarizer, at 500 °C, 200 s of integration time and at the same conditions as Fig 6.3.

        a) $(NdI_3)_{0.05}$-$(LiI$-$KI)_{eu,\ 0.95}$.
        b) $(NdI_3)_{0.075}$-$(NdI_2)_{0.025}$-$(LiI$-$KI)_{eu,\ 0.90}$.
        c) $(NdI_3)_{0.05}$-$(NdI_2)_{0.05}$-$(LiI$-$KI)_{eu,\ 0.90}$.
        d) $(NdI_3)_{0.025}$-$(NdI_2)_{0.075}$-$(LiI$-$KI)_{eu,\ 0.90}$.
        e) $(NdI_2)_{0.02}$-$(LiI$-$KI)_{eu,\ 0.98}$.

Spectrum *a* in Fig 6.17 shows the NdI_3-$(LiI-KI)_{eu}$ spectrum at 500°C with the dominant ν_2-band. With addition of NdI_2 this band becomes weaker and the signal to noise ratio of the spectrum decreases. This is presumably due to the corrosive effect of NdI_2. At a ratio NdI_2:NdI_3 of 3:1 the polarized band is hardly recognizable. The spectrum for $(NdI_2)_{0.02}$-$(LiI-KI)_{eu, 0.98}$ does not show any analyzable band.

7. Discussion

In this chapter a discussion of the results presented in chapters 5 and 6 is given. It is organized as follows: the first section provides a review of the physicochemical and structural properties reported in the literature of the substances here investigated. In the following, the systems are discussed in the sequence: rare earth trihalides, rare earth dihalides, and mixtures of rare earth metal with rare earth trihalides or, respectively, rare earth dihalides with rare earth trihalides.

It is known that the spectra, in which the electrical vector of the incident light is perpendicular to the electrical vector of the excited light (I_{HV}), have only contributions of the non totally symmetric vibrations, and when the electrical vector of the incident light is parallel to the electrical vector of the excited light (I_{VV}), then the contributions come from the symmetrical and asymmetrical vibrations. In order to have an account of the intensity of the symmetrical vibrations, in this chapter the spectra of the liquid rare earth halides are shown in the *iso* and *aniso* form. These are defined as follows (Bulkin 1991): $I_{iso} = I_{VV} - 4/3 \, I_{HV}$ and $I_{aniso} = 4/3 \, I_{HV}$ (see equations 2.14 and 2.15), respectively.

7.1. Structural and Physicochemical Data of Solid and Liquid LnX$_3$ and LnX$_2$

The physicochemical properties, and in particular the structural aspects, of LnX$_3$ and LnX$_3$-AX have been extensively studied, theoretically and experimentally, in recent years (Mochinaga 1993, Photiadis 1993, Photiadis 1998 and references cited therein, Wasse 1999,

Satyavathi 1979, Pavlatou 1997, Hutchinson 1999, Madden 1995, Madden 2000). Some important features are listed in tables 7.1 and 7.2.

Table 7.1: Structural data for some crystalline rare earth trihalides (Brown 1968 Haschke 1979, Gmelin 1982, Photiadis 1998)

Structure type (space group) symmetry	UCl_3 $(C6_3/m)$ Hexagonal (C_{6h}^2)	$PuBr_3$ (Cmcm) Orthorhombic (D_{2h}^{17})	YCl_3 (C2/m) Monoclinic (C_{2h}^3)	BiI_3 $(R\bar{3})$ Rhombohedral (C_{3i}^2)
Cl	La-Gd	Tb	Dy-Lu, Y	
Br	La-Pr	Nd-Eu		Gd-Lu, Y
I		La-Nd		Sm-Lu, Y
Ln^{3+}-X^-(Å)	1.63-1.93	1.96-2.17	1.99-2.13	2.08-2.55
Cation Coord. No. (CN)	9	8	6	6

Table 7.2: Some physicochemical properties of rare earth trichlorides and alkali halides on melting (Shannon 1976, Freyland 1995, Wasse 1999 and references cited therein).

[T_m: Temperature of melting; $\Delta V/V$: percentage volume change relative to the solid volume; σ: ionic conductivity of the liquid phase near the melting point; R+-: nearest neighbor cation-anion distances in the melt and corresponding crystalline data in brackets].

Salt	T_m(°C)	$\Delta V/V$ (%)	$\sigma(\Omega^{-1}cm^{-1})$	R_{+-}(Å)
Crystal structure UCl₃ type:				
$LaCl_3$	858-877	16-19.1	1.2-1.5	2.93
$LaBr_3$	788	12	0.6-0.8	3.01
$CeCl_3$	817	21.9	0.8-1.1	2.93
$CeBr_3$	732			3.01
$NdCl_3$	768	21.8	0.08	2.79
$SmCl_3$	662	24.5	0.5	2.77
$GdCl_3$	602	26.5	0.2	2.75

Crystal structure PuBr₃ type:

LaI$_3$	778	24	0.4	3.18
CeI$_3$	760		0.4	3.18
NdBr$_3$	682		0.5	2.94
NdI$_3$	782			3.18

Crystal structure YCl₃ type:

YCl$_3$	714	0.5	0.35-0.40	2.64
EuCl$_3$	775	5.3	0.3-0.4	2.66
AX:				
KCl	772	20.2	2.16	3.06(3.14)

Contrary to LnX$_3$ melts, less is known for pure divalent halide melts, with exception of the conductivity measurements performed by Bredig's group (for review and data collection see Bredig 1964). This lack of available information is mainly due to the extreme corrosive properties of the materials and to problems of disproportion, i.e. $3LnX_2 \rightarrow 2LnX_3 + Ln$, in some cases (Gmelin 1982, Meyer 1988). The experimental data found in the literature are listed in the table 7.3.

Table 7.3: Structural data for some crystalline rare earth dihalides
(Brown 1968, Haschke 1979, Gmelin 1982, Meyer 1988, Stöwe 1997)

Structure type (space group) symmetry	PbCl$_2$ (Pbmn) Orthorhombic (D_{2h}^{16})	CuTi$_2$ (14/mmm) Tetragonal (D_{4h}^{17})	SrBr$_2$ (P4/n) Tetragonal (C_{4h}^{3})
Cl	Nd, Sm, Eu	Tb	Dy
Br	Nd	Pm	Sm, Eu
I		La-Pr	Nd
Cation Coord. No. (CN)	9	8	8

7.2. LnX₃ and LnX₃-(LiX-KX)ₑᵤ Melts

In this section structural aspects of solid and liquid LnX_3, as well as solutions of LnX_3 in eutectic alkali halide mixtures, are discussed.

Using Raman spectroscopy Photiadis et al. (Photiadis 1993 and Photiadis 1998) have extensively studied the structural rearrangements upon melting of $NdCl_3$ and $NdCl_3$-AX (A=K, Li) mixtures. According to our investigations, our results are very similar to those of Photiadis et al. (table 7.4 and Fig 7.3). In the case of $CeCl_3$ and LnI_3, however, there is no reported information in the literature up to now.

7.2.1. LnX₃

The crystal structure of $LnCl_3$ is hexagonal. The lanthanides Ln^{3+} have a nine-fold coordination. Six halides are shared with neighboring Ln^{3+}. Three other halides are mainly associated with the central Ln^{3+} cation (Fig. 7.1). The crystal structure of LnI_3 is orthorhombic with an eight-fold coordination of the lanthanide ion, whereas the halide ions are two-fold coordinated and are located at similar positions along the y axis (Fig 7.2). The space symmetry are C_{6h}^2 and D_{2h}^{17} for $LnCl_3$ and LnI_3 respectively and the expected Raman active modes are (Ferraro 1969, Photiadis 1993, Photiadis 1998, Wilmarth 1988):

$$\Gamma_R\left(C_{6h}^2\right) = 2A_g + E_{1g} + 3E_{2g}$$

$$\Gamma_R\left(D_{2h}^{17}\right) = 4A_g + 3B_{1g} + B_{2g} + 4B_{3g}$$

○ Ln(1/4)
◉ Ln(3/4)
◯ Cl(1/4)
◯ Cl(3/4)
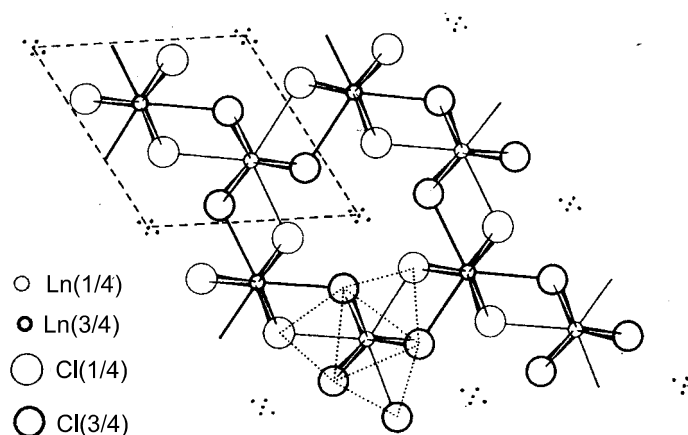
Figure 7.1: Projection of the crystal structure of solid $LnCl_3$. (From A. F. Wells, Structural Inorganic Chemistry, Clarendon Press, Oxford, 1962).

O Ln at y=0   ◯ Cl at y=0

O Ln at y=1/2   ◯ Cl at y=1/2
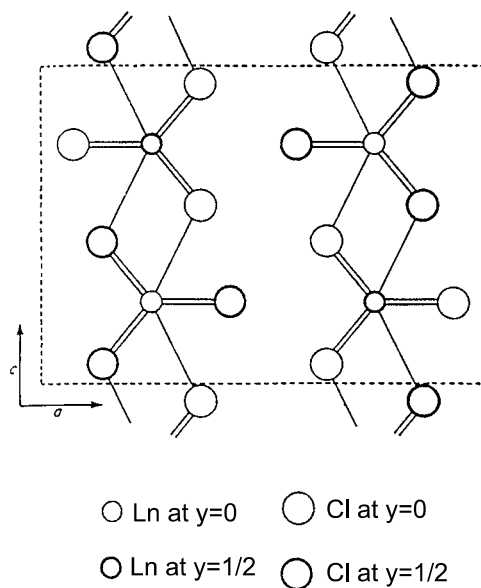
Figure 7.2: Crystal structure of solid LnI₃. (From A. F. Wells, Structural Inorganic Chemistry, Clarendon Press, Oxford, 1962)

In the case of NdCl₃ (C_{6h}^2 symmetry), from the expected six modes only four were observed in the spectra at room temperature: v_2, v_4, v_5, v_6 (Table 7.4). With increasing temperature certain bands overlapped ($v_5 + v_6$), yielding finally at temperatures up to ~400°C a spectrum that consisted of two main bands. For CeCl₃, only the overlapped bands $v_3 + v_4$ and $v_5 + v_6$ could be observed in the spectra corresponding to the solid state (below 700°C, Appendix A.4.2), which are also reported in Table 7.4. On the other hand, in the case of LnI₃, only four main bands were observed in the spectra at room temperature: v_1, v_2, v_3, v_4 (Table 7.4). With increasing temperature the v_4 band disappears and at temperatures up to 400°C the spectra consisted of three main bands: v_1, v_2, v_3 (see also Figs 6.3 and 6.12).

Upon melting, the spectra of the LnX₃ change considerably. They show now two polarized and two depolarized bands (Table 7.4 and Fig 7.3). Fig 7.3 also shows a comparison of the NdCl₃ spectra obtained in this work with the spectra reported in the literature. Here is possible to observe that our results are in agreement with those of the literature. The differences among the spectra at frequencies lower than 150 cm⁻¹ are due to the notch filter used in this work, which suppresses the Rayleigh line (as explained before in chapter 3). Some authors recommend the use of the reduced intensity (eqn 2.16) for the quantitative

Raman analyses, because with that it is possible to remove the Rayleigh intensity and to establish the presence of weak Raman bands in the region of 10-200 cm^{-1}. Moreover, the reduced Raman spectrum is directly proportional to the intrinsic molar scattering factor, which is a measure of the square of the derivative of the polarizability tensor α with respect to the normal coordinate [$(\partial\alpha/\partial Q)_0$, eqn 2.5]. This reduced form is well suited for comparisons with the infrared absorption spectrum and the inelastic neutron scattering spectrum (Brooker 1988). In the case of NdCl$_3$ such analysis is useful to obtain the depolarized band D$_1$ at 123 cm^{-1} (Table 7.4 and Fig 7.3). However, in our case the D$_1$ band interferes with the cut off of the notch filter and we recognize it only by comparison with the literature. The two polarized and the two depolarized bands observed in the NdCl$_3$ spectra are attributed to a distorted octahedral-loose-network structure (Photiadis 1993).

Table 7.4: Observed Raman bands of solid and liquid LnX$_3$

LnCl$_3$	T(°C)	Solid						Source
		Main Frequencies (cm^{-1})						
		ν_1	ν_2	ν_3	ν_4	ν_5	ν_6	
NdCl$_3$	25		147		191 w	217 w	224 w	Fig A.3.1
		103 (E$_{2g}$)	151 *	183 (E$_{2g}$)	192 (E$_{1g}$)	218 (A$_g$)	223 (E$_{2g}$)	(a)
	400			181		213		Fig A.3.1
		98		185		218		(a)
				(E$_{2g}$+E$_{1g}$)		(A$_g$+E$_{2g}$)		
	750					213		Fig A.3.1
		90		176		212		(a)
CeCl$_3$	25			173	181	205	212	Fig A.4.2
		102		178	184	208	218	(b)
	400			172		196	206	Fig A.4.2
	700			168			204	Fig A.4.2

LnCl$_3$	T(°C)	Liquid				Source
		Main Frequencies (cm^{-1})				
		P$_1$	P$_2$	D$_1$	D$_2$	
NdCl$_3$**	780	249	322	-	220	Fig 5.1
		251	320	123	223	(a)

* This feature corresponds to an electronic Raman band (see Photiadis 1993).
** The frequencies of the bands where obtained using the reduced form of the spectra.
(a) Damen 1968, Schaack 1970.
(b) Photiadis 1993.
w: weak band.
The assignment and numbering of the ν_i is done arbitrarily in the present work.

		Solid				
LnI$_3$	T(°C)	Main Frequencies (cm^{-1})				Source
		ν_1	ν_2	ν_3	ν_4	
NdI$_3$	25	103	114	139	299	Fig 6.12
	400	99	111	130		Fig 6.12
	600	88	109	140		Fig 6.12
CeI$_3$	25	90	101	126	258	Fig 6.3
	400	88	98	121		Fig 6.3
	700	84	95	119		Fig 6.3

		Liquid				
LnI$_3$	T/°C)	Main Frequencies (cm^{-1})				Source
		P_1	P_2	D_1	D_2	
NdI$_3$	800	110	155	107	166	Fig 6.13
CeI$_3$	780	110	157	108	161	Fig 6.4
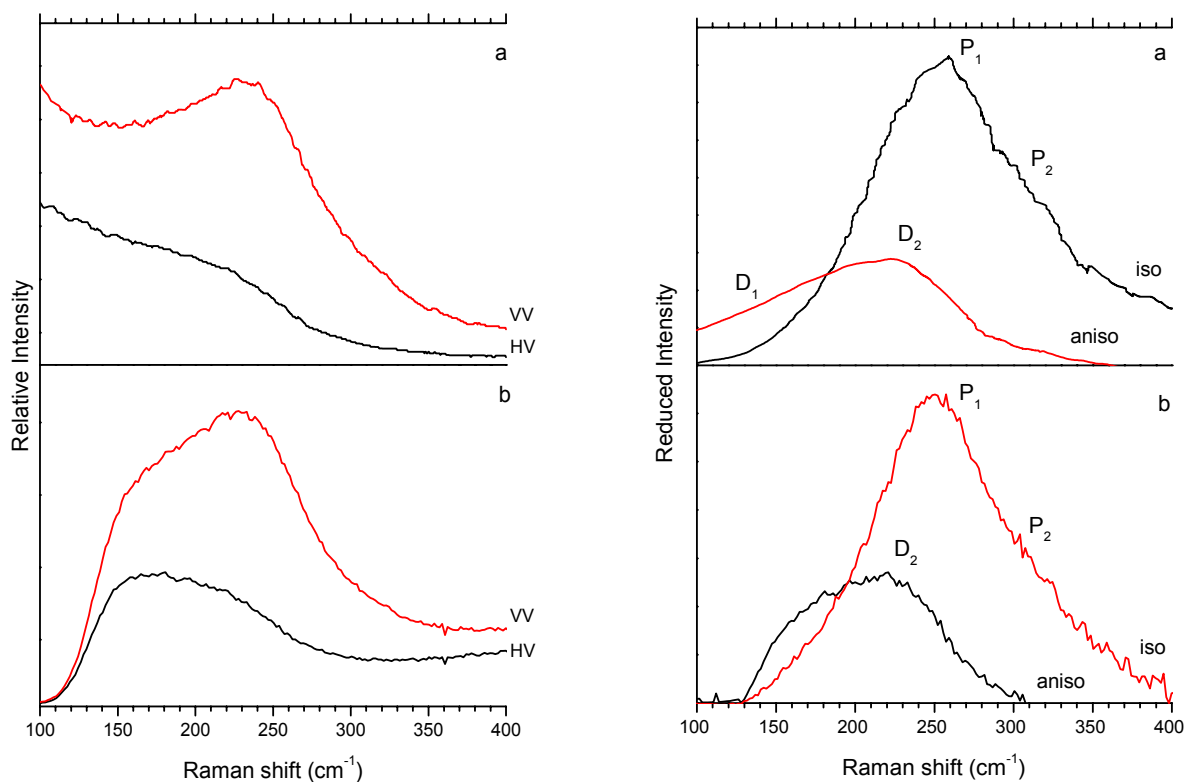
Figure 7.3: Normal and reduced Raman spectra of liquid NdCl$_3$ at 780°C: (a) Photiadis 1993, (b) our results. Assignments of P_1, P_2, D_1 and D_2 according to Photiadis 1993.

In that sense, the measured spectra (Fig 7.5, upper panel) indicate that the dominant structure of the melts in LnX$_3$ systems (where Ln = {Ce, Nd} and X = {Cl, I}) is the distorted octahedral complex LnX_6^{3-}, where a loose-network-like structure is formed consisting of octahedra sharing edges (Fig 7.4). It means that the coordination number (CN) around a rare earth cation decreases from 9 to 8 for the crystalline and to 6 in the liquid state, which is indeed supported by measurements of molar volume expansion and preliminary Raman spectroscopic measurements (Mochinaga 1993, Pavlatou 1997, Photiadis 1998 and references cited therein, Papatheodorou 2000). Electronic absorption spectra are also in agreement with this finding (Photiadis 1998). The space symmetry of the LnX_6^{3-} species is D_{3d}^1, for which the expected Raman active modes are (Ferraro 1969, Photiadis 1993, Photiadis 1998):

$$\Gamma_R\left(D_{3d}^1\right) = 2A_{1g} + 4E_g$$
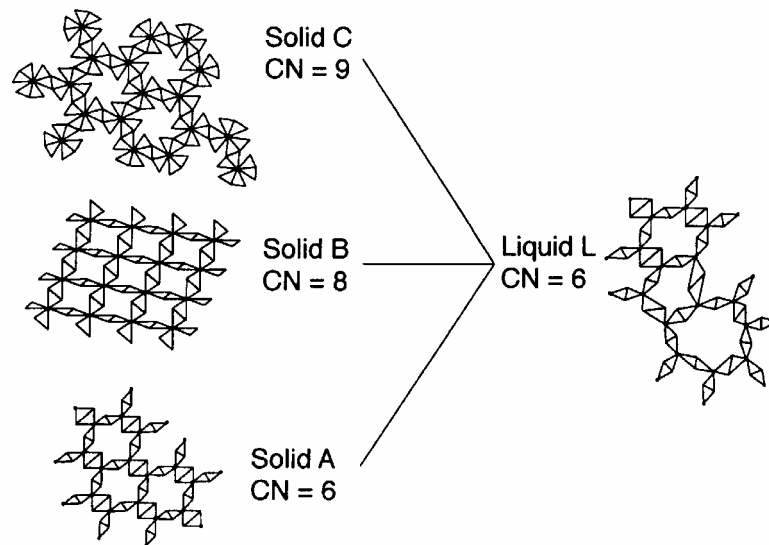
Figure 7.4: Schematic skeletons of solid and molten rare earth trihalides: Solid A, monoclinic or rhombohedral; Solid B, orthorhombic; Solid C, hexagonal (Photiadis 1998).

On diluting the pure LnX$_3$ melts with alkali halides the polarized band P$_1$ survives as octahedral A$_{1g}$ vibration. It is shifted only slightly. In the same sequence the polarized band P$_2$ disappears. The comparison of our LnX$_3$-(LiX-KX)$_{eu}$-systems with available literature spectra lead us to the assignment of the LnX$_3$-systems as shown in Fig 7.5: the band P$_1$ was related to the A$_{1g}$ vibration in the LnX$_3$-(LiX-KX)$_{eu}$-systems; different to the iodide systems, the band P$_2$ is hardly discernible in the chloride system. This is probably due to the blackbody

background radiation. Therefore, we have assigned the P_2 band according with $NdCl_3$ results of Photiadis et al. (Photiadis 1993 and Photiadis 1998).
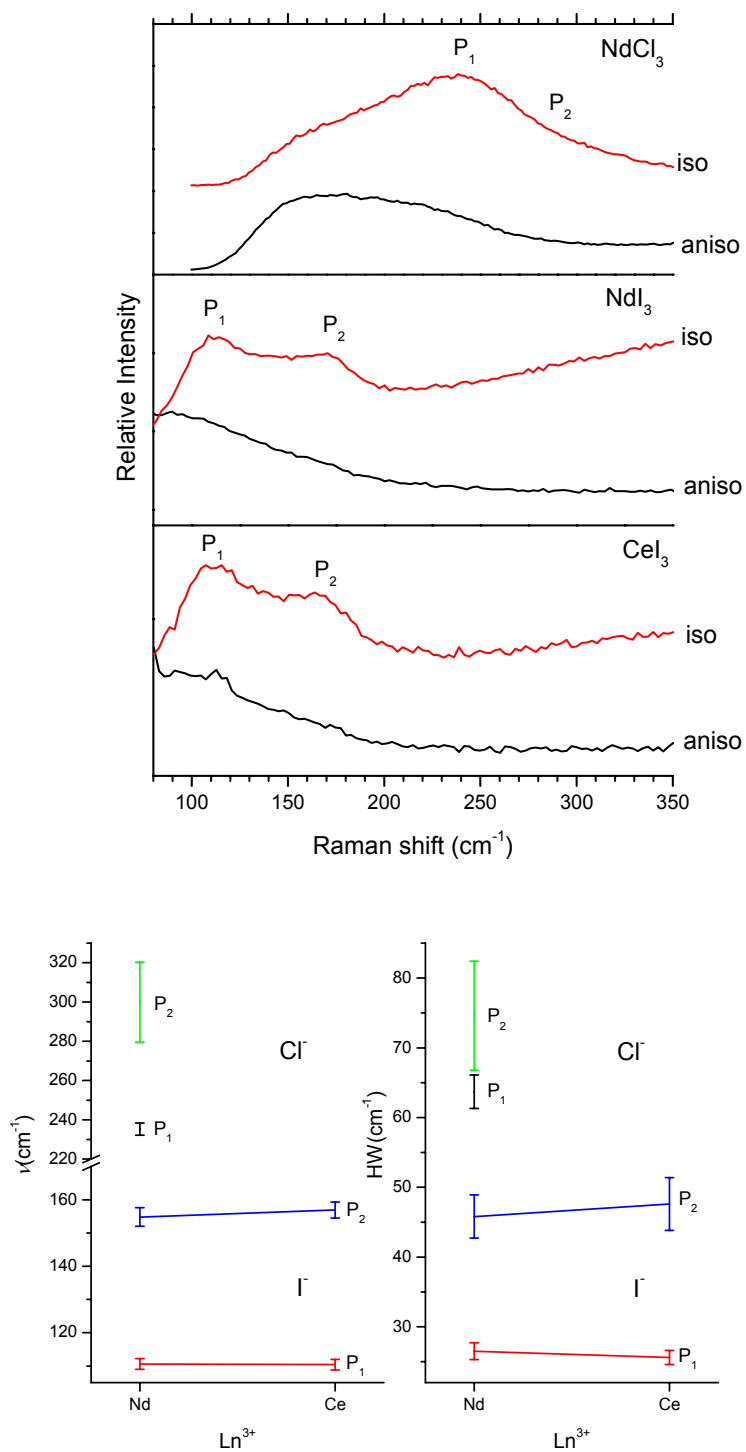
Figure 7.5. Upper panel: iso- and aniso- Raman spectra of liquid LnX_3: $NdCl_3$ and CeI_3 at 780°C, NdI_3 at 800°C. Lower panel: spectral parameter of the polarized bands P_1 and P_2: peak frequency (ν) and band width (HW).

The separation of the P_1 and P_2 bands give some insight into the distortion of the octahedra in the melt. This separation in the spectra of the LnX₃, which is 41% for LnI₃ and only 28% for NdCl₃ (Fig 7.5, lower panel), is due to the competition between attractive coulombic Ln^{3+}–X^- and repulsive X^-–X^- interactions. These interactions determine the degree of the octahedral distortions (Photiadis 1998). From this, it is possible to conclude that the degree of distortion increases in the order $Cl^- \rightarrow I^-$.

On the other hand, the band widths increase in the order $I^- \rightarrow Cl^-$. This can be a consequence of different factors: (a) a strong coupling between the vibrations of the octahedral units within the network phase; (b) the inhomogeneous octahedral environments, which contain Ln^{3+} ions with varying degrees of corner and edge sharing; and, (c) the bands could be lifetime broadened. In a computer simulation study of the vibrational density of states, Pavlatou et al. (Pavlatou 1997) discusses this aspect in more detail. From their results, fluctuation effects are responsible for the band width, which supports the idea that inhomogeneous and life time broading are the dominating effects.

7.2.2. LnX₃-(LiX-KX)ₑᵤ

It is known that the addition of AX (A=Li, K) to NdCl₃ leads to a continuous destruction of the loose-network structure D_{3d}^1. Consequently, in alkali halide rich (e.g. $x_{NdCl_3} \leq 0.25$) molten mixtures the normal octahedral $NdCl_6^{3-}$ species dominate, as shown in Fig. 7.6 (Pavlatou 1997, Photiadis 1993, Photiadis 1998). Thus, the spectra of the molten NdCl₃ in (LiCl-KCl)ₑᵤ show only one polarized and one depolarized bands (see Figs 5.6 and 7.7, upper panel).

The observed Raman spectra for all the liquid mixtures of LnX₃ in LiX-KX eutectic reported in this work are very similar (Fig 7.7, upper panel). Accordingly, it is possible to conclude that in all these mixtures the undistorted octahedra are the predominant species, and the change in the spectra can be explained as follows: with the addition of AX in the LnX₃ melts, the LnX_6^{3-} species become more and more decoupled until they form the symmetrical octahedron. Then, the correlation of the vibrational modes by changing the symmetry occurs according to the following scheme:

$$A_1(P_1) \rightarrow A_{1g}(P_1) \qquad E(D_2) \rightarrow E_g \qquad A_1(P_2)+E(D_1) \rightarrow F_{2g}(D_1)$$
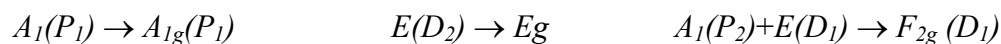
where P means polarized and D depolarized bands (Photiadis 1998). In this form, the expected Raman active modes for the new symmetry (O_h) are:

$$\Gamma_R(O_h) = A_{1g} + E_g + F_{2g}.$$

(a)   (b)
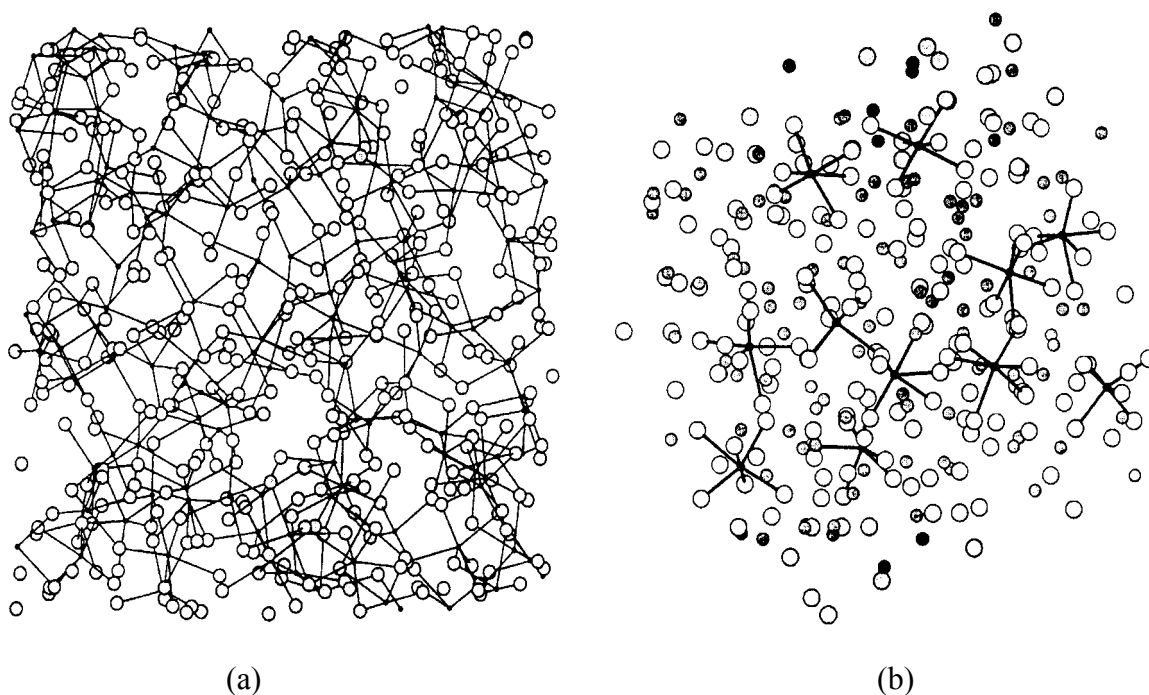
Figure 7.6: Molecular picture of (a) pure $LnCl_3$, (b) 20% $LnCl_3$ in 80% KCl. The largest spheres are the Cl^-, the smallest the Ln^{3+} and the medium the A^+ [only in (b)] (Pavlatou 1997).

From the three Raman active modes only two are observed in the melts (A_{1g} and F_{2g}). In our case the F_{2g} band is difficult to determine since it interferes with the notch filter edge. For Cl^- as well as for I^- as ligand we observe an increasing of the vibration frequency from Ce to Nd. This trend is in good agreement with the study of the vibrational frequencies of Ln hexahalides (Choca 1975). On account of the lanthanide contraction, the ionic radius decreases from Ce to Nd (Table 7.2). This may strengthen the chemical bond between the central ion and a ligand which leads to a higher vibrational frequency.
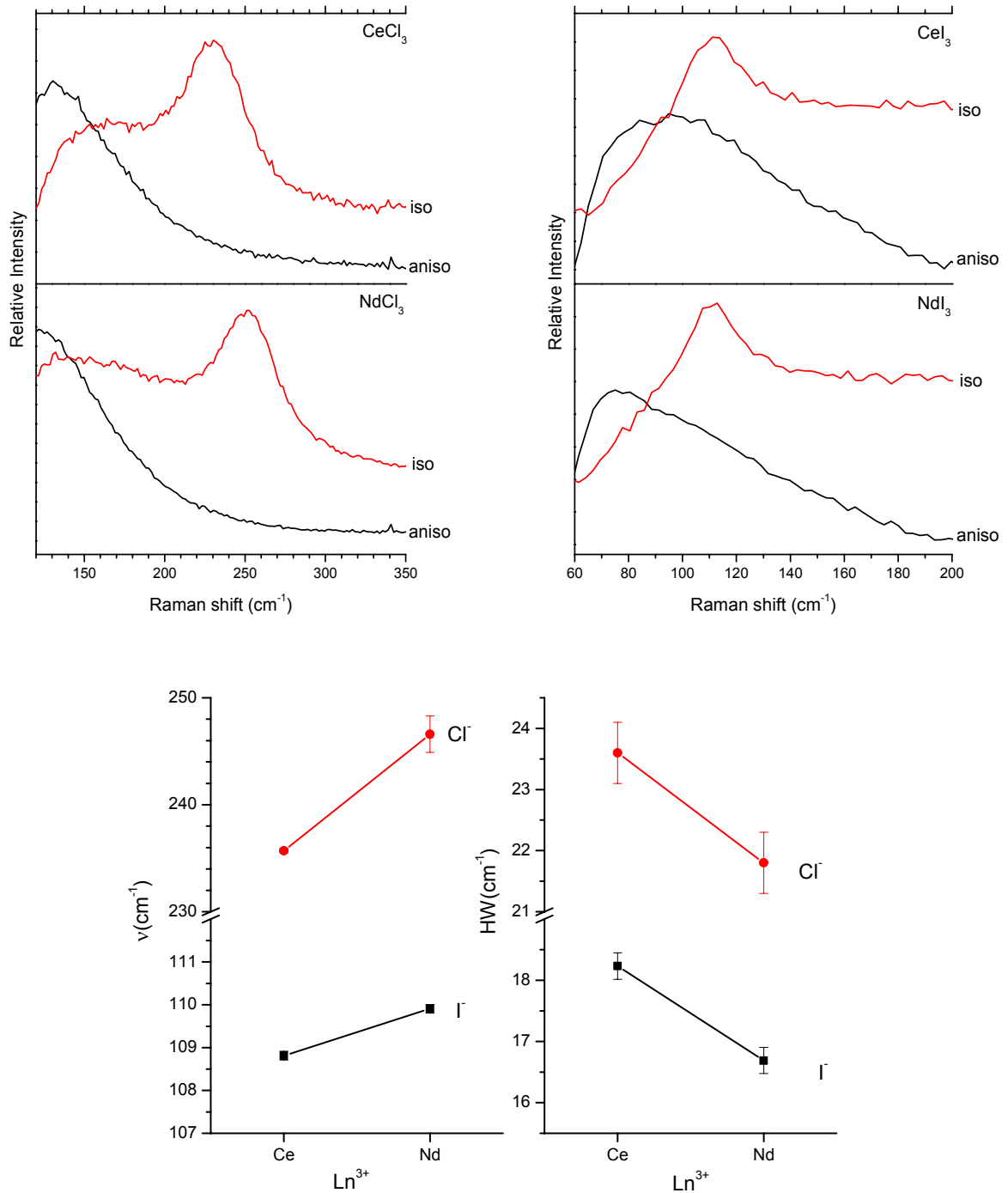
Figure 7.7. Upper panel: I_{iso} and I_{aniso} spectra of $(LnX_3)_{0.05}$-$(LiX-KX)_{0.95}$ at 600°C. Lower panel: the ν_2 frequency and band width (HW) of the LnX_6^{3-} species.

The calculation of the force constant for the vibronic motion of the octahedra is not straight forward. It requires a normal coordinate treatment and the application of a suitable

valence force field. This has been already discussed for $LnCl_6^{3-}$ and $LnBr_6^{3-}$ (Choca 1974). Comparing various force fields, they give a metal-halogen stretching force constant for $LnCl_6^{3-}$ of 72 to 79 Nm^{-1} and a significantly lower one for $LnBr_6^{3-}$ of 54 to 59 Nm^{-1}. This means that, for the observed frequency shift, the mass change can partly account.

To get a rough estimation for the force constant of the LnI_6^{3-} species we have plotted $v_1^2 \cdot m_x$ vs. the force constant of Choca et al. (Choca 1974). In this way we obtained a metal-iodine stretching force constant of 40 to 50 Nm^{-1}. This continues the trend of weaker bonds with increasing ligand size. The reason for this is probably the stronger steric repulsion of the larger ligands.

7.3. LnX$_2$ and LnX$_2$-(LiX-KX)$_{eu}$ Melts

To our knowledge, there are no Raman studies on liquid LnX$_2$ (Ln= Ce, Nd) and their mixtures with alkali halides reported in the literature. The main reason for this is certainly the strong corrodibility of these substances. In addition, some of them have volatility high enough to cover the optical window of the cells. Even with our improved Raman technology these shortcomings have been overcame only partly.

7.3.1. NdCl$_2$

The NdCl$_2$ crystallizes in the orthorhombic PbCl$_2$-type structure (Fig 7.9) with a nine-fold coordination of neodymium (Druding 1959, Gmelin 1982, Meyer 1988). The space symmetry of this structure is D_{2h}^{16}. It has to be noted that there are different reduced representations of Raman active modes for the same crystal structure reported in the literature. This can be due to the difficulty in determining the main axis of the structure in order to perform a factor group analysis for the determination of the Raman active modes (Brooker 1975). The following representations of the space group D_{2h}^{16} have been reported in the literature:

$$\Gamma_R\left(D_{2h}^{16}\right) = 6A_g + 6B_{1g} + 3B_{2g} + 3B_{3g} \quad \text{(Mendes-Filho 1979, for a PbCl}_2 \text{ crystal)}$$

$$\Gamma_R\left(D_{2h}^{16}\right) = 3A_g + B_{1g} + B_{2g} + B_{3g} \qquad \text{(Brooker 1975)}$$

$$\Gamma_R\left(D_{2h}^{16}\right) = 3A_g + 2B_{1g} + 1B_{2g} \qquad \text{(Ferraro 1969)}$$
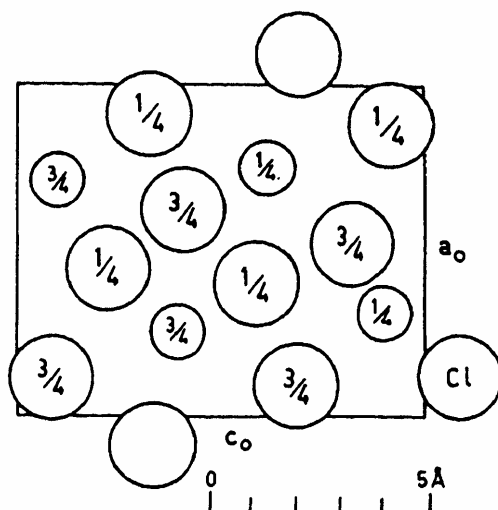
Figure 7.9: Orthorhombic PbCl₂-type structure projected along its crystallographic *b*-axis. The cation and the chlorine are situated on the *ac* mirror planes with $y = ¼$ and ¾ (from Mendes-Filho 1979).

The common Raman spectrum of powdered NdCl₂ solid at 25°C obtained in the present work shows four main bands, which are depolarized (ν_1':114, ν_1:175, ν_3:346, ν_4:454 cm⁻¹), and one very weak (ν_2':210 cm⁻¹), which is probably polarized (Fig 5.4). The assignment of the bands to a vibrational mode remains still unresolved. This requires polarization dependent measurements on oriented single crystals.

NdCl₂ has the same structure as EuCl₂. Its Raman spectrum in the solid and liquid state was described by Koyoma and coworkers (Koyoma 1997). Similar to NdCl₂, it exhibits four main bands in the solid state at room temperature. PbCl₂, the prototype of the given structure, was studied very carefully at 16 K and between 100°C and temperatures above the melting point (501°C) (Mendes-Filho 1979). The rich band structure at low temperatures merges to a few main bands at 100°C. This, again, can be qualitatively compared to the NdCl₂ case. The PbCl₂ and EuCl₂ systems show both a broad band in the liquid state, which is weaker in the case of PbCl₂. These bands arise presumably from distorted octahedral and tetrahedral species. One could expect a similar type of spectra for liquid NdCl₂. Within this work we did not obtain an analyzable spectrum of pure NdCl₂ in the liquid state.

NdCl₂ in NdCl₃ and NdCl₃-(LiCl-KCl)ₑᵤ Mixtures in Cell 2?

As previously mentioned (chapter 5, sections 5.1.1. and 5.1.3), the spectra of $NdCl_3$ and its mixtures with LiCl-KCl eutectic, recorded in the cell 2, show four relatively sharp main bands, which are certainly very similar to those of $NdCl_2$ (Figs 5.2 and 5.7). On the other hand, our spectra of $NdCl_3$ in cell 1 and cell 3 are in good agreement with the literature (Photiadis 1993, Fig 7.10). The main difference between cell 2 and cells 1 and 3 is the Mo heater closely adjacent to the sample in the open crucible. The hot Mo wires may act as a getter material for Cl_2. In such a way the equilibrium of

$$NdCl_3 \Leftrightarrow NdCl_2 + 1/2\,Cl_2$$

can shift to the right side. Employing DTA and thermogravimetry Laptev et al. (Laptev 1986) confirmed that $NdCl_3$ tends to decompose at 400°C to 500°C. Using a closed system like cell 1 or cell 3 without a sink for Cl_2, the equilibrium of the above reaction seems to be strong enough on the left side even at conditions above the melting point.
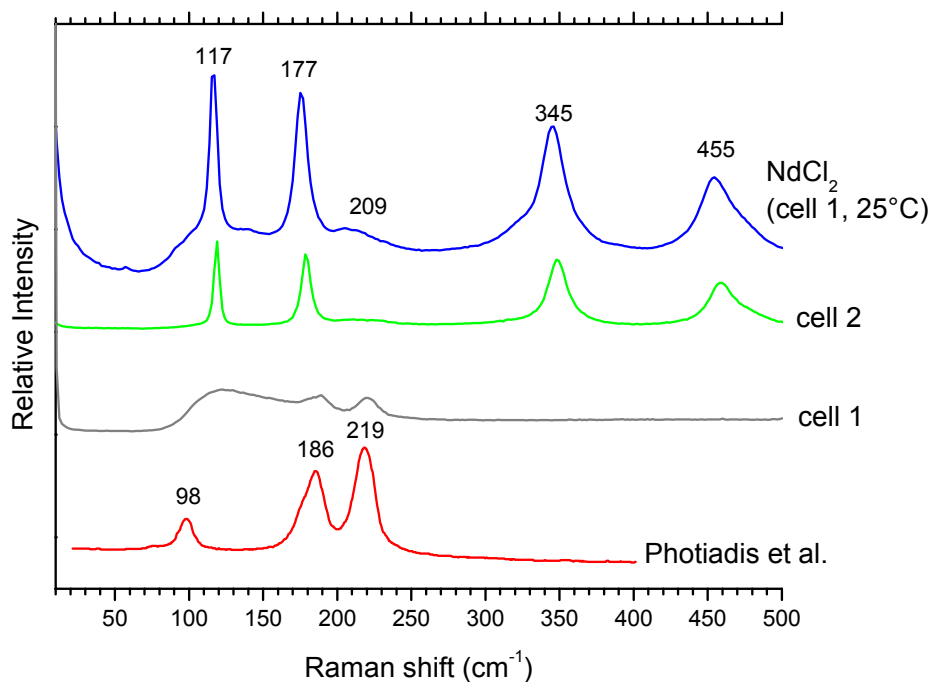
Figure 7.10: Comparison of $NdCl_3$ Raman spectra in the quartz cell (cell 1) and in the windowless cell (cell 2, after heating) at 400°C with literature results (Photiadis 1993) and with $NdCl_2$ at 25°C in cell 1.

In the context of the formation of NdCl$_2$ in cell 2 we have to describe another surprising and interesting phenomenon: Hase et al. (Hase 1981) and Del Cul et al. (Del Cul 1992) have studied the Raman spectra of single crystalline LnOCl. At first glance, the Raman spectrum of solid NdOCl looks very similar to that of pure solid NdCl$_2$ at room temperature and to that of the product formed in cell 2 from NdCl$_3$. However, the maxima of all five bands of NdCl$_2$ (see Fig 7.10) are shifted by a few wave numbers with respect to those of NdOCl. The difference is small but significant. At the same temperature the Raman bands of NdCl$_2$ are broader by 50%. In contrast to NdOCl the weak band at 210 cm^{-1} is polarized in NdCl$_2$. Finally, NdOCl single crystals are described as "transparent pale purple" coloured (Aride 1982) whereas NdCl$_2$ is dark green or almost black. In cell 2, NdCl$_3$ was heated in an inert atmosphere containing only traces of oxygen. Then, it is impossible that under such condition NdCl$_3$ could be converted nearly quantitatively to NdOCl. Mediaas et al. (Mediaas 1997 and Mediaas 2000) studied the NdCl$_3$-NdOCl system by Raman spectroscopy and showed that the network-like structure of chlorine edge-sharing $NdCl_6^{3-}$ octahedra in the pure liquid NdCl$_3$ is not changed significantly by the addition of NdOCl. Furthermore, they showed that the structure of isolate octahedral $NdCl_6^{3-}$ in the mixtures of NdCl$_3$ in alkali halides do not change when NdOCl is added. In contrast to Mediaas et al., the structure of our spectra for pure NdCl$_3$ and its mixtures with alkali halides looks in fact very different (four well defined bands, Fig 7.10), which indicates the existence of NdCl$_2$.

7.3.2. CeI$_2$ and NdI$_2$

For the sake of completeness the structures of CeI$_2$ and NdI$_2$ are shown in Fig 7.11 and 7.12, respectively. CeI$_2$ has a tetragonal crystal structure of the Ti$_2$Cu-type (Gmelin 1982, Meyer 1988). The coordination number of Ln^{2+} is [8+2], which means that Ln^{2+} is surrounded by eight iodine ions at close distance and by two additional ions a little farther. This leads to a layer type structure (Stöwe 1997). The space symmetry of this structure is D_{4h}^{17}, for which the following Raman active modes are expected (Brooker 1975a):

$$\Gamma_R = 2A_{1g} + 2E_g .$$
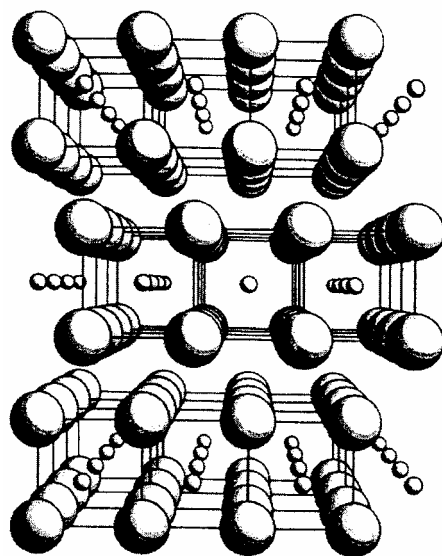
Figure 7.11: Structure of the CeI$_2$ (Ti$_2$Cu-Type) viewed along [100] (from Beck 1992).

Although CeI$_2$ and CeI$_3$ have different crystal structures, the Raman spectra of both salts in the solid state (25°C-400°C) are very similar (Figs 6.3 and 6.5). They differ only in the intensity distribution of the bands. The spectra of CeI$_3$ can be recorded to significantly higher temperatures. In the temperature range above 500°C the spectra of CeI$_2$ are disturbed by either corrosion of the cell 1 or by sublimation of the salt in cell 3.

The electronic structure of CeI$_2$ is sometimes illustrated by using the formula $(Ce^{3+})(e^-)(I^-)_2$ (Corbett 1961, Meyer 1988). One electron is only loosely related to Ce^{3+}, which gives rise to a high electronic conductivity (Dworkin 1963). Such a weakly localized or even free electron is not visible in the Raman spectra, but it should influence the optical absorption spectra. However, these spectra do not show any indication for such an electronic state. If these defect states are visible in the experimentally accessible spectral UV-VIS-NIR range above 0.5 eV, it depends strongly on the concentration of the electron and on its mobility. If the concentration is small and the mobility high, then the spectrum of these type of defect electron is shifted below 0.5 eV (Terakado 2002).

NdI$_2$ crystallizes with a tetragonal SmBr$_2$-type structure (Fig 7.12) and space symmetry C_{4h}^3, for which the expected Raman active modes are (Ferraro 1969):

$$\Gamma_R = 2A_g + 2B_g + E_g .$$
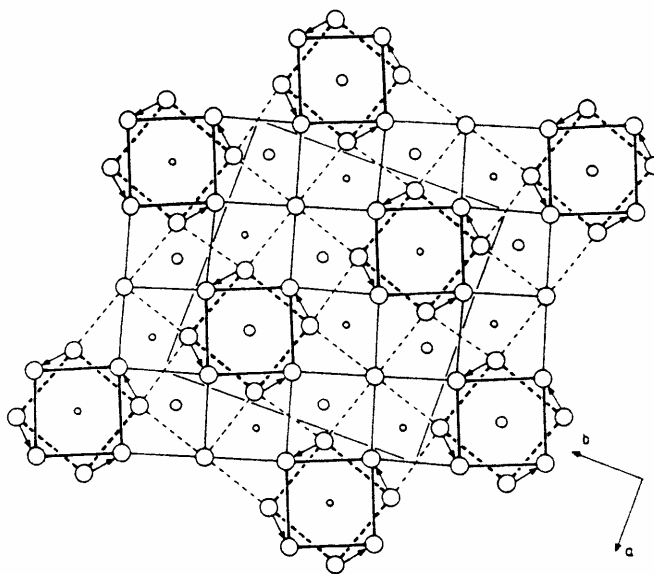
Figure 7.12: Structure of the NdI₂ (SrBr₂-Type) viewed along [001] (from Beck 1992).

In contrast to CeI$_2$, neodymium diiodid contains a "true" Nd^{2+} ion. This was already confirmed by ESR (Corbett 1961). NdI$_2$ should also be stable in the melt. However, we could not observe analyzable Raman spectra in the solid as well as in the liquid state. The reason for this is not clear so far.

7.3.3. LnCl$_2$-(LiCl-KCl)eu

The systems PbCl$_2$-KCl (Maroni 1971) and EuCl$_2$-NaCl (Koyoma 1997) may be selected to draw a comparison with our present system NdCl$_2$-(LiCl-KCl)$_{eu}$. On melting of the alkali halide and dissolving of the MX$_2$ the Raman spectra change considerably. In the case of PbCl$_2$- KCl a broad band is attributed to symmetric stretching motion of single species of the type $PbCl_n^{2-n}$ (n=2 to 4). A broad band of probably distorted octahedral species is seen in pure liquid EuCl$_2$. In contrast to the trihalide dissolved in alkali halides, no distinct octahedral band appears on addition of NaCl.

Again, the situation is different in NdCl$_2$-(LiCl-KCl). Even after homogenization (as seen by the rich band structure after cooling to the solid state) the typical spectra of solid NdCl$_2$ remain dominant in the liquid eutectic (see Fig 5.9, T=400°C). Unfortunately, the

phase diagram of $NdCl_2$-$(LiCl$-$KCl)_{eu}$ is not known and, in consequence, we do not know the solubility of the $NdCl_2$ as function of the temperature.

If one compares with $EuCl_2$-$NaCl$ it is not unlikely that dissolved $NdCl_2$ would not show a significant Raman band. A possible reason for this behavior could be the higher negative charge which might not favor the formation of symmetric octahedral species.

7.3.4. LnI$_2$-(LiI-KI)$_{eu}$

It is interesting to see a similar trend in the case of CeI_2-$(LiI$-$KI)_{eu}$. The dissolution process of CeI_2 in the alkali halide can be followed in Fig 6.9. When the alkali halide is liquid the spectra of CeI_2 change drastically. Now, ν_1 is the dominant band (see Fig 7.13). But on further heating only ν_2 is still discernable as a polarized band. ν_1 is now hardly detectable because of the close vicinity of the notch filter edge. In comparison to CeI_3-$(LiI$-$KI)_{eu}$ (see Fig 6.8) the intensity of the ν_2 band which might be due to the symmetric octahedral vibration, is drastically smaller. Perhaps in the $Ln(II)X_2$ system the octahedral complex formation seems to be less favored.
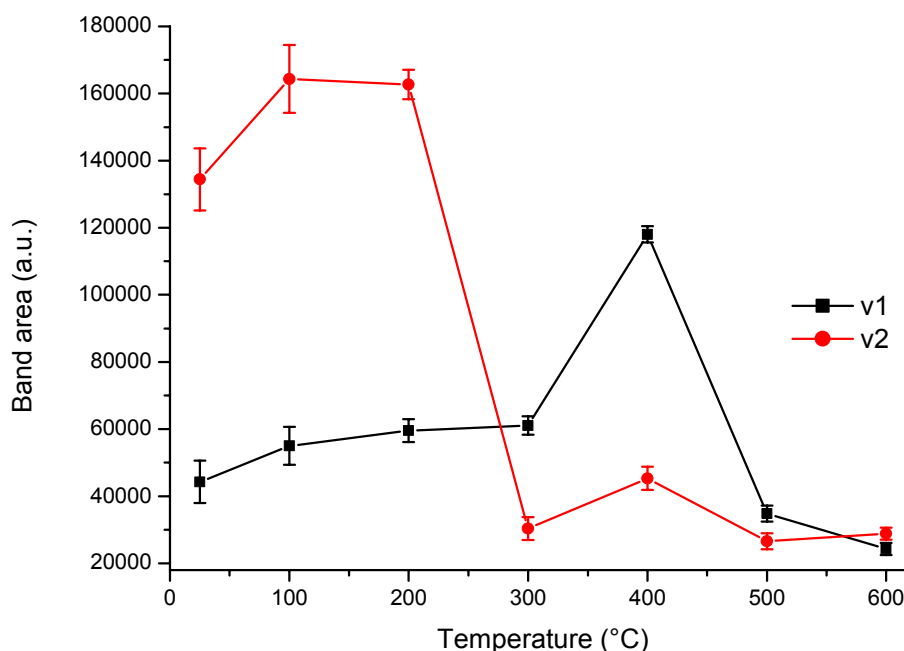
Figure 7.13: Band area of ν_1 and ν_2 obtained with the spectral analysis of Fig 6.9.

7.4. Mixed Rare Earth Metal-Rare Earth Halide (Ln-LnX₃) Systems

A main goal of this work is the study of the Raman spectra of mixed metal-molten salt solutions. This lead us to the question if and how the specific type of electron localization of a system influences the microscopic structure in that system. For this, it is of interest to summarize two prototypical scenarios of electron localization in metal-molten salt solutions, as follows.

7.4.1. Alkali Metal-Alkali Halide Solution: F-Centers, Bipolaron and Drude Electrons

These systems are quite well studied and understood. Briefly, as the alkali melt dissolves in the liquid alkali halide, the liquid analogue of the F-center is formed. At higher concentrations (x_M of the order of 0.01) dimer states come into play (bipolarons). In equilibrium with these strongly localized states mobile Drude-like electrons have been identifyed, which are responsible for the strong increase of the conductivity with metal concentration (Bredig 1964, Warren 1985, Freyland 1994, Freyland 1995).

These types of electronic defect species are not expected to have a strong influence on the Raman spectrum of an alkali metal- alkali halide system. Only the details of the Rayleigh shoulder may be altered. However, if these types of defect states are formed in a (LnX_2)-(LnX_3)-$(LiX\text{-}KX)_{eu}$ solution by oxidation of LnX_2 to LnX_3, one would expect that the Raman spectrum of the LnX_2 species becomes weaker and that of LnX_3 gets stronger, as predicted by the starting compositions. The following chemical picture may explain this:

$$LnX_2 + X^- \rightarrow LnX_3 + e^-.$$
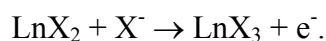
In such a scenario, it is not necessary that the molecular entities of the LnX_2 and LnX_3 species are distorted or disturbed. A reacting complex between LnX_2 and LnX_3 is not required since the electron itself may effectively move in conduction band tail states. Consequently the qualitative nature of both spectra should not be altered noticeably. On the other hand, the presence of F-centers and Drude electrons decreases the band intensities in the entire spectral range. This is due to their strong and broad absorption spectrum (Blanckenhagen 1999).

7.4.2. Mixed Valence States in Molten Salts: Two Site Small Polaron Model

A second prototypical defect scenario is the two site small polaron model. It is a well known defect state in solids like $Fe_3O_4 \left(= Fe^{2+}Fe_2^{3+}O_4\right)$ or $KFe^{2+}Fe^{3+}(CN)_6$. In a schematical description the excess electron experiences a double minimum potential. In the above examples the minima are situated at the two Fe-ions. Such a small polaron shows characteristic features with respect to the electronic transport and the optical absorption: it has a broad and asymmetric absorption band. The optical excitation energy (E_{Opt}) is connected to the activation energy (E_A) of the electronic conductivity according to $E_{Opt} = 4E_A$. This is the case if the double minimal potential curve is formed by two parabolic potential curves. For a further discussion about the small polaron model it is refered to Böttger and Bryksin (Böttger 1985).

The two site small polaron model was also suggested for mixed valence transition metals in molten salts (Stöhr 1999). Experimental evidence has been given by impedance spectroscopy, Wagner-Hebb polarization measurements and optical absorption spectroscopy.

In the sixties, Bredig (Bredig 1964) and Smirnov (Smirnov 1966) interestingly assumed independently a similar mechanismus for the liquid rare earth metal–rare earth halide system NdCl$_2$-NdCl$_3$. Very recently, this intervalence charge mechanismus was supported for NdX$_2$-NdX$_3$-(LiX-KX)$_{eu}$ solutions by electrical conductivity measurements and optical absorption spectroscopy (Terakado 2002, Terakado 2002a, Zein El Abedin 2002).

In the context of the present work, it is interesting to discuss the implication of this model for the microscopic structure and, accordingly, to the Raman spectra. In this sense, an important parameter is the life time of the excess electrons at an ionic site. If the hopping rate is considerably lower than the typical vibrational frequencies, the rare earth halide complexes in the melt have enough time to recover the equilibrium structure. In this case the reduced and the oxidized species should be visible in the spectra. On the other hand, a fast hopping rate compared to the time scale of the Raman experiment may result in distorted non-equilibrium structures of the complexes in the melt. These may differ from the equilibrium structures. Finally, on account of the broad and asymmetric polaron band, an overall reduction of the Raman spectra intensities should be expected.

7.4.3. NdCl₂-NdCl₃-(LiCl-KCl)ₑᵤ

The Raman spectra of liquid $(NdCl_3)_x$-$(NdCl_2)_y$-$(LiCl-KCl)_{eu, 1-x-y}$ samples are shown in Fig 5.10. The corresponding polarized and depolarized spectra can be found in the appendix A.3.5. It has to be noted that the concentration of $NdCl_3$ has been held constant: x=0.05 (spectra *a* to *f*). The concentration of $NdCl_2$ was increased from y=0 to y=0.05 in steps of 0.01. Fig 7.14 shows the analysis of the spectra in terms of the peak position, the half width and the integrated intensity.
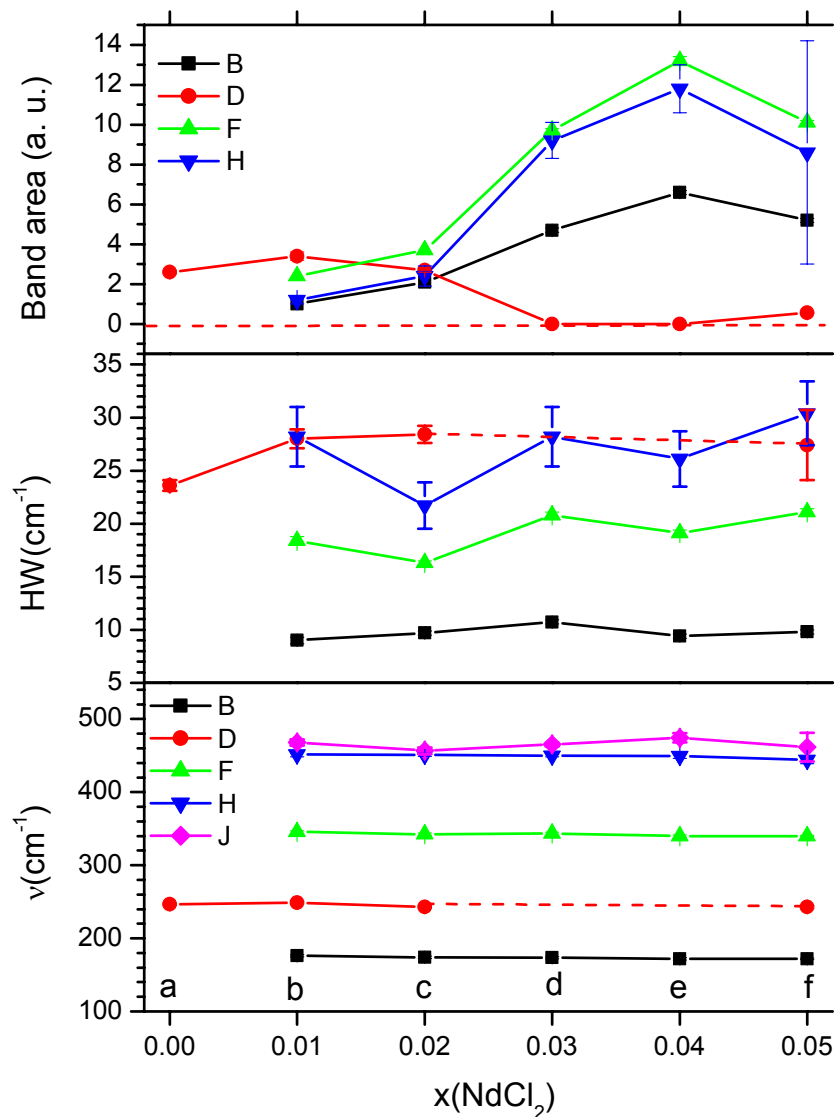
Figure 7.14: Composition effects on the NdCl₃-NdCl₂-(LiCl-KCl)ₑᵤ melts. Spectral analysis of Fig 5.10: ν= position of the band and HW = band width. *a*, *b*, *c*, *d*, *e*, and *f* correspond to the spectra of the mentioned figure.

The peak position of all analyzed bands of $NdCl_2$ and $NdCl_3$ is constant. The half width shows some scattering, just a bit outside of the error bars. So far, one can state that no new species appear in the spectra: there are neither new Raman bands, nor considerable shifts of the Raman bands. Since the recording conditions in this spectral series are the same, an interesting point is the decrease of the v_2 band (the polarized $NdCl_6^{3-}$ octahedra vibration) even though the concentration is kept constant. Other interesting observation is the increase of the $NdCl_2$-bands continuously with the composition up to a $NdCl_2$ concentration of y=0.04. This may answer the open question about the solubility of $NdCl_2$ in $NdCl_3$-$(LiCl$-$KCl)_{eu}$ melts. It is probable that $NdCl_2$ is homogenously dissolved in the melt. If $NdCl_2$ would stay solid it would be distributed inhomogenuosly in the sample. Then it would be highly unlikely to observe such a continuous increase of the Raman intensity.

It is more difficult to interpret the decrease of the $NdCl_3$-octahedra Raman band with increasing $NdCl_2$-concentration, and a final conclusion can not be given at the present status of the investigations. One idea considers a decreasing solubility of $NdCl_3$ with increasing $NdCl_2$ concentration in the eutectic melt. Again, this can only be proved if the phase behavior is studied thoroughly. Another approach considers a reaction of $NdCl_2$ with $NdCl_3$. However this is unlikely because we did not find traces of a reaction product in the Raman spectrum.

For mixtures of $NdCl_3$ and $NdCl_2$, as well as for NdI_2 and NdI_3 an intervalence charge transfer mechanisms was suggested from conductivity and optical absorption studies (Terakado 2002, Terakado 2002a, and Zein El Abedin 2002). It has been already suggested in section 7.4.2 for these defect states the posbility of estimate the average hopping rate of the electron and, respectively, the life time of the $NdCl_2$- and $NdCl_3$- species. For the excess electrons in NdI_3-NdI_2 Terakado (2002a) estimated a mobility of $\mu_e \approx 0.02$ cm^2/Vs. Assuming that this value is also valid for the chloride system, and using the equation of Einstein and Einstein-Smoluchovski, one can relate μ_e to an electron hopping frequency v_e as follows

$$v_e = \frac{2\mu_e RT}{ed_e^2} ,$$

where e is the elementary charge, R the gas constant and T the absolute temperature.

The hopping distance d_e could be estimated for our diluted system (roughly 10% of Nd-complexes in alkali halide eutectic) between 8 Å and 12 Å. From this, a hopping rate of 10^{11} Hz to $4 \cdot 10^{11}$ Hz is calculated. This is a factor of 10 to 100 slower than the typical

vibrational frequencies of the rare-earth halide species. Consequently, after a hopping process the reduced, as well the oxidized species, has time to restore its equilibrium structure. This would explain why we observe in our experiments the Raman bands of the pure $NdCl_2$- and $NdCl_3$- species simultaneously. Thus, the Raman spectra are in agreement with the two site polaron model as it was suggested by other experiments.

7.4.4. Ce-CeCl₃-(LiCl-KCl)$_{eu}$

In contrast to $NdCl_2$-$NdCl_3$-$(LiCl-KCl)_{eu}$ solutions, which show a noticeable qualitative change in the Raman spectra of liquid $NdCl_3$ with addition of $NdCl_2$, the equilibrium Raman spectra of Ce-$CeCl_3$-$(LiCl-KCl)_{eu}$ systems do not change qualitatively on doping with Ce (Fig 5.15). The ν_2 band, which is due to the octahedral species $CeCl_6^{3+}$, is still present. This spectral behavior does not exclude a mechanism for the electron localization on the basis of F-centers and /or Drude electrons. So far, no absorption spectra had been obtained already due to the strong corrosion of the window material (Terakado 2002). However, measurements of the apparent reflectivity, as the obtained by Terakado, indicate an increase of the absorption coefficient below 1.5 eV, which is in agreement with the Drude free electron behavior. This suggestion is also supported by electrical conductivity measurements of the Ce-$CeCl_3$ system (Bronstein 1962), which show an increasing very similar to alkali-alkali halide systems (a rate of approx. 5 times the value for the salt).

CeCl₂ in Ce-CeCl₃-(LiCl-KCl)$_{eu}$ Melts ?

As mentioned before, the qualitative development of the Raman spectra of liquid $CeCl_3$-$(LiCl-KCl)_{eu}$ solutions is not affected with increasing cerium; however, a prominent effect was observed during the dissolution process. Besides the octahedral band of the $CeCl_6^{3-}$ species at ~235 cm^{-1}, new Raman bands are present in the spectra of cell 3 at high concentrations of Ce in the melt ($y_{Ce} \geq 0.02$, Fig 5.18): ν_1, ν_3 and ν_4. These bands resemble closely the situation in $NdCl_2$-$NdCl_3$-$(LiCl-KCl)_{eu}$ (Figs 5.5 and 5.10).

On the other side, the bands ν_1, ν_3 and ν_4 in cell 3 depend on the doping of the system with metallic Ce. As we dope $CeCl_3$-$(LiCl-KCl)_{eu}$ with 0.5 mole percent Ce, we observe only

the melting process of the system with the time (see Fig 5.18). At a higher concentration of Ce (y_{Ce}=0.02) the new species which resemble the $NdCl_2$, form temporally. As can be seen at the right part of Fig 5.18, they disappear in a period of 3000 s; after this time only the octahedral vibration is visible.

Likely to $LaCl_2$, cerium dichloride is thermodynamically unstable at standard conditions (Mellors 1959). However, Smirnov and Lbov (Smirnov 1965) reported that $CeCl_2$ is stable in mixtures of Ce and $CeCl_3$ at Ce concentrations above 9.3% mole in the melt. The available Raman spectroscopic results give evidence that also in LiCl-KCl melts the Ce^{2+} species may exist at least for an intermediate period. Its structure is probably closely related to $NdCl_2$. In such a manner, the clearly low stability of the Ce^{2+} species provides an elucidation for the strong concentration dependence of the conductivity in Ce-$CeCl_3$ compared with the Nd-$NdCl_3$ system, i.e. less stable "electron-traps" are available in the Ce-system. On doping with Ce the free electrons are less strongly localized and contribute to a more effective electronic transport.

7.4.5. CeI_2-CeI_3-(LiI-KI)$_{eu}$

The Raman spectra of the CeI_3-CeI_2 system dissolved in a LiI-KI eutectic solution are presented in Fig 6.11. The HV and VV spectra can be found in the Appendix A.5.5. The CeI_3-(LiI-KI)$_{eu}$ shows the well known band ν_2, which is attributed to the polarized mode of the octahedral CeI_6^{3-} species. With the addition of CeI_2 it looks as if a new band ν_1 around 75 cm^{-1} appears. This feature is so close to the notch filter edge that can not be unambiguously attributed to a new band. Instead, it could also be caused from a broadened Rayleigh band. Unlikely to $NdCl_3$-$NdCl_2$-(LiCl-KCl)$_{eu}$, the present system does not undergo a clear visible qualitative change in the spectra. From his absorption experiments Terakado (Terakado 2002) discusses the possibility of formation of I_3^- species in CeI_3-CeI_2-(LiI-KI)$_{eu}$ solutions. However, the typical Raman bands of I_3^- at 110 cm^{-1} and 160 cm^{-1} (Loos 1974, Child 1983) are not visible in our system. Only the intensity of the polarized octahedra band drops with increasing CeI_2 concentration. One possible explanation for this is the presence of species which absorb the exciting laser radiation and the emitted Raman spectrum. F-center-like or polaron states, as well as mobile Drude electrons, could account for this.

Appendix

A1. Phase Diagrams and Literature Data of Selected Compounds

A.1.1. Nd-NdCl$_3$ (Bredig 1964)
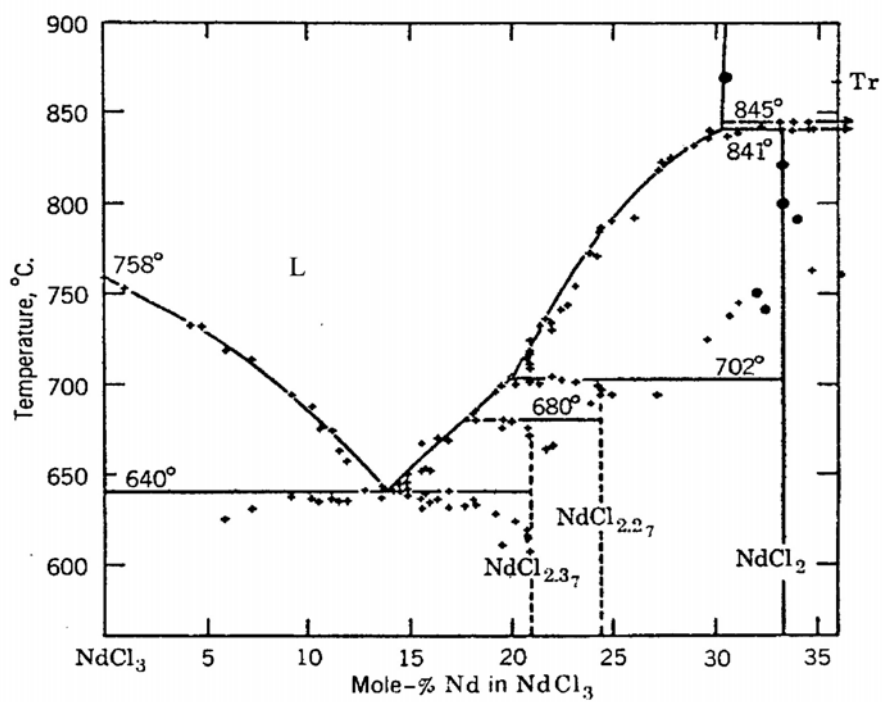
A.1.2. **NdCl₃-LiCl-KCl** (Nakamura 1997)
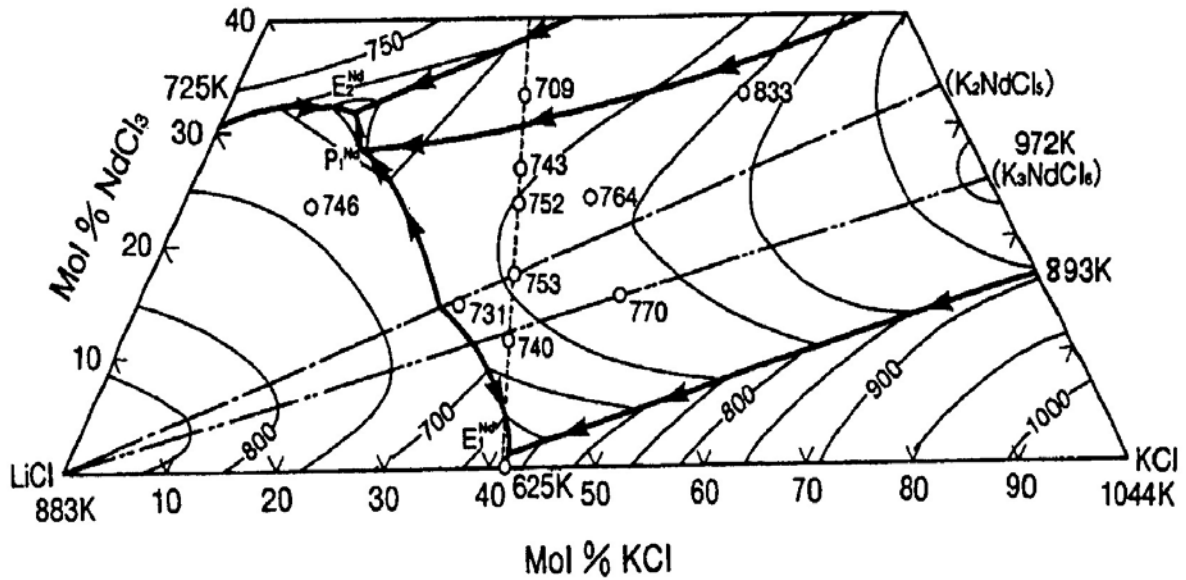
A.1.3. CeCl₃-(LiCl-KCl)ₑᵤ*   NdCl₃-(LiCl-KCl)ₑᵤ*
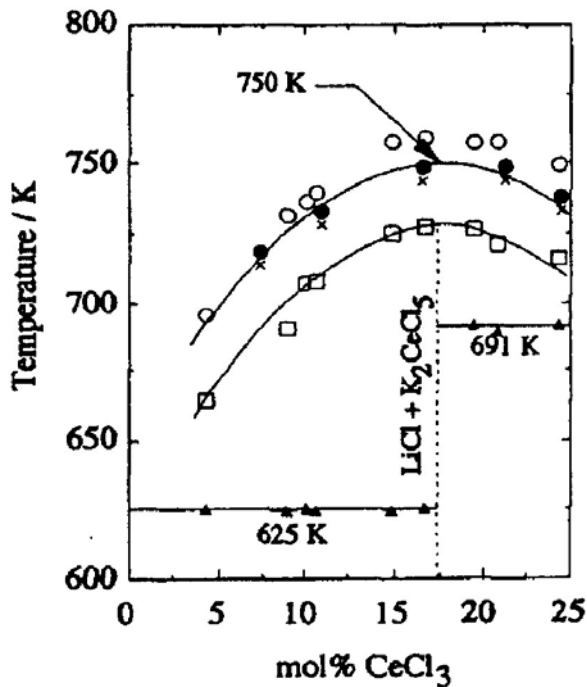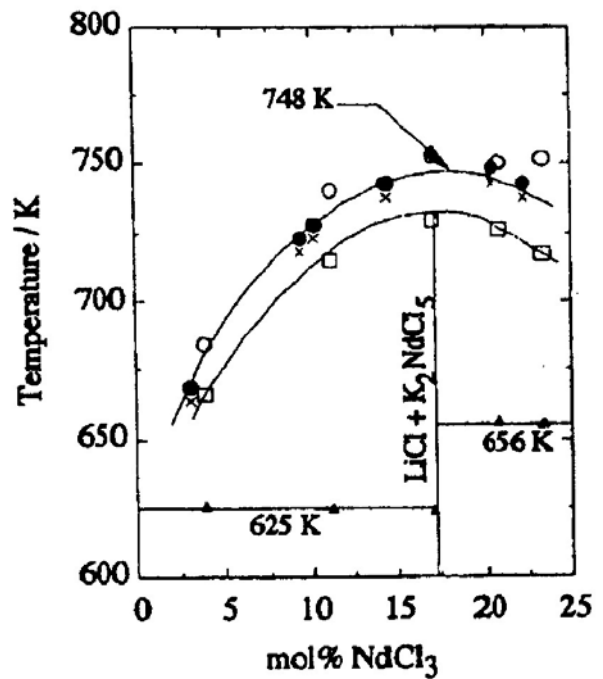
* The symbols ▲, □ and ○ indicate three types of transitions determined by thermal analysis and the symbols ● and × indicate liquid and two-phase regions determined by visual observations (Nakamura 1997).

A.1.4. Ce-CeCl₃ (Mellors 1959)
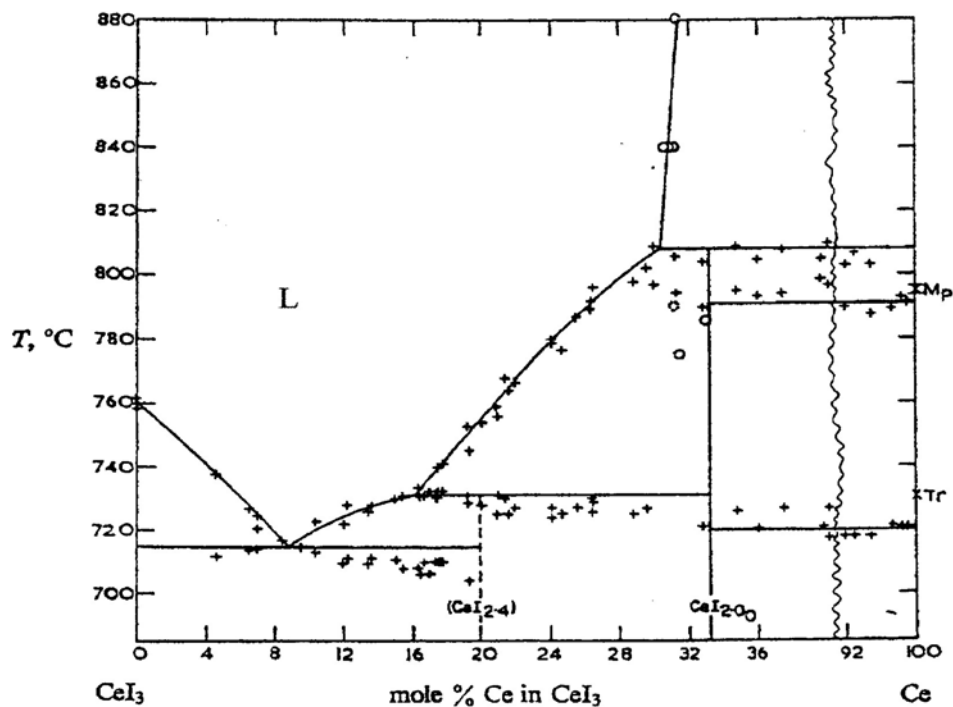
A.1.5. Nd-NdI₃ (Bredig 1964)
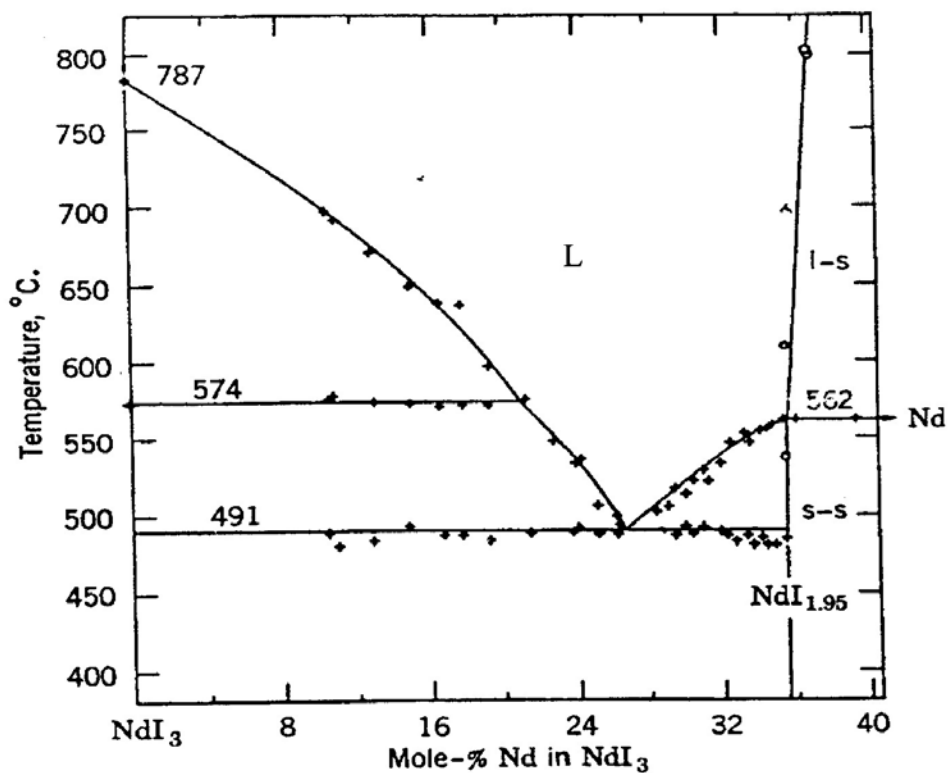
A.1.6. Ce-CeI$_3$ (Corbett 1961)
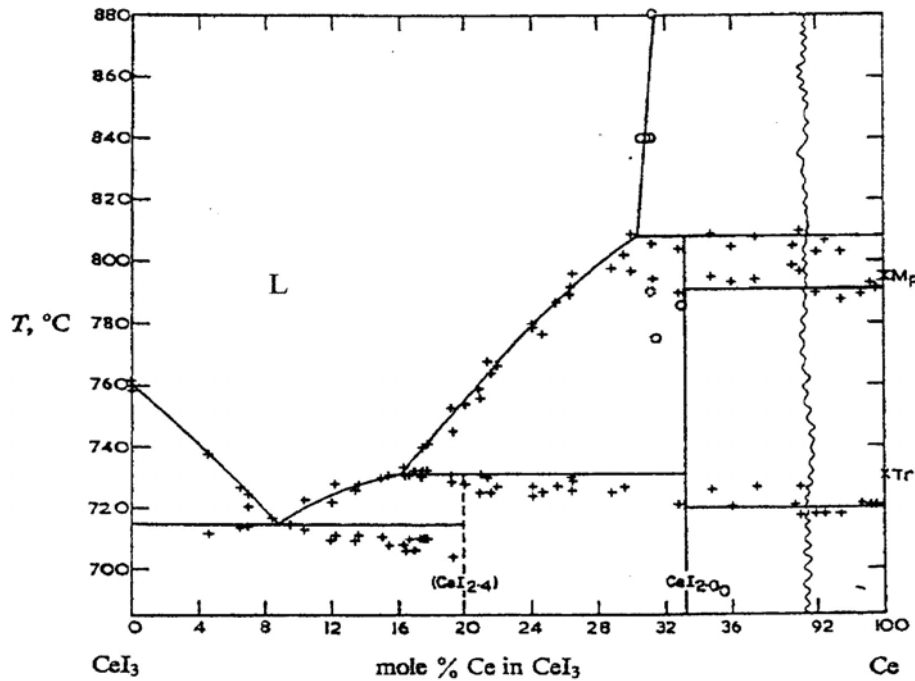
A.1.7. Literature Data

Janz 1967

(LiCl-KCl)$_{eu}$	$x_{KCl} = 0.415$
(LiI-KI)$_{eu}$	$x_{KI} = 0.369$

Melting Point (Janz 1967)

(LiCl-KCl)$_{eu}$	$T_m = 361°C$
(LiI-KI)$_{eu}$	$T_m = 260°C$

For rare earth halides see the corresponding phase diagrams.

Density ρ of the melts: $[\rho] = g/cm^3$ $[T] = °C$

NdCl$_3$	$3.751 - 0.000663 \cdot T$	(Gmelin 1982)
CeCl$_3$	$4.248 - 0.000925 \cdot T$	(Janz 1967)
NdI3	$5.1146 - 0.0010701 \cdot T$	(Kutscher 974)
(LiCl-KCl)$_{eu}$	$1.8781 - 0.0005332 \cdot T$	(Smirnov 1982)
(LiI-KI)$_{eu}$	$3.0951 - 0.000816 \cdot T$	(Janz 1977)

Electron Affinity (CRC 1997)

Cl^- 3.612 eV
I^- 3.059 eV

Ionization Energy (CRC 1997)

	I	II	III
Nd	5.5250 eV	10.73 eV	22.1 eV
Ce	5.5387 eV	10.85 eV	20.198 eV

Standard Enthalpy of Formation: ΔH_f^0 (Bratsch 1982, Cordfunke 2001, Kim 1979)

Chlorides

$NdCl_2{}^*$	-693 kJ/mol
$NdCl_3$	-1040.9 ± 1.0 kJ/mol
$CeCl_2{}^*$	-555 kJ/mol
$CeCl_3$	-1059 ± 1.0 kJ/mol

Iodides

$NdI_2{}^*$	-294 kJ/mol
NdI_3	-639.2 ± 4.0 kJ/mol
$CeI_2{}^*$	-294 kJ/mol
CeI_3	-666.8 ± 3.0 kJ/mol

The values of dihalides were calculated from the corresponding Born-Haber cycles (see also Johnson 1969, Struck 1991).

Appendix A2. Raman Spectra of the Alkali Halide Eutectic Mixtures.

A.2.1. Raman Spectrum of Liquid (LiCl-KCl)$_{eu}$ in Cell 2
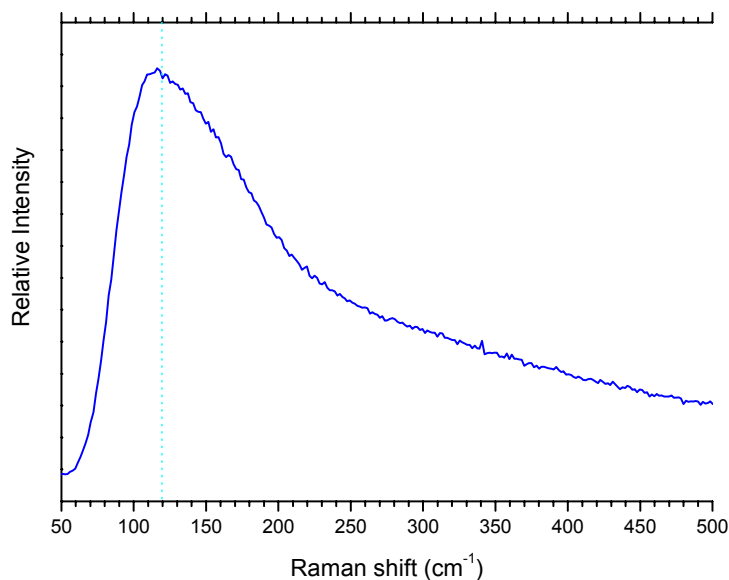
A.2.2. Raman Spectrum of Liquid (LiI-KI)$_{eu}$ in Cell 1
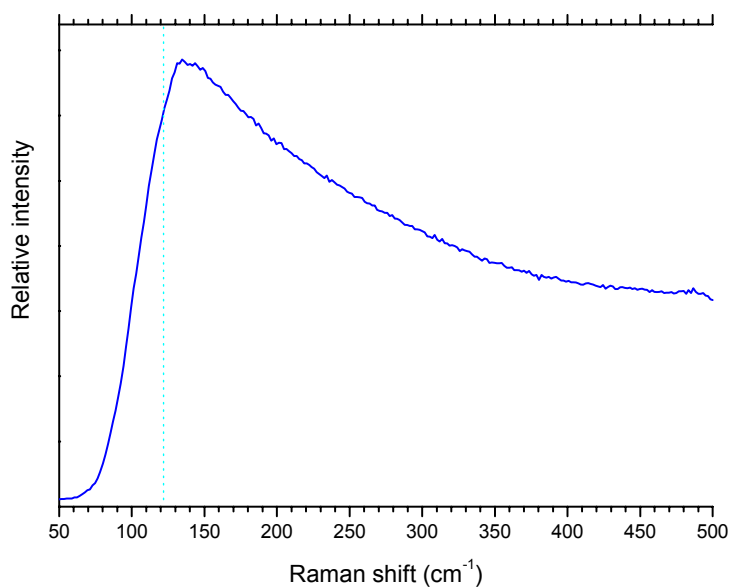
The Raman spectra were recorded at 500°C without polarizer, using a He-Ne laser (λ_0=632.8 nm), a 6.59° notch filter angle and a recording time of 30 s. The dashed line indicates the limit of the notch filter (120cm^{-1}).

A3. Raman Spectra of $(NdCl_3)_x$-$(NdCl_2)_y$–$(LiCl-KCl)_{eu, 1-x-y}$ Melts.

The Raman spectra presented in this Appendix were recorded under the following conditions: He-Ne laser (λ_0=632.8 nm), 6.59° notch filter angle and without polarizer.

A.3.1. Solid NdCl$_3$ in Cell 1.
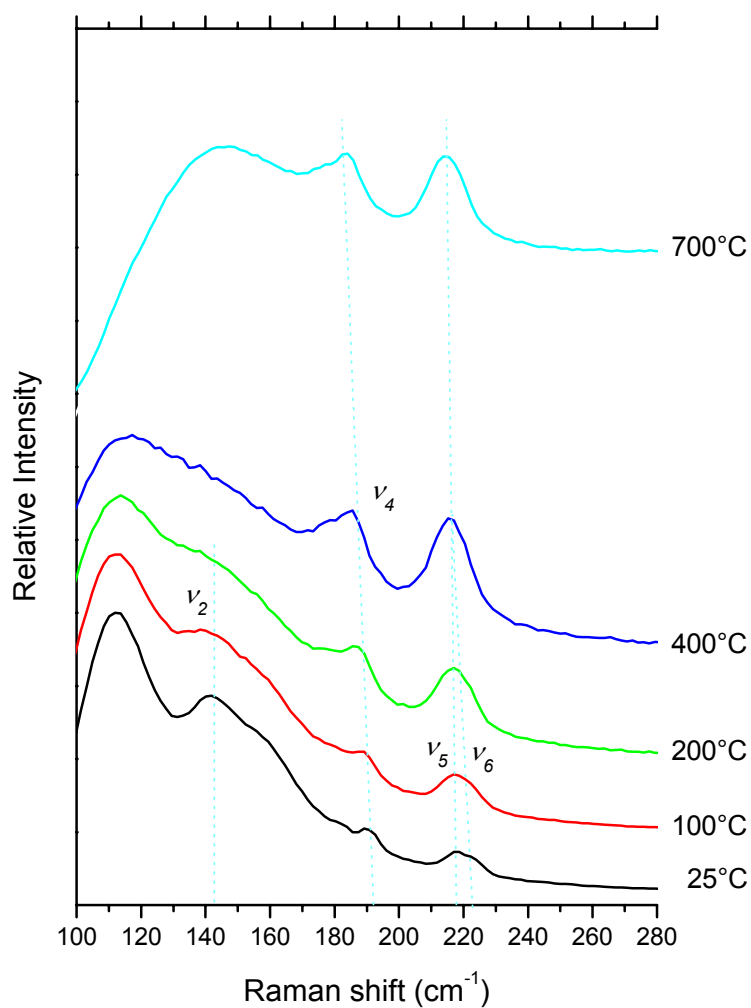
A.3.2. $(NdCl_3)_{0.10}$-$(LiCl\text{-}KCl)_{eu,\,0.90}$ in Cell 2 with Mo-Crucible
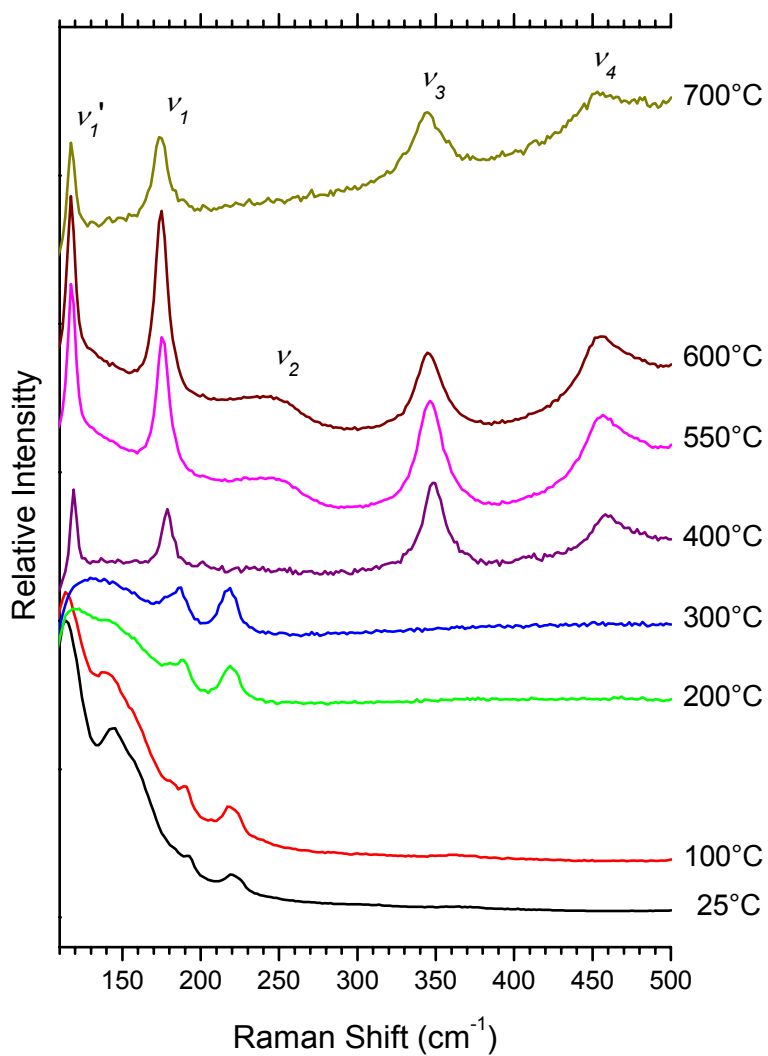
A.3.3. $(NdCl_3)_{0.10}$-$(LiCl\text{-}KCl)_{eu, 0.90}$ in Cell 2 with Glassy Carbon-Crucible
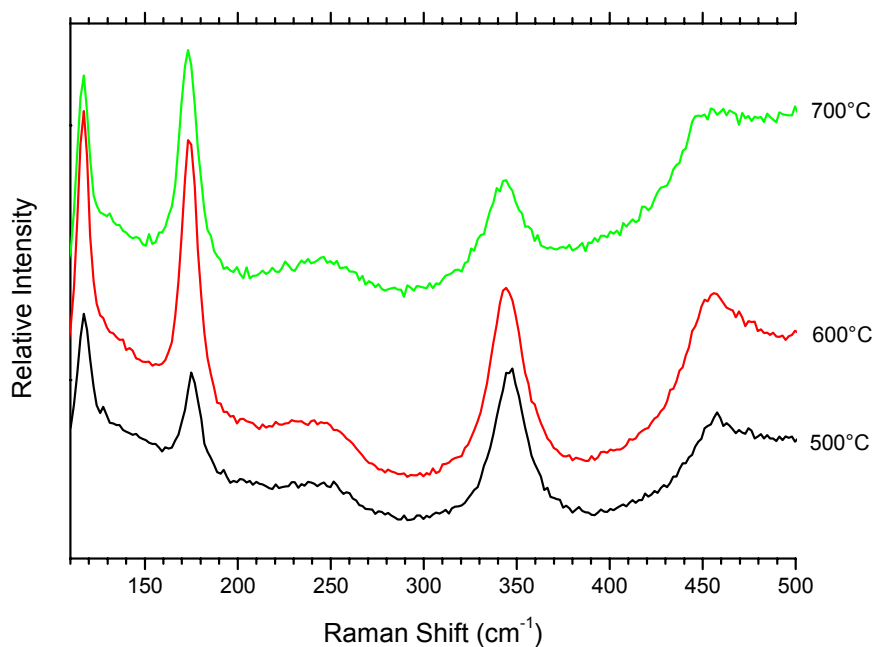
A.3.4. $(NdCl_3)_{0.05}$-$(LiCl\text{-}KCl)_{eu, 0.95}$ in Cell 3 (homogenized in a preliminary heating cycle).
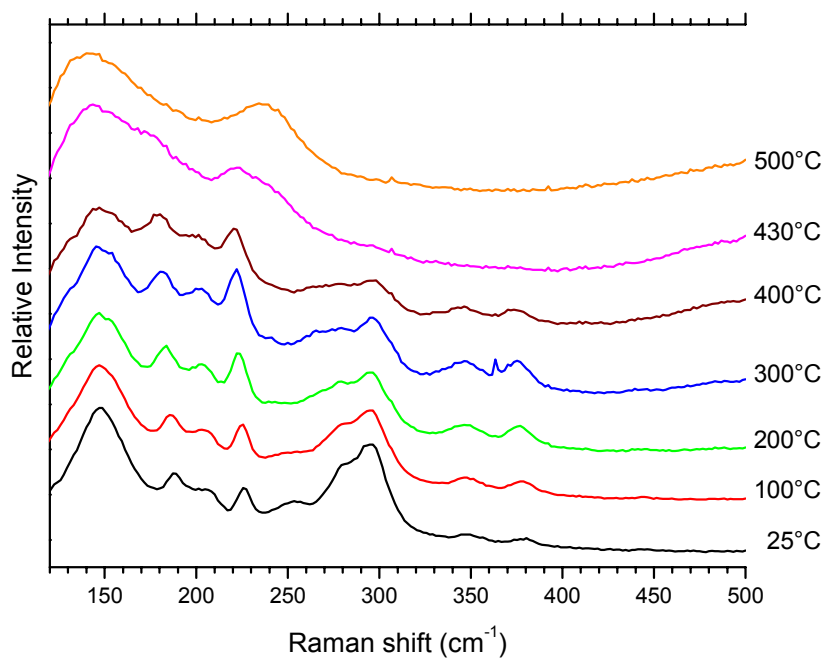
A.3.5. (NdCl$_3$)$_x$-(NdCl$_2$)$_y$-(LiCl-KCl)$_{eu, 1-x-y}$ Melts in Cell 3.

a) (NdCl$_3$)$_{0.05}$-(LiCl-KCl)$_{eu, 0.95}$ at 450°C.
b) (NdCl$_3$)$_{0.05}$-(NdCl$_2$)$_{0.01}$-(LiCl-KCl)$_{eu, 0.94}$ at 500°C.
c) (NdCl$_3$)$_{0.05}$-(NdCl$_2$)$_{0.02}$-(LiCl-KCl)$_{eu, 0.93}$ at 500°C.
d) (NdCl$_3$)$_{0.05}$-(NdCl$_2$)$_{0.03}$-(LiCl-KCl)$_{eu, 0.92}$ at 530°C.
e) (NdCl$_3$)$_{0.05}$-(NdCl$_2$)$_{0.04}$-(LiCl-KCl)$_{eu, 0.91}$ at 600°C.
f) (NdCl$_3$)$_{0.05}$-(NdCl$_2$)$_{0.05}$-(LiCl-KCl)$_{eu, 0.90}$ at 600°C.
g) (NdCl$_2$)$_{0.05}$-(LiCl-KCl)$_{eu, 0.95}$ at 600°C.

A.3.6. $(NdCl_3)_{0.05}$-$(NdCl_2)_{0.01}$-$(LiCl\text{-}KCl)_{eu,\ 0.94}$ in Cell 3 (homogenized in a preliminary heating cycle).
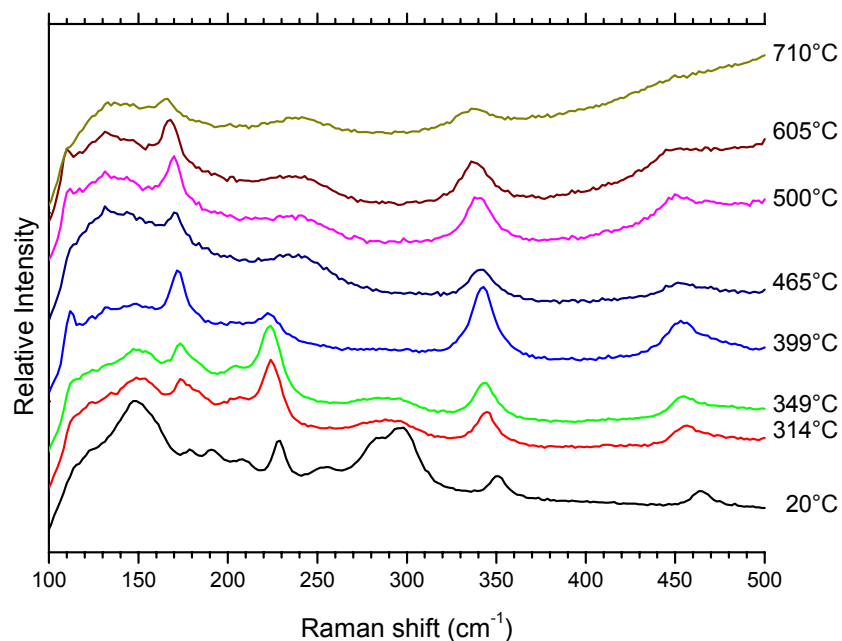
A.3.7. $(NdCl_3)_{0.05}$-$(NdCl_2)_{0.05}$-$(LiCl\text{-}KCl)_{eu,\ 0.90}$ at 600°C in Cell 3 (homogenized in a preliminary heating cycle).
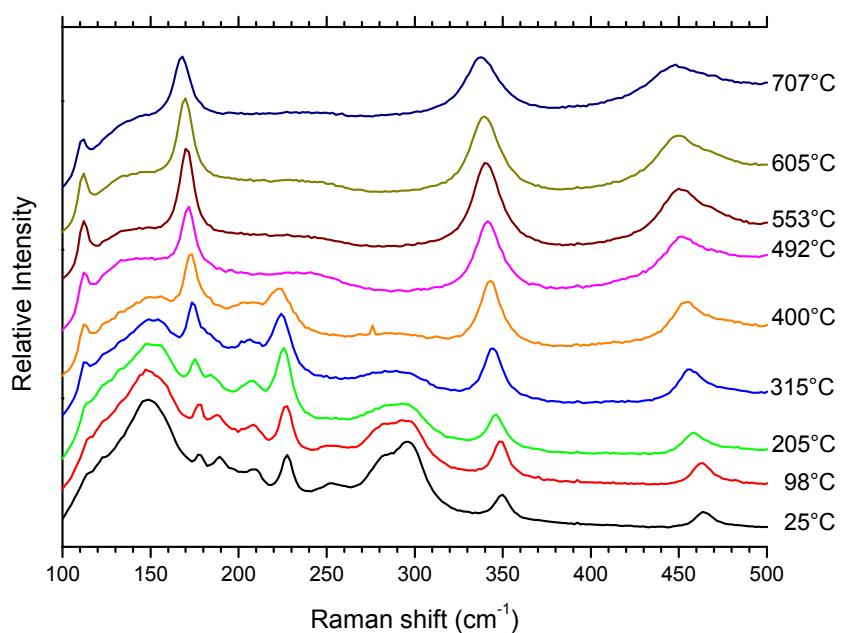
A4. Raman spectra of $(CeCl_3)_x$-$(Ce)_y$–$(LiCl\text{-}KCl)_{eu,\ 1\text{-}x\text{-}y}$ melts.

The following Raman spectra were recorded without polarizer, 120 s of integration time, λ_0=632.8 nm and a notch filter angle of 6.59°.

A.4.1. Surface of Ce metal at 25°C.
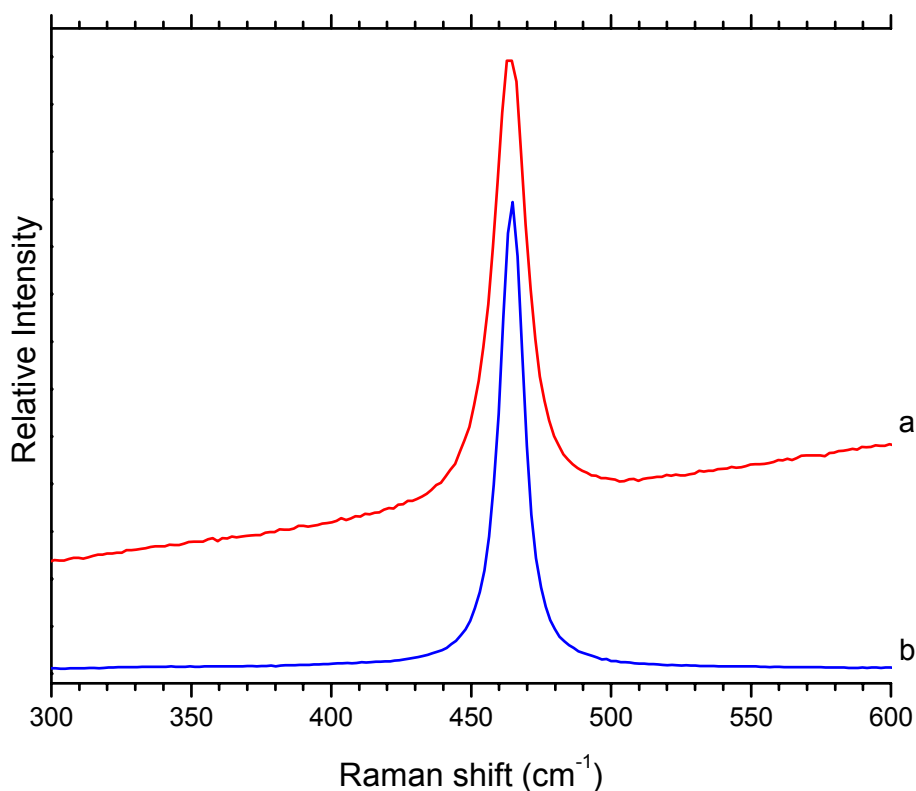
(a) The spectrum was recorded with an achromatic lens with 50 mm focal length.
(b) The spectrum was recorded with the 50x microscope's objective.

A.4.2. CeCl$_3$ in Cell 1.
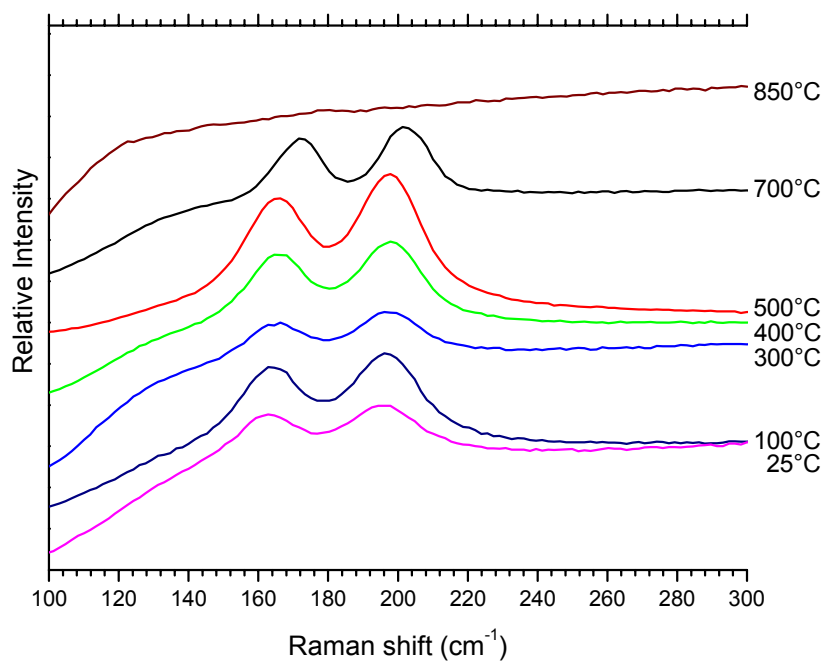
A.4.3. (CeCl$_3$)$_{0.25}$-(LiCl-KCl)$_{eu, 0.75}$ in Cell 3.
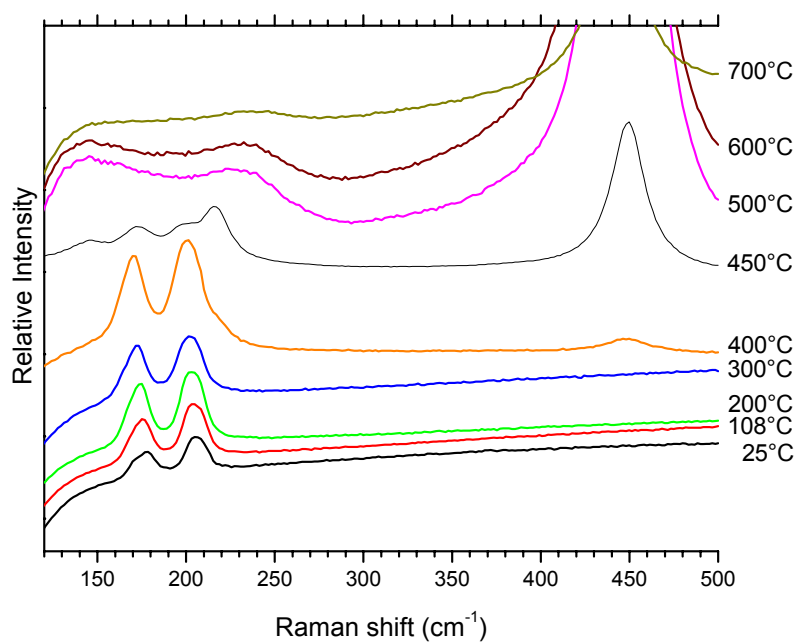
A.4.4. (CeCl$_3$)$_{0.25}$-(LiCl-KCl)$_{eu, 0.75}$ at 450°C in Cell 3.
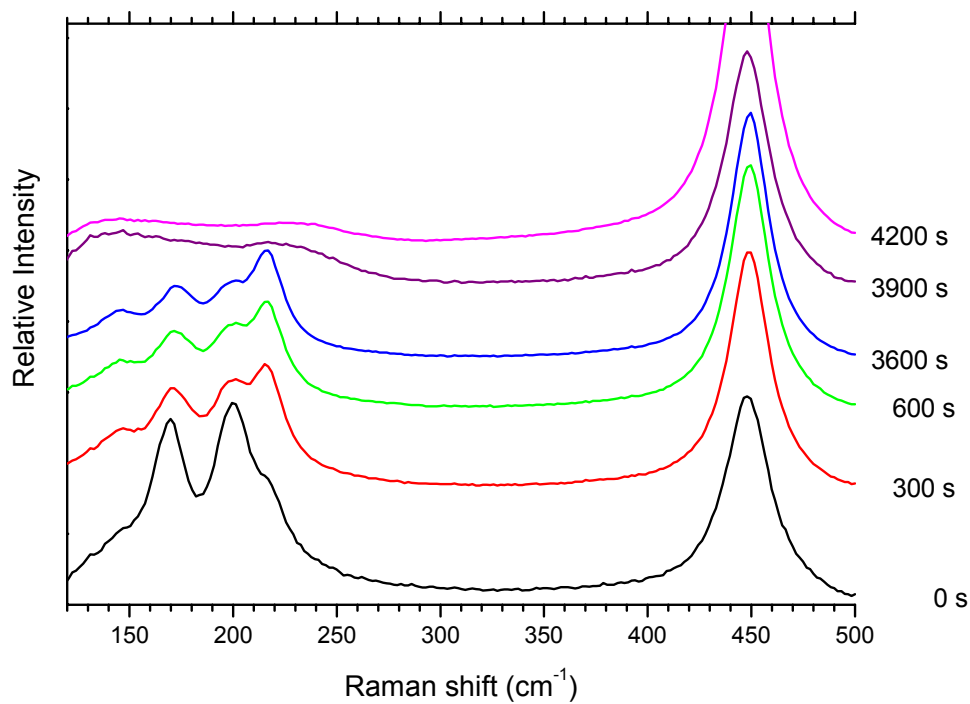
A.4.5. (CeCl$_3$)$_{0.20}$-(Ce)$_{0.02}$-(LiCl-KCl)$_{eu, 0.78}$ in Cell 3.
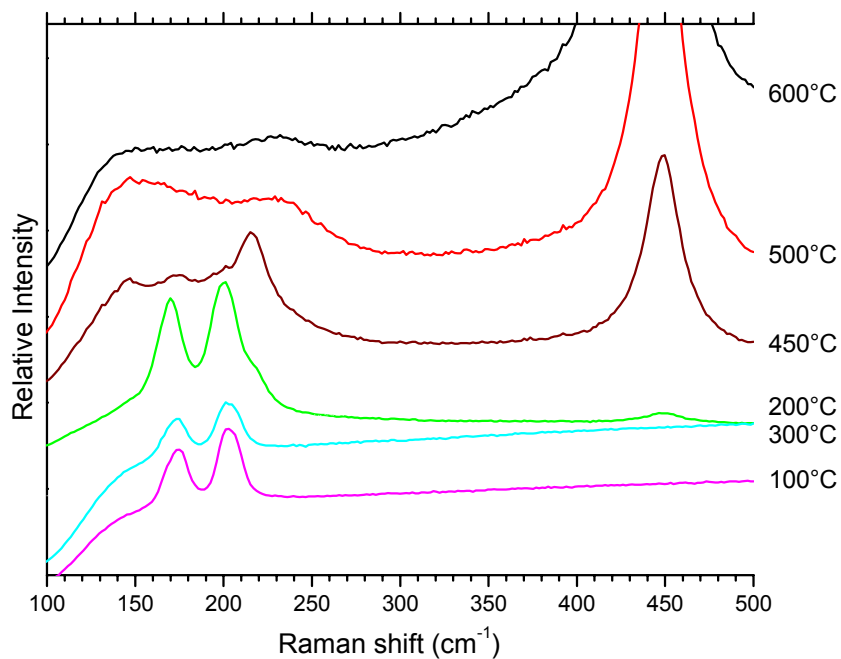
A5. Raman spectra of $(CeI_3)_x$-$(CeI_2)_y$–$(LiI\text{-}KI)_{eu,\ 1\text{-}x\text{-}y}$ melts.

A.5.1. Raman spectra of liquid $(CeI_3)_x$-$(CeI_2)_y$-$(LiI\text{-}KI)_{eu,\ 1\text{-}x\text{-}y}$ mixtures in cell 1. The spectra were recorded without polarizer, 60 s of integration time, λ_0=632.8 nm and a notch filter angle of 6.59°.
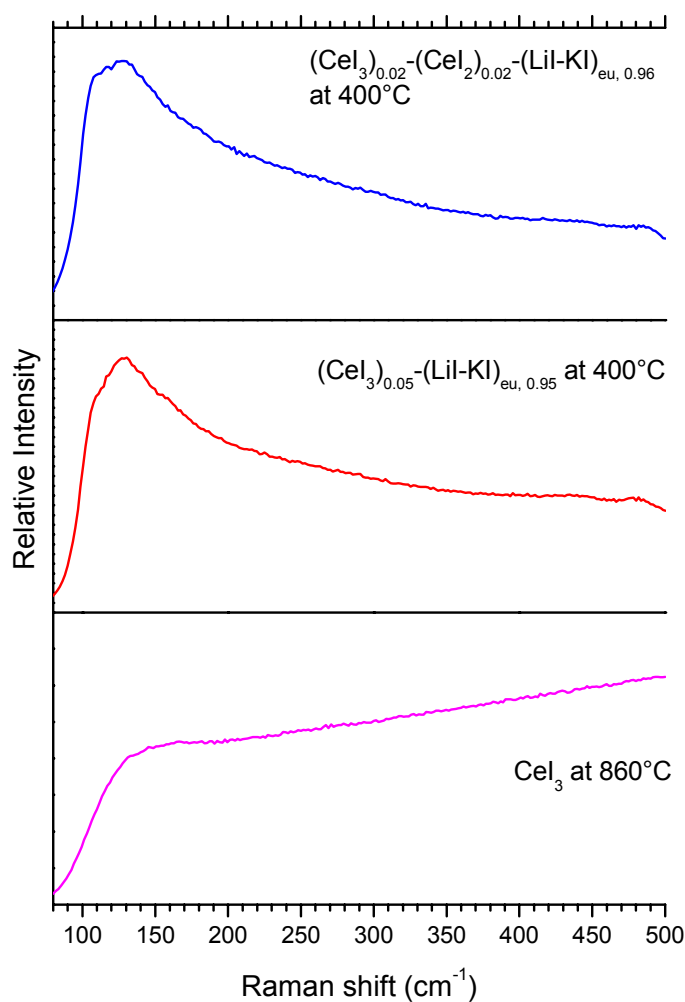
The following Raman spectra of $(CeI_3)_x$-$(CeI_2)_y$-$(LiI-KI)_{eu,\ 1-x-y}$ mixtures in cell 1 were recorded for the liquid and solid mixtures, with and without polarizer respectively, 300 s of integration time, λ_0=514.5 nm and a notch filter angle of 4.05°.

A.5.2. Liquid $(CeI_3)_x$-$(CeI_2)_y$ at 800°C
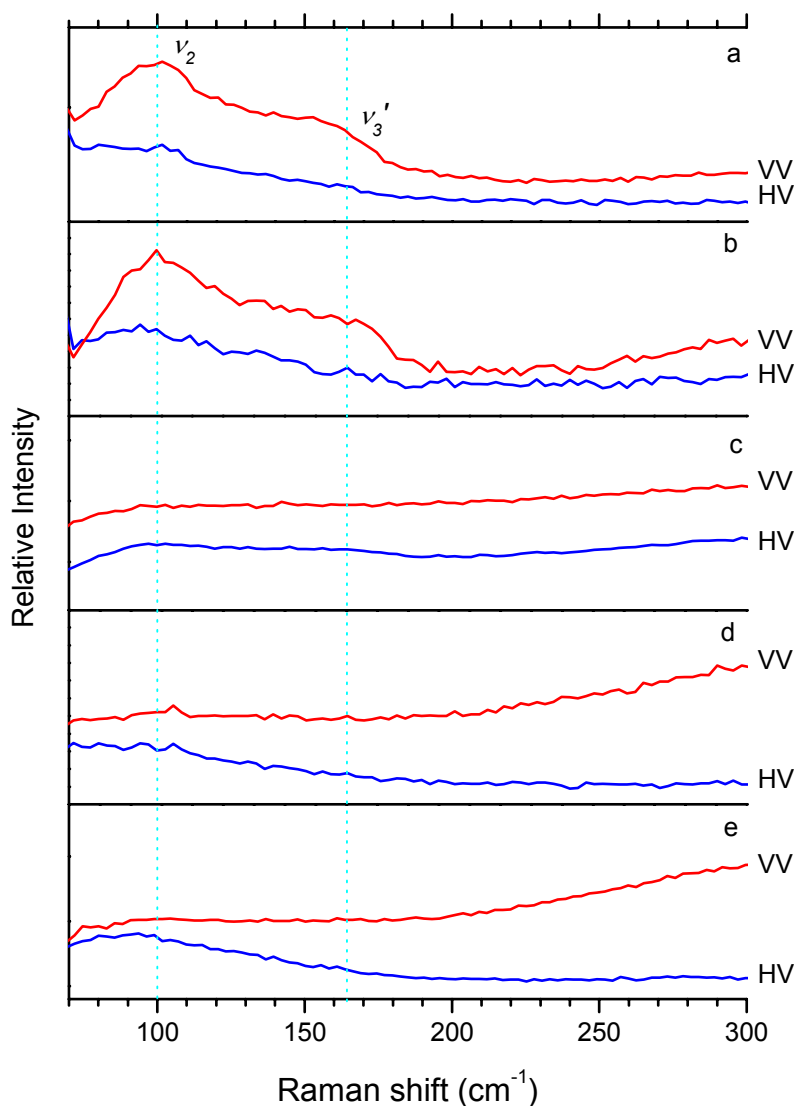
a) CeI_3

b) $(CeI_3)_{0.94}$-$(CeI_2)_{0.06}$

c) $(CeI_3)_{0.76}$-$(CeI_2)_{0.24}$

d) $(CeI_3)_{0.5}$-$(CeI_2)_{0.5}$

e) CeI_2

A.5.3. $(CeI_3)_{0.94}$-$(CeI_2)_{0.06}$
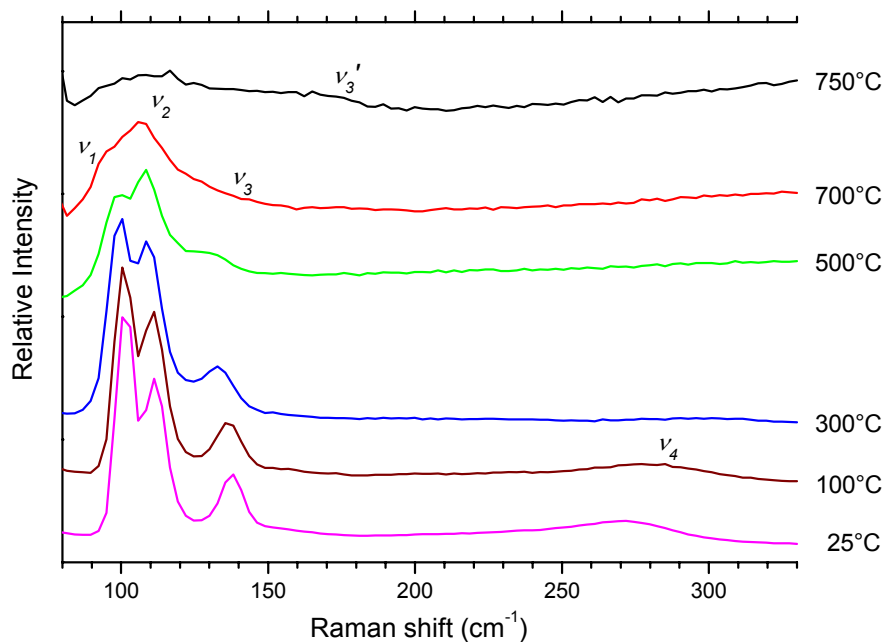
A.5.4. $(CeI_3)_{0.76}$-$(CeI_2)_{0.24}$
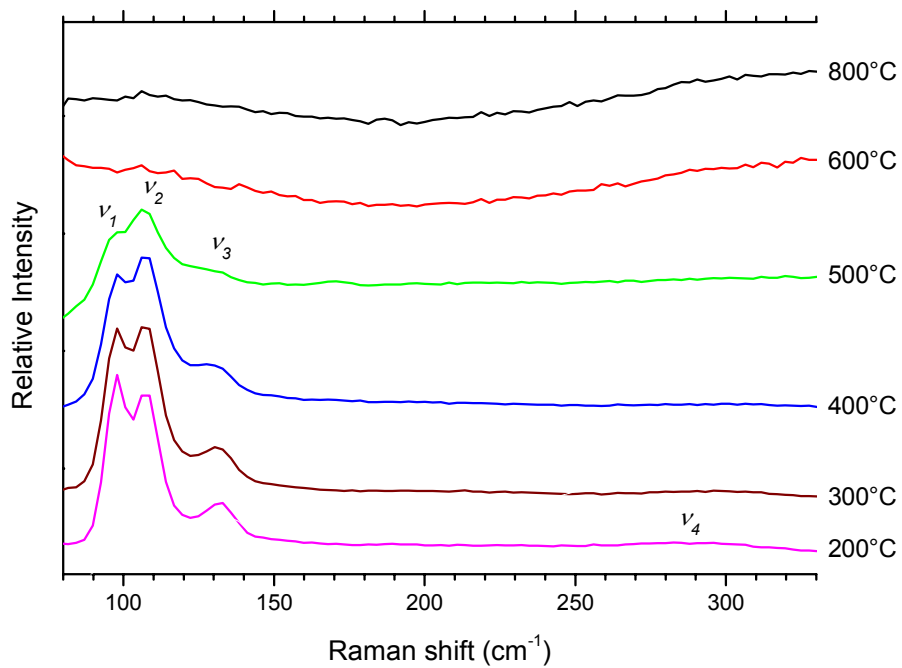
A.5.5. Liquid $(CeI_3)_x$-$(CeI_2)_y$-$(LiI$-$KI)_{eu, 1-x-y}$ at 500°C
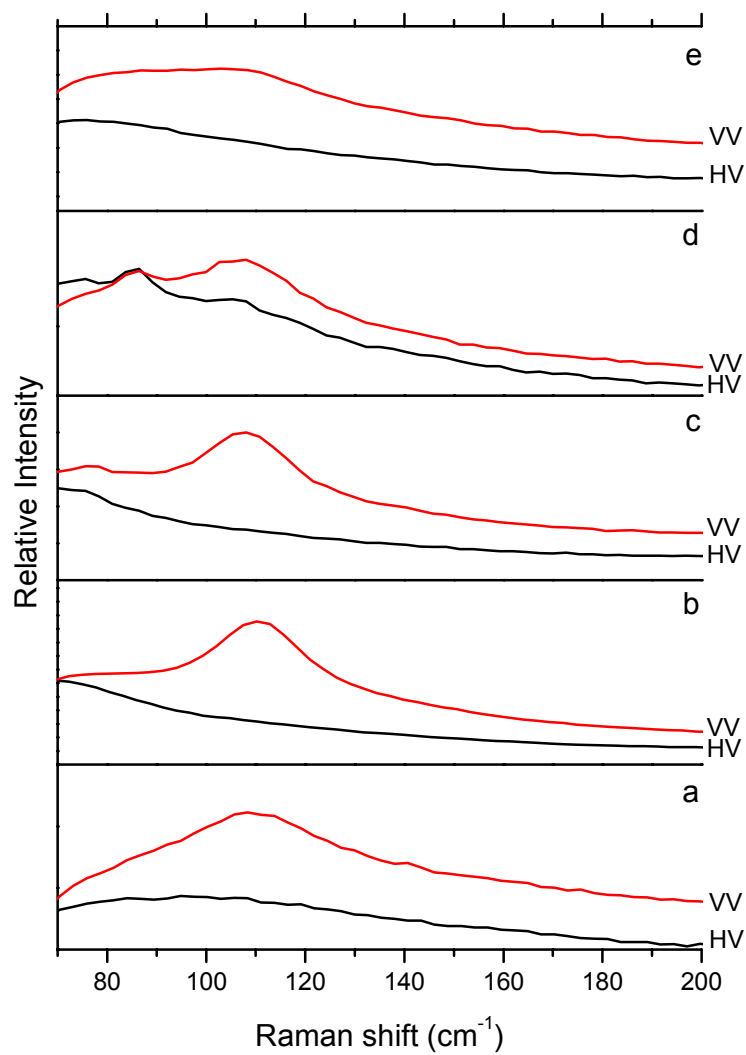
a) $(CeI_3)_{0.05}$-$(LiI$-$KI)_{eu, 0.95}$.

b) $(CeI_3)_{0.094}$-$(CeI_2)_{0.006}$-$(LiI$-$KI)_{eu, 0.90}$.

c) $(CeI_3)_{0.076}$-$(CeI_2)_{0.024}$-$(LiI$-$KI)_{eu, 0.90}$.

d) $(CeI_3)_{0.05}$-$(CeI_2)_{0.05}$-$(LiI$-$KI)_{eu, 0.90}$.

e) $(CeI_2)_{0.02}$-$(LiI$-$KI)_{eu, 0.98}$.

A.5.6. $(CeI_3)_{0.094}$-$(CeI_2)_{0.006}$-$(LiI-KI)_{eu, 0.90}$
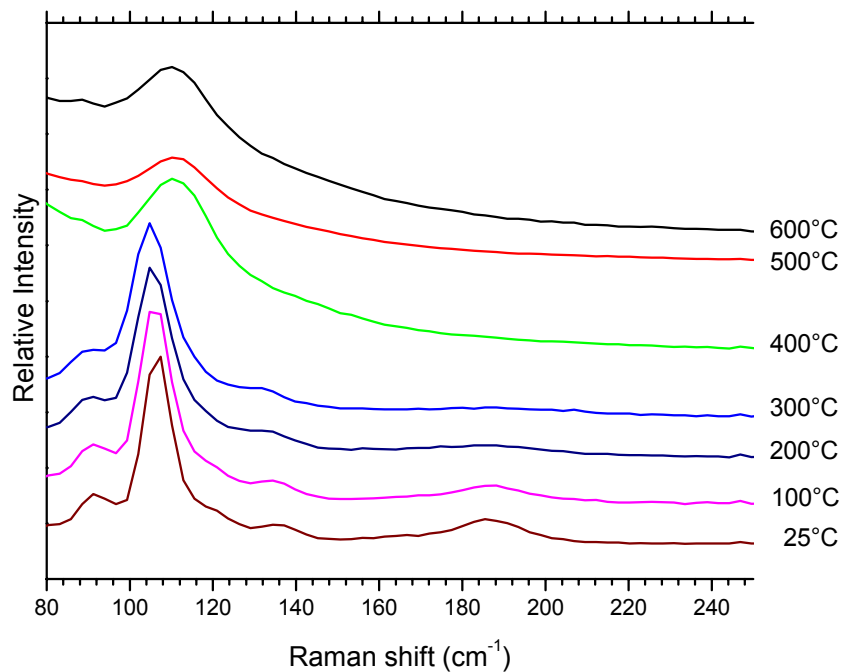
A.5.7. $(CeI_3)_{0.076}$-$(CeI_2)_{0.024}$-$(LiI-KI)_{eu, 0.90}$
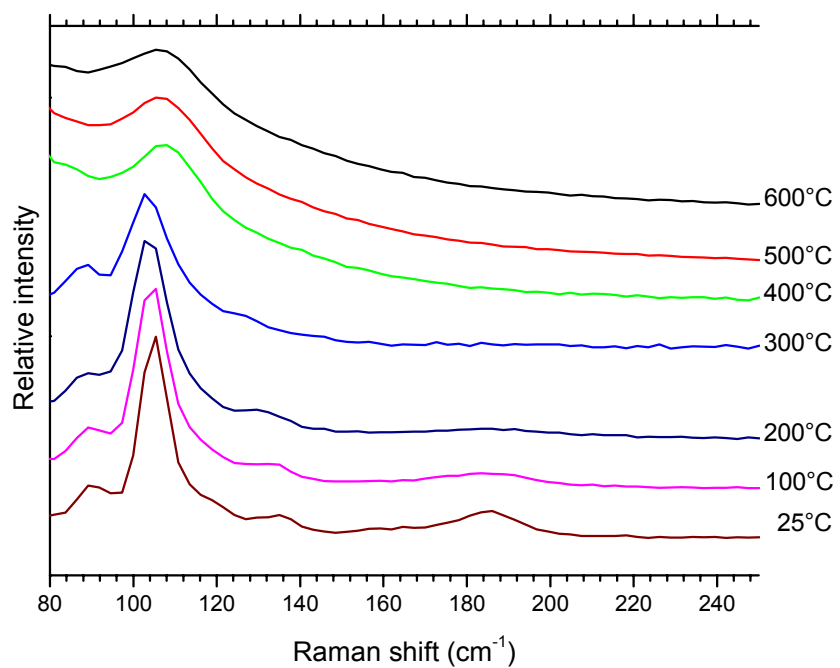
A.5.8. $(CeI_3)_{0.05}$-$(CeI_2)_{0.05}$-$(LiI\text{-}KI)_{eu,\ 0.90}$.
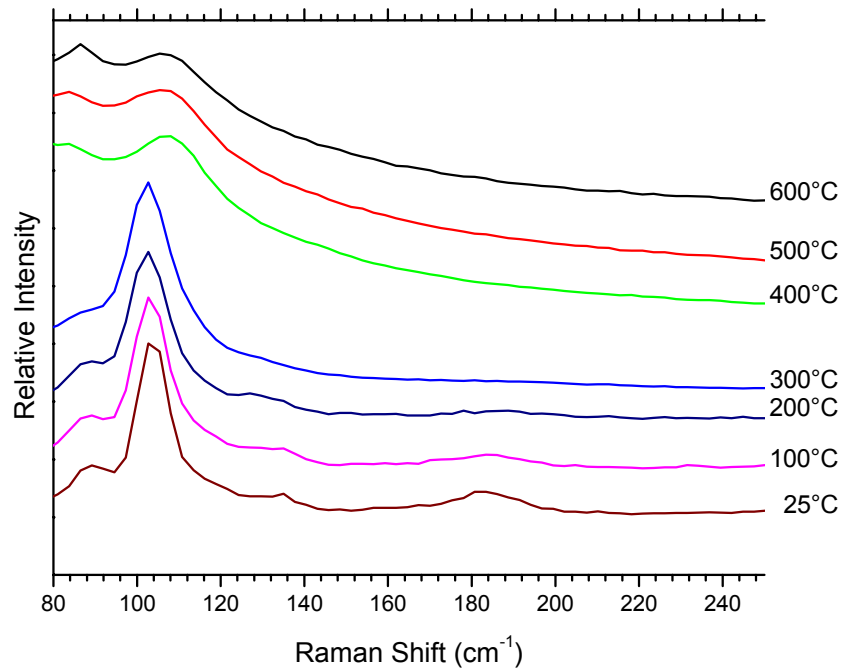
A6. Raman Spectra of $(NdI_3)_x$-$(NdI_2)_y$–$(LiI\text{-}KI)_{eu,\ 1\text{-}x\text{-}y}$ Melts.

The following Raman spectra of $(NdI_3)_x$-$(NdI_2)_y$-$(LiI\text{-}KI)_{eu,\ 1\text{-}x\text{-}y}$ mixtures in cell 1 were recorded for the liquid and solid mixtures with and without polarizer respectively, 200 to 300 s of integration time, λ_0=514.5 nm and a notch filter angle of 4.05°.

A.6.1. Liquid $(NdI_3)_x$-$(NdI_2)_y$ at 800°C
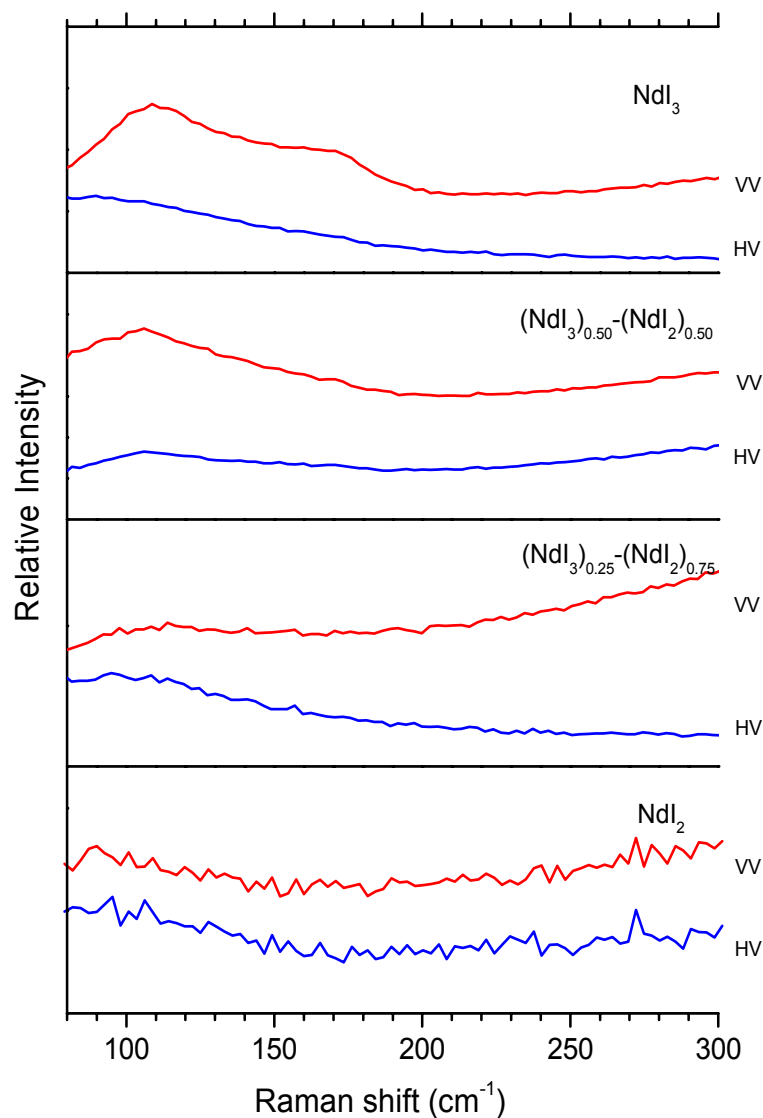
A.6.2. $(NdI_3)_{0.75}$-$(NdI_2)_{0.25}$
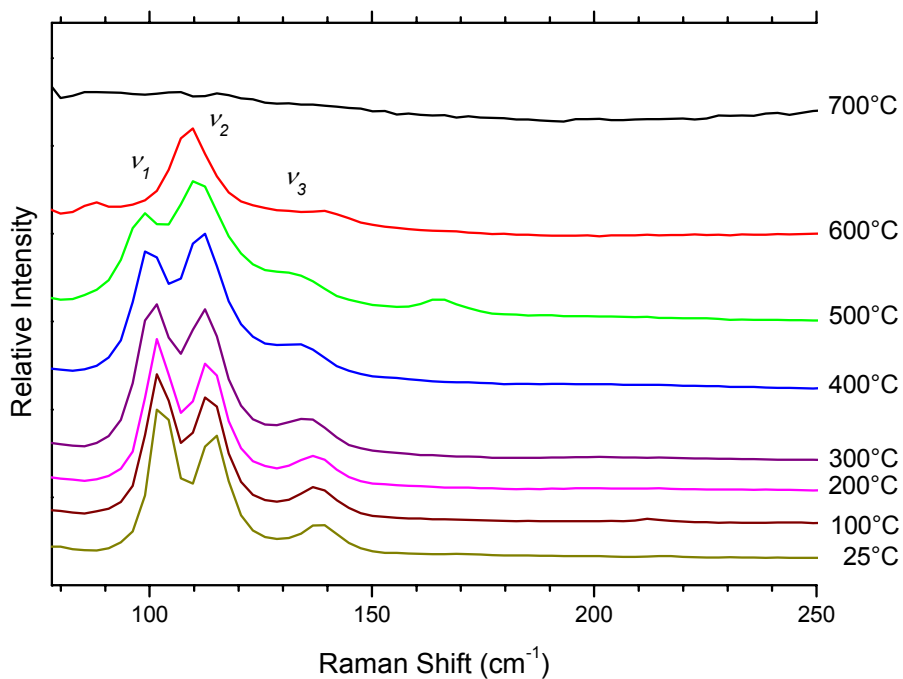
A.6.3. $(NdI_3)_{0.50}$-$(NdI_2)_{0.50}$
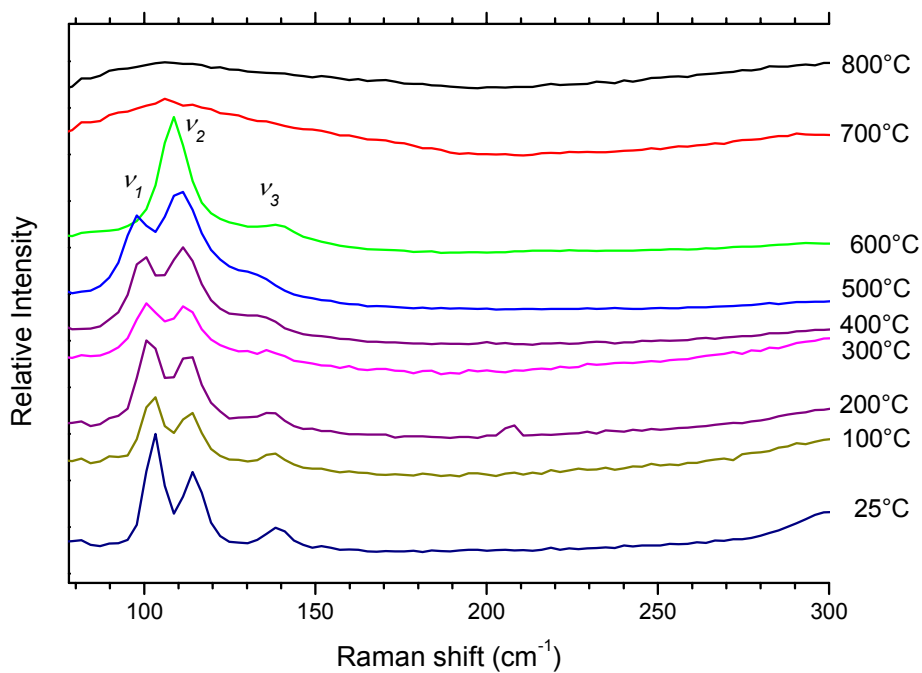
A.6.4. $(NdI_3)_{0.25}$-$(NdI_2)_{0.75}$
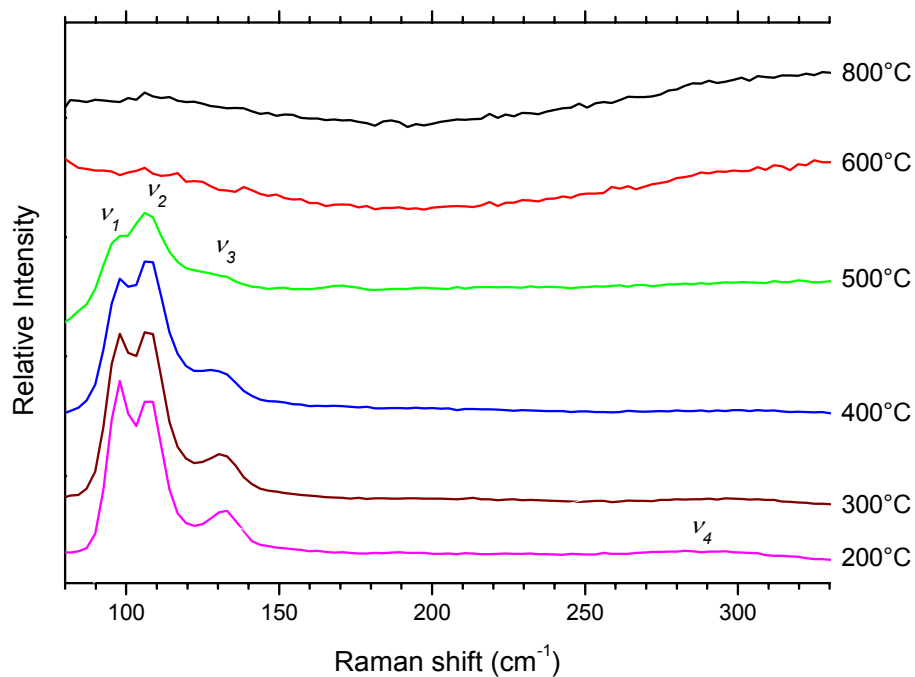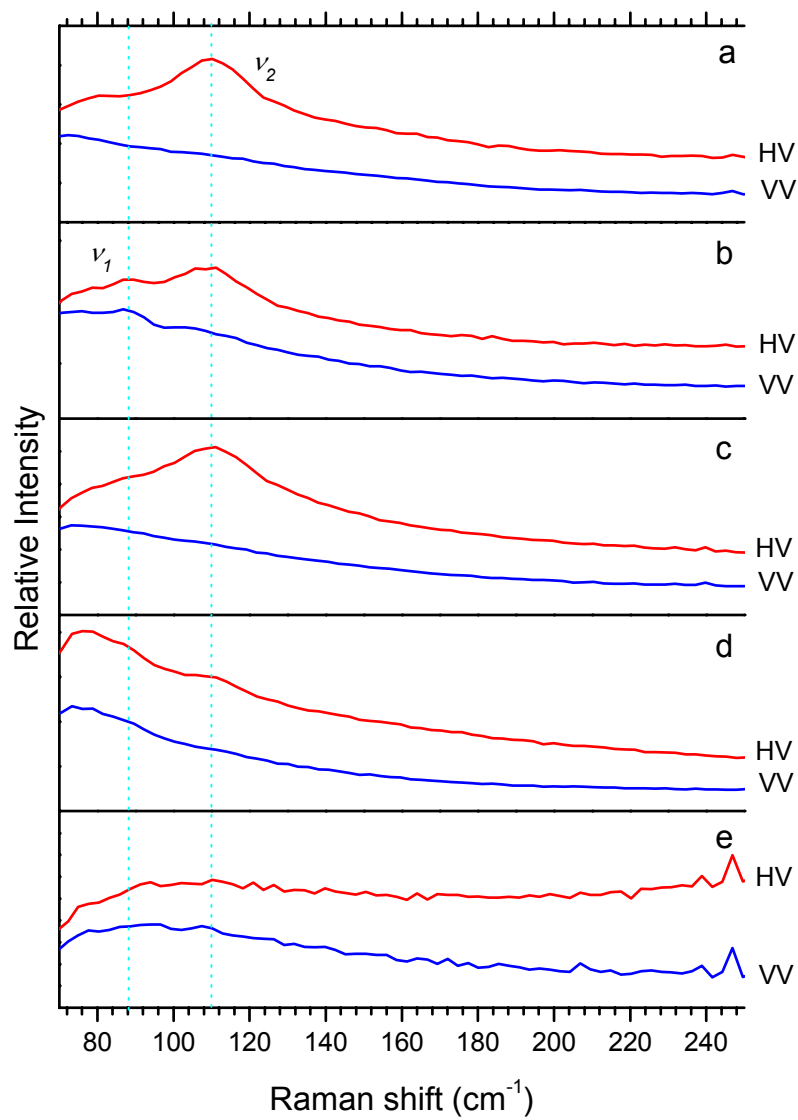

A.6.5. $(NdI_3)_{0.075}$-$(NdI_2)_{0.025}$-$(LiI\text{-}KI)_{eu, 0.90}$
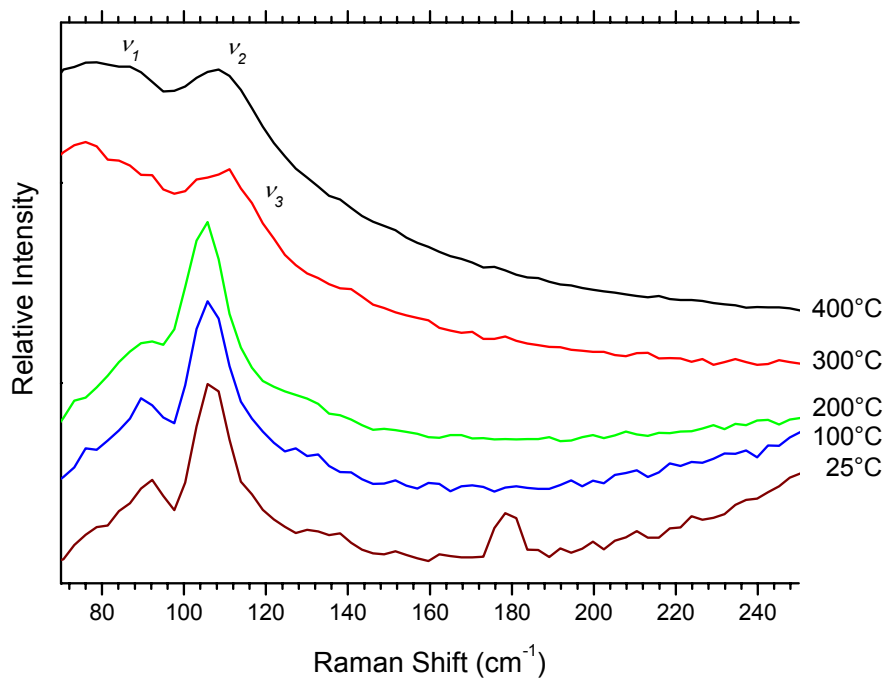
A.6.6. $(NdI_3)_{0.05}$-$(NdI_2)_{0.05}$-$(LiI\text{-}KI)_{eu,\ 0.90}$
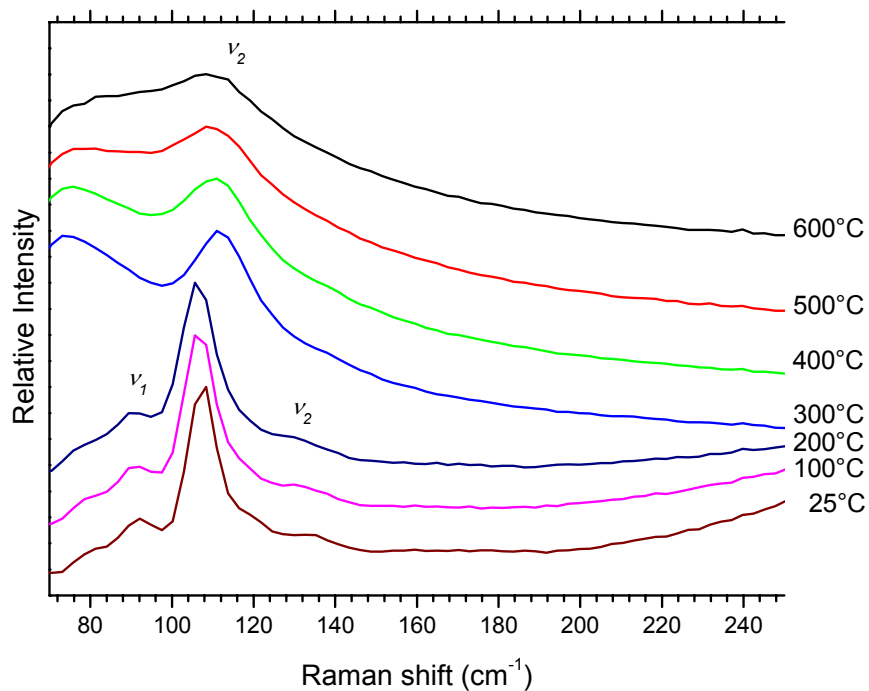
A.6.7. $(NdI_3)_{0.025}$-$(NdI_2)_{0.075}$-$(LiI\text{-}KI)_{eu,\ 0.90}$.
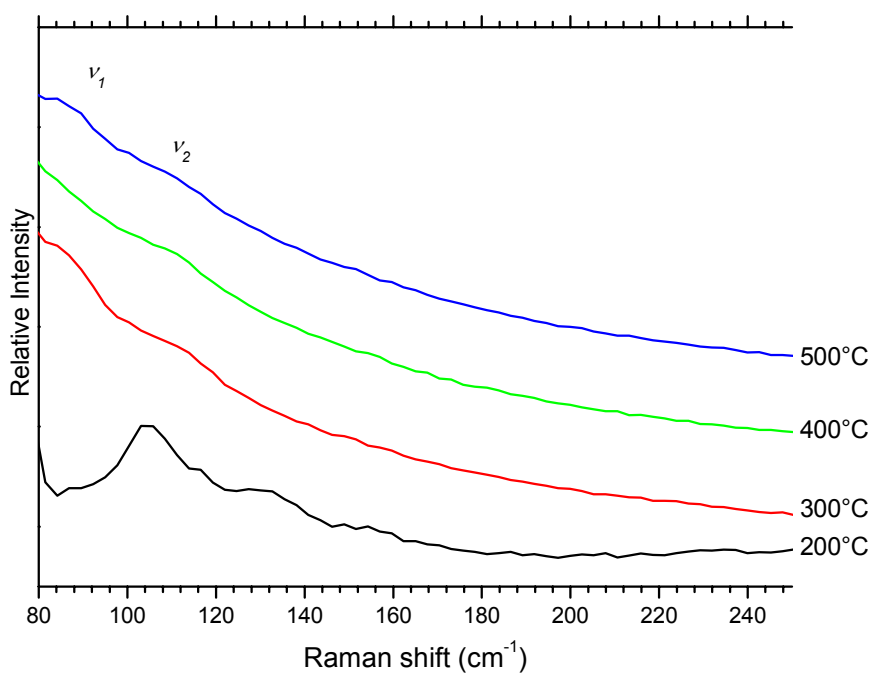
A.6.8. Liquid $(NdI_3)_x$-$(NdI_2)_y$-$(LiI-KI)_{eu, 1-x-y}$ at 500°C

a) $(NdI_3)_{0.05}$-$(LiI-KI)_{eu, 0.95}$.

b) $(NdI_3)_{0.075}$-$(CeI_2)_{0.025}$-$(LiI-KI)_{eu, 0.90}$.

c) $(NdI_3)_{0.05}$-$(NdI_2)_{0.05}$-$(LiI-KI)_{eu, 0.90}$.

d) $(NdI_3)_{0.025}$-$(NdI_2)_{0.075}$-$(LiI-KI)_{eu, 0.90}$.

e) $(NdI_2)_{0.02}$-$(LiI-KI)_{eu, 0.98}$.

Manufacturer List

(Alfa) Alfa Chemikalien, Karlsruhe

(Aldrich) Aldrich Chemikalien, Steinheim

(M. Braun) M. Braun GmbH, Garching

(Deutsche Carbon) Deutsche Carbon AG, Frankfurt am Main

(Eurotherm) Eurotherm GmbH, Limburg

(Hüttinger) Hüttinger, Freiburg

(Jobin Yvon) Jobin Yvon GmbH, Grasbrunn

References

Aride 1982   J. Aride, J.-P. Chaminade and M. Pouchard, *J. Crystal Growth*, **57** (1982) 194.

Atkins 1999   P. W. Atkins, Physical Chemistry, Sixth Edition, Oxford University Press (1999).

Bachtler 1994   M. Bachtler, J. Rockenberger and W. Freyland, *J. Phys. Chem.,* **98** (1994) 742.

Beck 1976   H. P. Beck, *Z. Naturforsch. B*, **31** (1976) 1548.

Beck 1992   H. P. Beck and M. Schuster, *J. solid State Chemistry*, **100** (1992), 301.

Bogacz 1999   A. Bogacz, L. Rycerz, S. Rumianowski, W. Szymanski, W. Szklarski, *High Temp. Material Processes,* **3** (1999) 461.

Boghosian 1996   S. Boghosian and G. N. Papatheodorou, *Handbook on the Physics and Chemistriy of Rare Earths*, Vol. 23, ed. By KA. Gscheider, Jr. and L. Eyring, Elsevier (1996).

Børresen 1996   B. Børresen, V. Dracopoulos, G. Photiadis, B. Gilbert and G. N. Papatheodorou, *Proc. X Inter. Symp. Molten Salts ECS*, **96**-7 (1996).

Böttger 1985   H. Böttger, V. V. Bryksin in Hopping Conduction in Solids, Akademie Verlag, Berlin (1985).

Bratsch 1982   S. Bratsch and H. B. Silber, *Rare Earths Mod. Sci. Thecnol.*, **3** (1982) 291.

Bredig 1964   M. A. Bredig, in *Molten Salt Chemistry,* ed. M. Blander, Interscience, New York (1964).

Bronstein 1962   H. R. Bronstein, A. S. Dworkin and M. A. Bredig, *J. Phys. Chem.*, **66** (1962) 44.

Brooker 1975   M. H. Brooker, *Applied Spectroscopy*, **29**-6 (1975) 528.

Brooker 1975a   M. H. Brooker, *J. chem.. Phys.*, **63** (1975) 3054.

Brooker 1988   M. H. Brooker, O. F. Nielsen and E. Praestgaard, *J. Raman Spectroscopy*, **19** (1988) 71.

Brooker 1995   M. H. Brooker, O. F. Nielsen and D. Christensen, *J. Raman Spectroscopy*, **26** (1995) 331.

Brown 1968   D. Brown, *Halides of the Transition Elements. Volume: Halides of the Lanthanides and Actinides*, New York: John Wiley and Sons, Inc, 1968.

Bulmer 1975   J. T. Bulmer, d. E. Irish, F. W. Grossman, G. Herriot, M. Tseng and A.J. Weerheim, *Applied spectroscopy* **29**-6(1975) 506.

Bulkin 1991   B. J. Bulkin, *Analytical Raman Spectroscopy. Chemical analysis volume 114*, B. J. Bulkin and J. G. Grasselli, editors, New York: John Wiley and Sons, Inc, 1991.

Child 1983   W. C. Child, Jr. and G. N. Papatheodorou, *J. Chem. Phys.*, **87** (1983) 272.

Choca 1974   M. Choca, J. R. Ferraro and N. Nakamoto, *Coordination Chemistry Reviews*, **12** (1974) 295.

Choca 1975   M. Choca, J. R. Ferraro and N. Nakamoto, *J. inorg. nucl. Chem.,* **37** (1975) 1425.

Corbett 1961   J. D. Corbett, L. F. Druding, W. J. Burkhard and C. B. Lindahl, *Discussions Faraday Soc.*, **32** (1961) 79.

Corbett 1983   J. D. Corbett, *Inorg. Synth.*, **22** (1983) 15.

Cordfunke 2001   E. H. P. Cordfunke and R. J. M: Konings, *Thermochim. Acta*, **375** (2001) 17.

CRC 1997   CRC *Handbook of Chemistry and Physics*, CRC Press, New York (1997).

Dai 1998   S. Dai, H. Xiao, J. P. Young, *Electrochemical Society Proceedings*, **98**-11 (1998) 592.

Damen 1986   T. C. Damen, A. Kiel, S. P. S. Porto and S. Singh, *Solid State Communications*, **6**(1968) 671.

Del Cul 1992   G. D. Del Cul, S. E. Nave, G. M. Begun and J. R. Peterson, *J. Raman Spectroscopy*, **23** (1992) 267.

Dracopoulos 1998   V. Dracopoulos, B. Gilbert and G. N. Papatheodorou, *J. Chem. Soc., Faraday Trans.*, **94**-17 (1998) 2601.

Druding 1959   L. F. Druding, J. D. Corbett, *J. Amer. Chem. Soc.,* **81** (1959) 5512.

Druding 1961   L. F. Druding, J. D. Corbett, *J. Amer. Chem. Soc.,* **83** (1961) 2462.

Dworkin 1963   A. S. Dworkin, R. A. Sallach, H. R. Bronstein, M. A. Bredig and J. D. Corbett, *J. Phys. Chem.*, **67** (1963) 1145.

Ferraro 1969   J. R. Ferraro and J. S. Ziomek, *Introductory Group Theory and its Application to Molecular Structure,* Premium Press, New York (1969).

Ferraro 1994   J. R. Ferraro, K. Nakamoto, *Introductory Raman Spectroscopy*, Academic Press, New York (1994)

Foosnæs 1981   T. Foosnæs and H. A. Øye, *Acta Chemica Scandinavica A*, **35**(1981) 81.

Freyland 1994   W. Freyland, Z. Phys. Chem., **184** (1994)139.

Freyland 1995   W. Freyland in *Metal-Insulator Transitions Revisited*, ed. By P. P. Edwards and C. N. R. Rao, Taylor and Francis, London (1995).

Gaune-Escard 1994   M. Gaune-Escard, A. Bogacz, L. Rycerz and W. Szczepaniak, Thermochim. Acta, **236** (1994) 67.

Gmelin 1982   *Gmelin Handbuch der Anorganischen Chemie, Seltenerdelemente,* System Nr. 39, Vols.: **C4a** (Chloride), **C4b** (Individual Chloride), **C5** (Alkali Chlorometallates), **C6** (Iodide), **E1** (Optical Spectra of Ce) and **E2a** (Optical Spectra of Nd), 1982.

Harfold 1946   R. S. Harfold, *J. Chem. Phys.,* **14** (1946) 8.

Harfold 1946a   R. S. Harfold and O. A. Shaeffer, *J. Chem. Phys.,* **14** (1946) 141.

Hase 1981   Y. Hase, P. O. Dunstan L. and M. L. A. Temperini, *Spectrochimica Acta*, **37A**-8 (1981) 597.

Herzberg 1954   G. Herzberg, Molecular Spectra and Molecular Structure, II. Infrared and Raman Spectra of Polyatomic Molecules, ed. D. Van Nostrand Company, Inc., New York (1954).

Ichikawa 1979   K. Ichikawa, W. W. Warren Jr., *Physical Review B*, **20**-3 (1979) 900.

Ichikawa 1982   K. Ichikawa, *Supplement of the Progress of Theoretical Physics*, **72** (1982) 156.

Iizuka 1997   M. Iizuka, T. Koyoma, N. Kondo, R. Fujita and H. Tanaka, *J. Nucl. Mater*., **247** (1997) 183.

Janz 1967   G. J. Janz, *Molten Salt Handbook*, Academic Press, New York, (1967).

Janz 1977   G. J. Janz, R. P. T. Tomkins, C. B. Allen, J. R. Downey, Jr. and S. K. Singer, *J. Phys. Chem. Ref. Data*, **6** (1977) 409.

Johnson 1969   D. A. Johnson, *J. Chem. Soc. A.*, (1969) 2578.

Jörger 1998   M. Jörger, *Diploma Thesis*, University of Karlsruhe (1998).

Kim 1996   Y. C. Kim and J. Oishi, *J. Less-Common Met.*, **100** (1996) 95.

Koyama 1997   Y. Koyama. R. Takagi, Y. Iwadate, K. Fukushima, *J. Alloys and Compounds*, **260** (1997) 75.

Kutscher 1974   J. Kutscher and A. Schneider, *Z. Anorg. Allg. Chem.*, **408** (1974) 121.

Kvam 1998   K. R. Kvam, D. Bratland and H. A. Øye, in *Proceedings of the international Terje Østvold Symposium,* (1998) 97.

Laptev 1986   D. M. Laptev, T. V. Kiseleva, M. N. Kulagin, V. F. Goryushkin and E. S. Vorontsov, *Russ. J. Inorg. Chem.*, **31**-8 (1986) 1131.

Long 1977   D. A. Long, *Raman Spectroscopy*, McGraw Hill International Book Company, London (1977).

Loos 1974   K. R. Loos, A. C. Jones, *J. Phys. Chem.*, **78**-22 (1974) 2306.

Madden 1991   P. A. Madden, K. F. O'Sullivan, *J. Chem. Phys.*, **95**-3 (1991) 1980.

Madden 2000   P. A. Madden, M. Wilson, *J. Phys. Condens. Matter*, **12** (2000) A 95.

Marcus 1977   Y. Marcus, *Introduction to Liquid State Chemistry*, John Wiley, London (1977).

Maroni 1971   V. A. Maroni, *J. Chem. Phys.*, **54** (1971) 4126.

Mediaas 1997   H. Mediaas, G. Photiadis, G. N. Papatheodorou, J. E. Vindstad and T. Østvold, *Acta Chemica Scandinavica*, **51** (1997) 8.

Mediaas 2000   H. Mediaas, O. Tkatcheva, V. Dracopoulos, G. N. Papatheodorou, G. J. Kopouros and T. Østvold, *Metallurgical and Materials Transactios B*, **31B** (2000) 631.

Mellors 1959   G. W. Mellors and S. Senderoff, *J. Phys. Chem.,* **63** (1959) 1110.

Mendes-Filho 1979   J. Mendes-Filho, F. E. Melo and J. E. Moreira, *J. Raman Spectroscopy*, **8**-4 (1979) 199.

Meyer 1985   G. Meyer and T. Shield, *Z. anorg. Allg. Chem.*, **528** (1985) 55.

Meyer 1988   G. Meyer, *Chem. Rev.*, **88** (1988), 93.

Mochinaga 1993   J. Mochinaga, M. Ikeda, K. Igarashi, K. Fukushima and Y. Iwadate, *J. of Alloys and Compounds*, **193** (1993) 36.

Muenter 1996   J. S. Muenter, *J. Chemical Education*, **73**-6 (1996) 576.

Nakamura 1997   K. Nakamura and M. Kurata, *J. Nucl. Mat.*, **247** (1997) 309.

Nattland 1993   D. Nattland, Th. Rauch and W. Freyland, *J. Chem. Phys.,* **98** (1993) 4429.

Nattland 1996   D. Nattland, *Habilitationsschrift*, University of Karlsruhe (1996).

Papatheodorou 1975   G. N. Papatheodorou, *Inorg. Nucl. Chem. Letters*, **11** (1975) 483.

Papatheodorou 1996   G. N. Papatheodorou, S. G. Kalogriantis, T. G. Mihopoulos and E. A. Pavlatou, *J. Chem. Phys.* **105**-7 (1996) 2660.

Papatheodorou 2000   G. N. Papatheodorou, in *Progress in molten salt Chemistry 1*, ed.by R. W. Berg and H. A. Hjuler, Elvesier, Paris, (2000) 65.

Pavlatou 1997   E. A. Pavlatou, P. A. Madden and M. Wilson, *J. Chem. Phys.*, **107**-24 (1997) 10446.

Photiadis 1993   G. M. Photiadis, G. A Voyiatzis, und G. N. Papatheodorou, *MoltenSalts Forum*, **1-2** (1993/94) 183.

Photiadis 1998   G. M. Photiadis, B. Børresen, und G. N. Papatheodorou, *J. Chem. Soc., Faraday Trans.,* **94** (1998) 2605.

Quist 1971   A. S. Quist, *Applied Spectroscopy*, **25**-1 (1971) 80.

Satyavathi 1979   N. Satyavathi and N. Rajeswar Rao, *Pramãna*, **12**-2 (1979) 139.

Schaack 1970   G. Schaack and J. A. Koningstein, *J. Phys. Chem. Solids*, **31** (1970) 2417.

Shannon 1976   R. D. Shannon, *Acta Crystall. A*, **32**-5 (1976) 751.

Schindelbeck 1996   T. Schindelbeck and W. Freyland, *J. Phys. Chem.,* **105** (1996) 4448

Smirnov 1965   M. V. Smirnov and V. S. Lbov, *Soviet Electrochemistry*, **1** (1965) 740.

Smirnov 1966   M. V. Smirnov, P. M. Usov, V. S. Lbov and O. M. Shabanov, *Tr. Inst. Elektrokhim.*, 1965, 57; translated in A. N. Barabroshkin, *Electrochemistry of Molten and Solid Electrolytes*, Consultans Bureau, New York, **3** (1966) 49.

Smirnov 1982   M. V. Smirnov and Stepanov, *Electrochim. Acta*, **27** (1982) 1551.

Stöhr 1999   U. Stöhr, W. Freyland, *PCCP* **1** (1999) 4383.

Stöhr 1999a   U. Stöhr, W. Freyland, *Electrochim. Acta*, **44** (1999) 2199.

Stöwe 1997   K. Stöwe, S. Tratzky, H. P. Beck, A. Jungmann, R. Claessen, R. Zimmermann, G. Meng, P. Steiner, S. Hüfner, *J. Alloys and Compounds*, **246** (1997) 101.

Sushchinskii 1972   M. M. Sushchinskii, *Raman Spectra of Molecules and Crystals*, Israel Program for Scientific Translations, New York-Jerusalem-London, 1972.

Terakado 2002   O. Terakado, PhD thesis, University of Karlsruhe, (2002).

Terakado 2002a   O. Terakado, S. Zein El Abedin, F. Endres, D. Nattland, W. Freyland, *J. Non-Crystalline Solids*, **312-314** (2002) 459.

Walton 1998   P. H. Walton, *Beginning Group Theory for Chemistry*, Workbooks in Chemistry, ed. by S. K. Scott, Oxford University Press, 1998.

Wang 2001   S. Wang, W. Wang, J. Zou, and Y. Qian, *Materials Chemistry and Physics*, **68** (2001) 246.

Warren 1984   W. W. Warren Jr., S. Sotier and G. Brennert, *Physical Review B*, **30**-1 (1984) 6.

Warren 1985   W. W. Warren Jr., in *The Metallic and Non-metallic State of the Matters*, ed. by P. P. Edwars and C. N. R. Rao, Taylor and Francis, London, 1985.

Wasse 1999   J. C. Wasse and P. S. Salmon, *J. Phys. Condens. Matter*, **11** (1999) 1381 and 9293.

Weber 1993   W. H. Weber, K. C. Hass and J. R. McBride, *Physical Review B,* **48** (1993) 178.

Wilmarth 1988   W. R. Wilmarth, G. M. Begun, J. F. Daniel, R. C. Hard, S. E. Nave and J. R. Peterson, *J. Raman Spectroscopy*, **19** (1988) 245.

Xie 1993   G. Xie, K. Ema, Y. Ito and Z. M. Shou, J. Appl. Electrochem., **23** (1993) 753.

Yamamura 1998   Y. Yamamura, I. Wu, H. Zhu, M. Endo, N. Akao, M. Mohamedi and Y. Sato, *Molten Salt Chem.. Technol.*, **5** (1998) 355.

Young 1964   J. P. Young, *Analytical Chemistry*, **36**-2 (1964) 391.

Zein El Abedin 2002 S. Zein El Abedin, O. Terakado, F. Endres, D. Nattland and W. Freyland, *Phys. Chem. Chem. Phys.*, **4** (2002) 5335.

Curriculum Vitae

Personal Information

Name	Verónica María RODRÍGUEZ BETANCOURTT
Date of birth	27.06.1972
Birthplace	Guadalajara, Jalisco, México
Family status	married
Children	one daughter, 5 years old

Basic Studies

1978 - 1984	Primary School in Guadalajara, Mexico
1984 - 1987	Middle School in Guadalajara
1987 - 1990	High School in Guadalajara

Studies

Sep. 1990 – Aug. 1995	Chemical Engineering at the University of Guadalajara, Mexico Area: Cellulose and Paper Title of the thesis: Determination of the Compressibility Factor of the Marrow of Canebagasse and its Influence on the Mechanical and Physical Properties of the Paper (in Spanish).
Sep. 1995 – Jan. 1998	Master in Sciences at the University of Guadalajara Area: Electrochemistry Title of the thesis: Mathematical Modelling of Microelectrodes applied to SECM and SPECM (in Spanish).
Apr. 1999 – Jul. 2003	Ph.D. at the University of Karlsruhe Institute of Physical Chemistry, Physical Chemistry of Condensed Matter Division

Acknowledgements